Imaginary-time quantum many-body theory out of equilibrium. II. Analytic continuation of dynamic observables and transport properties

Andreas Dirks,[1] Jong E. Han,[2] Mark Jarrell,[3] and Thomas Pruschke[1]
[1]*Institut für Theoretische Physik, Universität Göttingen, D-37077 Göttingen, Germany*
[2]*Department of Physics, State University of New York at Buffalo, Buffalo, New York 14260, USA*
[3]*Department of Physics and Astronomy, Louisiana State University, Baton Rouge, Louisiana 70803, USA*
(Received 3 May 2012; published 28 June 2013)

Within the imaginary-time theory for nonequilibrium in quantum dot systems the calculation of dynamical quantities like Green's functions is possible via a suitable quantum Monte Carlo algorithm. The challenging task is to analytically continue the imaginary-time data for both complex voltage and complex frequency onto the real variables. To this end a function-theoretical description of dynamical observables is introduced and discussed within the framework of the mathematical theory of several complex variables. We construct a feasible maximum-entropy algorithm for the analytical continuation by imposing a continuity assumption on the analytic structure and provide results for spectral functions in stationary nonequilibrium and current-voltage characteristics for different values of the dot charging energy.

DOI: 10.1103/PhysRevB.87.235140 PACS number(s): 02.70.Ss, 72.10.Bg, 73.63.Kv

I. INTRODUCTION

Dynamic observables play a crucial role in the Matsubara voltage approach introduced by Han and Heary to address steady-state nonequilibrium properties of models for quantum dots.[1] In a previous publication (hereafter referred to as paper I)[2] we showed the conditions under which the real-time Keldysh and imaginary-time Matsubara-voltage approaches are formally equivalent and how a proper analytical continuation must be performed. In paper I, this scheme was applied to static quantities obtained from a continuous-time quantum Monte Carlo (CT-QMC) algorithm[3,4] combined with a standard maximum-entropy (MaxEnt) approach[5] to obtain results for steady-state expectation values of quantum dot models at finite bias.

We consider a single-impurity Anderson model for the quantum dot system,[2] with the Hamiltonian

$$\begin{aligned}\hat{H} = &\sum_{\alpha k\sigma} \epsilon_{\alpha k\sigma} c^\dagger_{\alpha k\sigma} c_{\alpha k\sigma} + \epsilon_d \sum_\sigma d^\dagger_\sigma d_\sigma \\ &- \sum_{\alpha k\sigma} \frac{t_\alpha}{\sqrt{\Omega}} (d^\dagger_\sigma c_{\alpha k\sigma} + \text{H.c.}) \\ &+ U(n_{d,\uparrow} - 1/2)(n_{d,\downarrow} - 1/2). \end{aligned} \tag{1}$$

This Hamiltonian describes a quantum dot device which consists of the quantum dot orbital operator $d^\dagger_\sigma$ of spin σ and with source and drain leads, represented by conduction electron operators $c^\dagger_{\alpha k\sigma}$ with the continuum index k, the spin index σ and the reservoir index $\alpha = L, R$ for the source (left) and drain (right), respectively. The model is characterized by few parameters[6]: the local energy or gate voltage ϵ_d, which controls the number of electrons on the dot; the charging energy $U > 0$ due to the small capacitance; and finally the coupling of the dot to the leads, which can in many cases be collected in two quantities, Γ_L and Γ_R.

Although some thermodynamic observables can be calculated directly without analytic continuation of imaginary frequency,[2] only a restricted set of observables can be handled in this manner. Unfortunately, the current operator $\langle I \rangle$ is not suitable, and the rather important question about the transport through a quantum dot, both electrically and thermally driven, must be addressed in a different manner. For simple quantum dot geometries one can employ the result by Meir and Wingreen,[7] who showed that for single quantum dots and not-too-different properties in the left and right leads, one can express the current through the dot due to a finite external bias $eV_B \equiv \Phi$ via the density-of-states (DOS) $\mathcal{N}_\sigma(\epsilon; \Phi)$ on the dot as

$$I(\Phi) = I_0 \sum_\sigma \int d\epsilon [f_L(\epsilon) - f_R(\epsilon)] \mathcal{N}_\sigma(\epsilon; \Phi), \tag{2}$$

where $f_\alpha(\epsilon)$ denotes Fermi's function for the left or right lead. Note that the bias enters in two distinct ways: first, in the Fermi functions through the chemical potential of the leads as[8] $\mu \pm \Phi/2$, and, second, through the DOS. Usually, for $\Phi \to 0$, one ignores the latter dependency and can thereby recover the results from linear-response theory. Note that Meir-Wingreen formula is only applicable in case the hybridization to left and right leads are proportional to each other, i.e., $\Gamma_L(\omega) \propto \Gamma_R(\omega)$.

Besides its relevance for calculating the current, the DOS is an interesting quantity in its own right, and its dependency as functions of frequency and bias is still a matter of debate. In equilibrium, it is well-known that the DOS develops a very sharp resonance, the so-called Kondo resonance, pinned at $\epsilon = 0$, which in linear response leads to the pinning of the conductance to the unitary limit. The precise way that this resonance dies under the influence of finite bias is actually unknown, and different techniques provide different answers.

Within the Matsubara-voltage imaginary-time approach by Han and Heary the nonequilibrium steady state is mapped to an infinite set of effective equilibrium systems by introducing a bosonic Matsubara voltage $\varphi_m = 4\pi m/\beta$.[1,2,4,9] It has to be analytically continued to a variable $z_\varphi \in \mathbb{C}$ in order to compute the limit $z_\varphi \to \Phi \pm i\delta$ to obtain the physical quantity at the chosen bias Φ.

Considering dynamic observables, the simultaneous presence of the fermionic Matsubara frequency $i\omega_n$, which must be analytically continued to $z_\omega \in \mathbb{C}$ to eventually obtain

the corresponding real-frequency quantity, implies that a double-complex-variable function $G(\underline{z})$, with $\underline{z} := (z_\varphi, z_\omega)^T \in \mathbb{C}^2$, must be studied. Without the presence of $i\varphi_m$, i.e., within conventional Matsubara theory, Green's functions are analytic on the upper and lower half planes, $\mathbb{H}$ and $\mathbb{H}^*$. Due to the rapid decay of $G(z_\omega)$ as $z_\omega \to \infty$, a Lehmann spectral representation with respect to the real axis is used.[10] Conversely, from a knowledge of all Matsubara-frequency data one can, in principle, infer the spectral function. Numerically, this is known to be an ill-conditioned problem. An approach, particularly suited for QMC data, is the MaxEnt technique.[5]

From a mathematical point of view, the branch cut on the real axis represents the only set of points $z_0 \in \mathbb{C}$ for which the Green's function is not holomorphic. The very location of the branch cut gives rise to the spectral representation in Matsubara theory; i.e., it yields, due the nonsingular structure at ∞, a unique characterization of the analytic structure. In order to perform an analytic continuation for the two-variable function $G(\underline{z})$ the natural question arises as to which minimal set of quantities characterizes its analytic structure in a unique fashion. Therefore, referral to mathematical results in the analysis of several complex variables is necessary (see in particular the discussion following Sec. III C 1).[4]

In the original implementation of Han and his co-worker,[1,9] analytic continuation on (z_φ, z_ω) produced rather smooth spectra in good agreement with other numerical results.[9,11] However, the employed methods were crude fit with *ad hoc* smoothening and annealing to the numerical data without regard to statistical analysis. In this work we provide mathematical foundation to multivariable analytic continuation and develop systematic numerical implementation.

The paper is structured as follows. Since the mathematical structure dealing with functions of several complex variables is probably very alien to the reader, we start with a presentation of the central results for spectral functions and transport properties of the single-impurity Anderson model in steady-state nonequilibrium in Sec. II. As compared to an earlier publication,[4] we improve our numerics by including several analytic wedges of the Green's function into the procedure. We refer to this as a *multiwedge approach*, as opposed to the earlier *single-wedge approach*. The underlying mathematical framework is developed in the succeeding sections. Starting from conventional one-dimensional complex analysis, Sec. III provides an introduction to the basic concepts of theory of several complex variables. We then use this theory to systematically analyze the analytical structure of the Matsubara-voltage Green's function and provide an axiomatic description of it. In Sec. IV, an asymptotically exact continuity assumption is employed to construct an integral representation for Matsubara Green's function $G(i\varphi_m, i\omega_n)$. It allows us to include more information within the Bayesian inference process of the MaxEnt method as compared to our previous approach in Ref. 4. The resulting structure connects to the earlier suggestions by Han and Heary.[1,9] For future applications, an unbiased extension of the integral representation beyond the continuity assumption is proposed in Sec. V.

Figure 1 provides an overview of the paper as a flowchart. It may serve as a guide. Mathematically less inclined readers may skip the lightly shaded Sec. III and study the numerical results in Sec. II, which are based on the continuity ansatz and MaxEnt procedure described in Sec. IV and corresponding appendixes. In the chart solid arrows denote numerical steps in the computation. Open arrows denote formal analytical steps required to derive the relations involved in the MaxEnt procedure for analytic continuation.

All numerical results provided in the paper rely on a highly precise continuous-time quantum Monte Carlo (QMC) implementation which was introduced in Ref. 4. The data provided by QMC simulations, see left box in Fig. 1, give rise to a discrete grid of well-estimated imaginary-time Green's function values. Due to the structure of the Matsubara-voltage formalism, however, these data, in general, belong to different analytic sheets of the two-variable Green's function [Fig. 13(b)], due to the presence of an infinite set of branch cuts. The analytic sheets are defined on so-called wedges in the complex variable space $\mathbb{C}^2$. Depending on the considered wedge, an analytic continuation within the sheet to real frequencies and voltages may not have a direct physical interpretation. However, QMC data from these sheets should be used to reconstruct the physical real-time limit. For this sake, the mathematical structure of the Green's function's sheets is systematically investigated in Sec. III. Since it may require a lot of effort to study the details of the latter, the reader is recommended to first study the results section and possibly skip Sec. III at first reading.

The results section (Sec. II) discusses numerical results for the dot electron spectral function out of equilibrium and consequent transport characteristics. It relies on a MaxEnt procedure which infers a probability distribution based on a linear relation (72) which is derived in Sec. IV but has to be inverted. Since as in the conventional Wick rotation of imaginary-time data,[5] the inversion is an ill-posed problem, the MaxEnt provides a most probable solution by means of Bayes' theorem. Central to the function-theoretical derivation of the relation (72) is a continuity assumption to the real-time structure of the theory, Eq. (65). It gives rise to the kernel operator (73) which defines the inverse problem (72). It is shown in Sec. IV that the continuity assumption improves the MaxEnt algorithm for the determination of spectral functions dramatically, as compared to the earlier approach introduced in Ref. 4, such that nontrivial nonequilibrium spectra could be obtained.

Let us now briefly discuss the more mathematically involved Sec. III by means of the flowchart in Fig. 1. Since the analytical derivation makes use of two-dimensional complex analysis, it provides an introduction to that field, comparing its fundamental notions to those of conventional function theory. In particular, the theory of integral representations of functions on domains of holomorphy is discussed. Such functions may often be parametrized by their values on the so-called Bergman-Shilov boundary. In an analogous way, conventional complex analysis parametrizes functions on domains by their boundary values using, e.g., Cauchy's integral equation. Also the concept of the conformal map has the analogon of a biholomorphic map, which is widely used for formal derivations in the present work. Section III also systematically points out that wedges are the domains of holomorphy for the two-variable Green's function and provides constraints to the Green's function which give rise to Vladimirov's integral representation (43), which is central

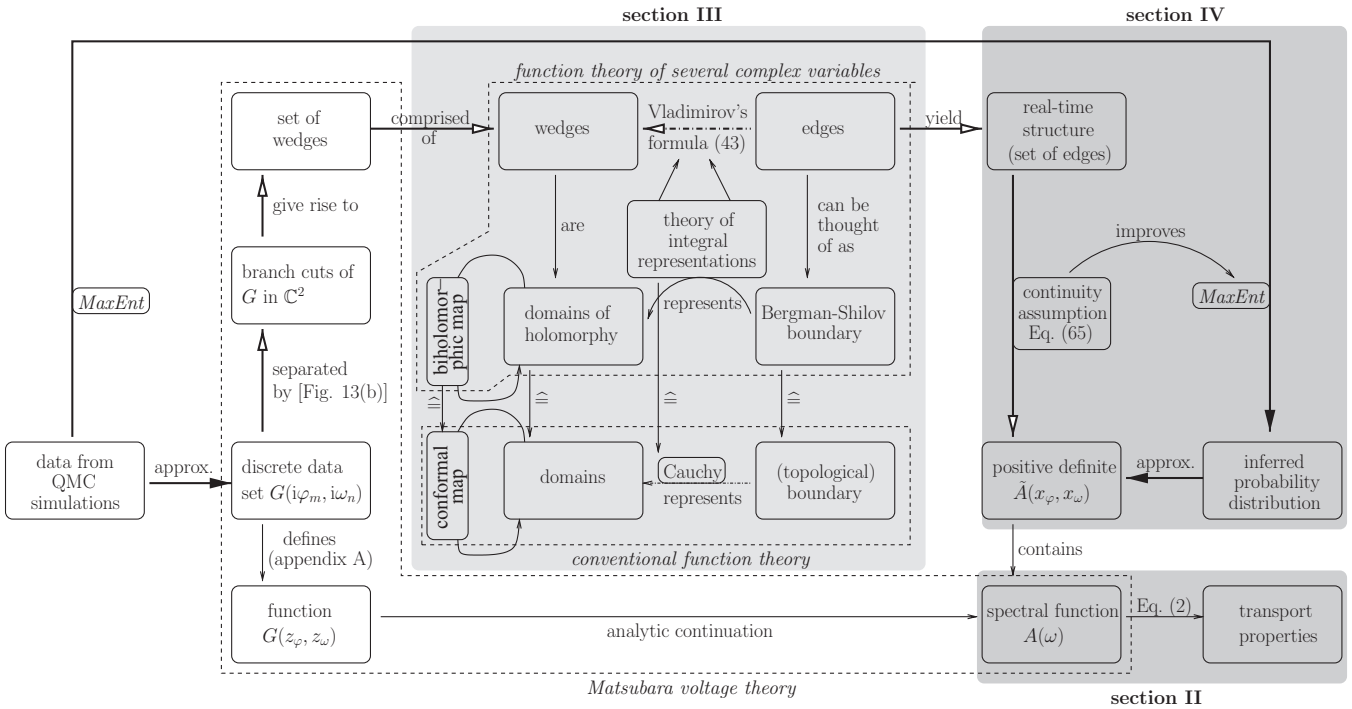

FIG. 1. Contents of the paper as a flowchart. Solid arrows represent numerical procedures within our approach. Open arrows represent the formal steps necessary for a derivation of the MaxEnt kernel used for numerical results. Shaded areas are discussed in the corresponding sections. The rather unconventional two-dimensional function theory with respect to the simultaneously variables (z_φ, z_ω) is explained by analogies ($\widehat{=}$) with the conventional theory in the light-shaded area. It may be skipped at first reading. Concepts such as the biholomorphic maps are used to obtain explicit equations. Dash-dotted lines denoting either Vladimirov's formula or Cauchy's integral equation put an emphasis on the fact that the content of a domain (of holomorphy) is parametrized by its (Bergman-Shilov) boundary. In the numerical implementation it is thus an inverse problem to reconstruct function values on the (Bergman-Shilov) boundary, which requires a MaxEnt approach.

to the constructed MaxEnt algorithm. The representation links function values on the real-time boundary (the edge) of a considered wedge to data within the wedge. The dash-dotted lines in Fig. 1 represent such linear relations, which are practically used in the reverse direction and thus bring along an inverse problem.

II. RESULTS FOR SPECTRAL FUNCTIONS AND TRANSPORT

In the following, we present results obtained from analyzing data using the CT-QMC algorithm described in Ref. 4 based on the "multiwedge" MaxEnt scheme we present in this paper. We present data for the particle-hole symmetric case, $\epsilon_d = 0$. Figure 2 provides an example for the raw simulation output. It has to be analytically continued with respect to both Matsubara voltage and frequency. This was accomplished using MaxEnt applied to the functional relation between Matsubara-domain data and spectral function developed in Sec. IV. As discussed in Ref. 4, the Green's function is analytical in certain cones in the four-dimensional variable space. Previously, we used only the cone closest to $i\varphi_m = 0$ for providing information to the MaxEnt. This turned out to be not sufficient to generate reliable and reproducible spectra. As discussed in detail in Sec. IV and Appendix E, we here assume a certain property of the Green's function, namely that its real part at the meeting point of the cones is independent of the cone it was approached from. This makes it possible to map data in different cones by means of linear transformations into the actual data space and hence improve the accuracy of the MaxEnt tremendously. We introduced this earlier in the introduction as multiwedge approach. A

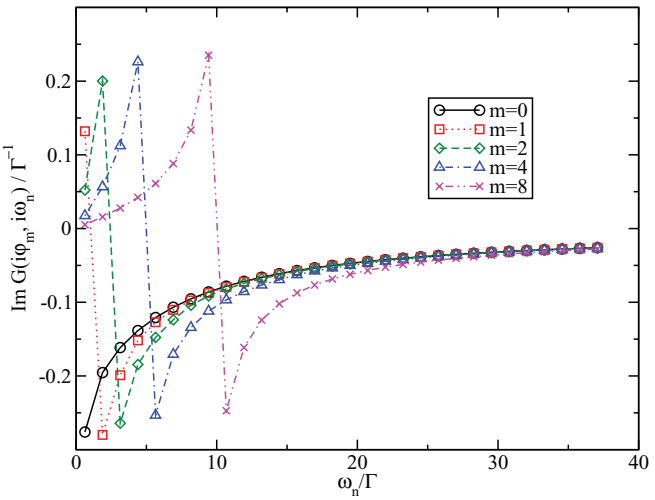

FIG. 2. (Color online) Effective-equilibrium data as obtained from CT-QMC simulations[4] for $U = 8\Gamma, e\Phi = 0.1\Gamma, \beta = 5\Gamma^{-1}$. The integer number m specifies the respective index of the Matsubara voltage $\varphi_m = 4\pi m/\beta$. The discontinuity at $\omega_n = \varphi_m/2$ is the principal branch cut which will, in particular, be discussed in Sec. III D.

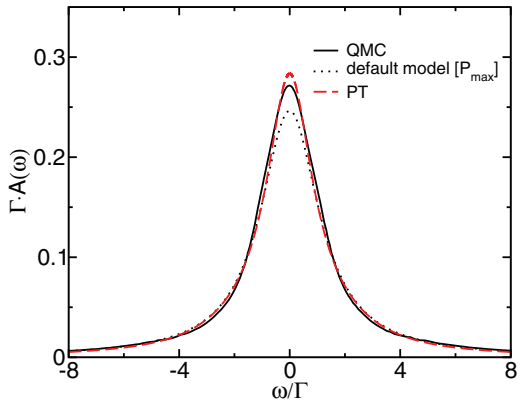

FIG. 3. (Color online) Spectral function of the dot electrons as inferred for the nonequilibrium weak-coupling case $U = 2\Gamma$, $e\Phi = \Gamma$, $\beta = 5\Gamma^{-1}$, compared to second-order perturbation theory.

comparison of the single-wedge and multiwedge approaches is provided at the end of this section. We must emphasize that the validity of this crucial property underlying the multiwedge approach cannot be proven rigorously; however, the results obtained can be taken as evidence that its violation does not influence the physical structures too much. Furthermore, in Sec. V we provide a route to improve on this approximation systematically, at the expense of a more complex algorithm.

We concentrate on the evolution of the spectral functions as a function of Coulomb parameter U and bias voltage Φ. Using the relation (2) we also calculate $I(V)$ characteristics and compare them to results obtained with other techniques.

A. Weak-coupling regime

The resulting nonequilibrium spectral function for $U = 2\Gamma$, $\beta = 5\Gamma^{-1}$, $e\Phi = \Gamma$, obtained by evaluating $A(\omega) = \tilde{A}(\Phi,\omega)$, where $\tilde{A}$ is some two-dimensional MaxEnt-inferred quantity, is displayed in Fig. 3. A good agreement with the second-order perturbation theory provided by Ref. 12 is observed.

However, the maximal value of the resonance is slightly smaller than predicted by perturbation theory. This could well be due the fact that MaxEnt tends to infer a conservative estimate close to the default model. The latter is also included in Fig. 3 as a dotted line; it is a Lorentzian whose width is determined by the Bayesian procedure outlined in Appendix E. For the weak-coupling case, the width is essentially the one of the true spectrum, as expected.

B. Intermediate-coupling regime

Figure 4 shows spectral functions computed at $U = 4\Gamma$ and inverse temperature $\beta = 5\Gamma^{-1}$ for different bias voltages Φ. An excellent agreement with second-order perturbation theory is obtained for the cases $e\Phi = 0.125\Gamma$ and $e\Phi = \Gamma$,

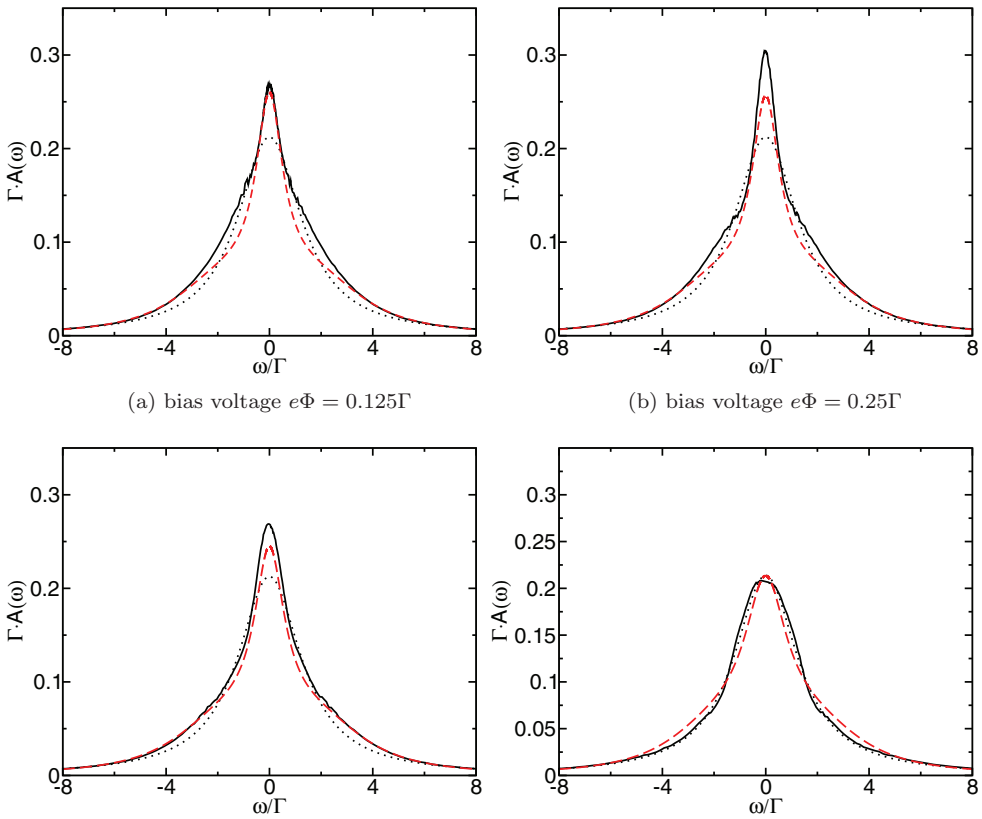

(a) bias voltage $e\Phi = 0.125\Gamma$ (b) bias voltage $e\Phi = 0.25\Gamma$

(c) bias voltage $e\Phi = 0.5\Gamma$ (d) bias voltage $e\Phi = 1.0\Gamma$

FIG. 4. (Color online) Nonequilibrium spectral functions for $U = 4\Gamma$ and inverse temperature $\beta = 5\Gamma^{-1}$ of the leads, as compared to second-order perturbation theory. Line legends are the same as in Fig. 3.

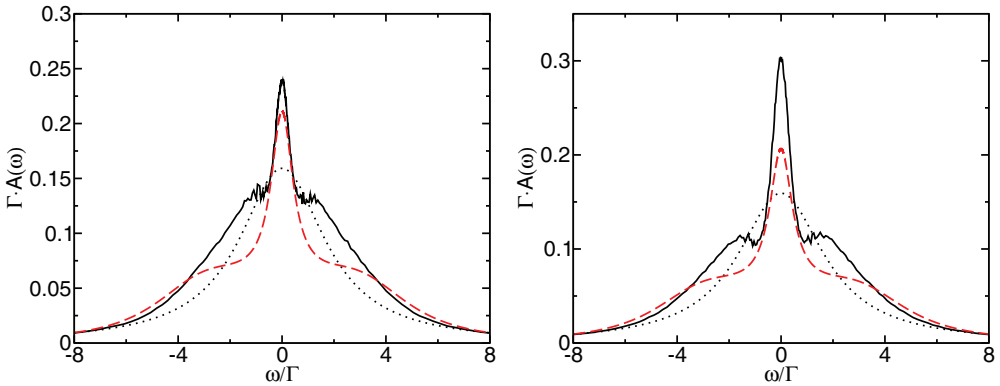

(a) bias voltage $e\Phi = 0.125\Gamma$ (b) bias voltage $e\Phi = 0.25\Gamma$

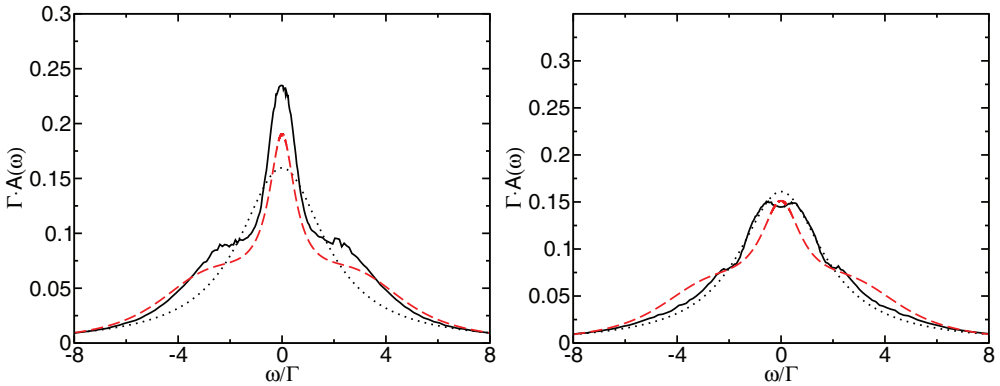

(c) bias voltage $e\Phi = 0.5\Gamma$ (d) bias voltage $e\Phi = 1.0\Gamma$

FIG. 5. (Color online) Nonequilibrium spectral functions for $U = 6\Gamma$ and inverse temperature $\beta = 5\Gamma^{-1}$, as compared to second-order perturbation theory. Line legends are the same as in Fig. 3.

and it is reasonable for $e\Phi = 0.5\Gamma$. Although one should not expect it to be very different, the quasiparticle resonance in the MaxEnt result for $e\Phi = 0.25\Gamma$ is overshooting $e\Phi = 0.125\Gamma$ and disagrees with the almost unchanged second-order perturbation theory. This is presumably a systematic MaxEnt artifact, possibly related to the default model.

The normalization of the MaxEnt spectra is reasonably close to one. In particular, at the small voltages, and for larger frequencies some side bands form which tend to increase the total spectral weight unphysically. However, the good description of the low-energy physics seems to be unaffected by this type of artifact. Note that again the optimal width of the default model is the same as the one for the final spectrum.

Inferred spectral functions for an even stronger interaction $U = 6\Gamma$ are displayed in Fig. 5 for intermediate to large bias voltage. For the equilibrium situation we already are in a regime with a distinct three-peak structure with an Abrikosov-Suhl resonance (ASR) at $\omega = 0$ characteristic for the Kondo regime. An estimate for the equilibrium Kondo scale gives $T_K \approx 0.1\Gamma$. Again, the general low-energy behavior agrees reasonably well with the results from perturbation theory—which should still be valid for this value of U—and the weight at $e\Phi = 0.25\Gamma$ is again overestimated. At $e\Phi = 0.5\Gamma$ one now observes a distinctly larger broadening of the ASR as compared to perturbation theory, and at $\Phi = \Gamma$ a clear double-peak structure is visible. This structure is compatible with a Kondo peak splitting. However, due to the approximations involved, we feel unable to decide at present whether this feature is actually a prediction of the Matsubara-voltage theory itself. It is interesting to note that here the default model is strongly renormalized for small bias, while at large bias the default model, apart from the double peak structure around $\omega = 0$, again is already a reasonable estimate for the full spectrum.

As before, the spectral weight in the now developing Hubbard bands is strongly enhanced as compared to perturbation theory, pointing towards an overestimation of the integral weight by MaxEnt. On the other hand, the position is in good agreement with perturbation theory.

Figure 6 shows a similar set of curves for interaction strength $U = 8\Gamma$. As compared to the lower values of U, a similar behavior of the algorithm is observed. The perturbative prediction for the ASR is again essentially reproduced in the cases $e\Phi = 0.1\Gamma$ and $e\Phi = \Gamma$. The ASR is, however, again broadened as a function of the bias voltage and appears to split eventually at $e\Phi = \Gamma$. Again, intermediate voltages have a much stronger weight of the quasiparticle peak, and the difference between $e\Phi = 0.1$ and $e\Phi = 0.2$ is even larger than for lower values of the interaction. If those artifacts are due to the MaxEnt, they might be at least partially removed by using more appropriate default models or an annealing procedure, i.e., using spectra for smaller bias as defaults for larger. Such a procedure can be successfully applied when lowering temperatures (see the next section). The increased interaction again broadens the spectra as compared to smaller values of U.

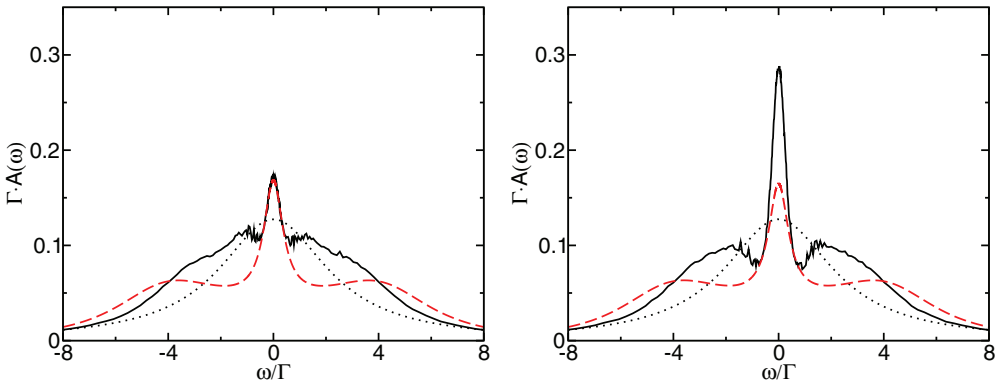

(a) bias voltage $e\Phi = 0.1\Gamma$ (b) bias voltage $e\Phi = 0.2\Gamma$

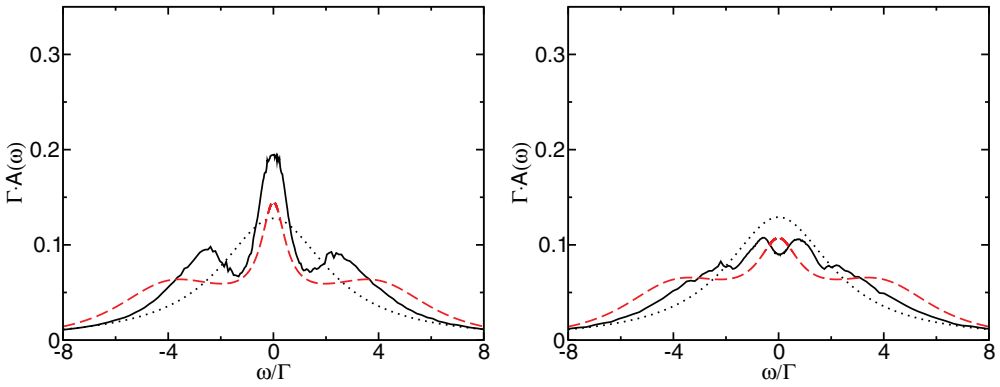

(c) bias voltage $e\Phi = 0.5\Gamma$ (d) bias voltage $e\Phi = 1.0\Gamma$

FIG. 6. (Color online) Nonequilibrium spectral functions for $U = 8\Gamma$ at inverse temperature $\beta = 5\Gamma^{-1}$, as compared to second-order perturbation theory. Line legends are the same as in Fig. 3.

However, the MaxEnt procedure does not clearly predict the correct Hubbard peak positions at $\pm U/2$. A possible reason for this is the partially rather slow decay behavior of the kernel function which was derived for the MaxEnt. It may result in decreased resolution in the high-frequency range, as compared to a conventional MaxEnt procedure for the Wick rotation.

Spectra for interaction strength $U = 10\Gamma$ are displayed in Fig. 7. Again, the solution is very similar to the perturbative prediction, and still a splitting of the ASR at larger bias voltages is observed. The MaxEnt resolution issue for the Hubbard bands is again observed.

C. Approaching lower temperatures

For data at lower temperature, namely $\beta = 10\Gamma^{-1}$, the behavior of MaxEnt solutions is similar to the one described above. Nevertheless, sharper structures, such as the Kondo peak, which emerge at lower temperatures, make the MaxEnt procedure more challenging. A common way to deal with this problem is the so-called "annealing procedure."[13,14] Here, a fine-temperature grid is imposed in order to freeze out low-energy features step by step. The procedure starts with a featureless default model at very high temperatures. At lower temperature, the MaxEnt result of the next higher temperature is used as default model, and so forth, until the target temperature is reached.

We found earlier[4] that it is of great use also within the two-dimensional analytic continuation problem. Also in the present extension of the approach in Ref. 4, the MaxEnt yields more well-behaved solutions if a higher temperature is used as default model. This was investigated by a simple single-step annealing procedure, using results from a $\beta = 5\Gamma^{-1}$ run. In fact, the occurrence of unphysical normalization-violating sidebands may already be avoided in some cases for this rather rough temperature grid. Figure 8 shows two examples in which the one-step annealing procedure was able to improve the results significantly.

D. Transport properties

Using the Meir-Wingreen equation (2), we are able to compute transport properties based on spectral functions resulting from the MaxEnt analytic continuation procedure. Figure 9 compares results obtained at Coulomb interaction strengths $U = 4\Gamma$ and $U = 6\Gamma$ to real-time quantum Monte Carlo data from Ref. 15.

The low-temperature data were obtained without the employment of an expensive annealing procedure: The most distinct feature of the low-temperature data is an increase in current at low voltages for $\beta = 10\Gamma^{-1}$ and $U = 6\Gamma$. It is obtained whether the single-step annealing procedure described above is employed or not.

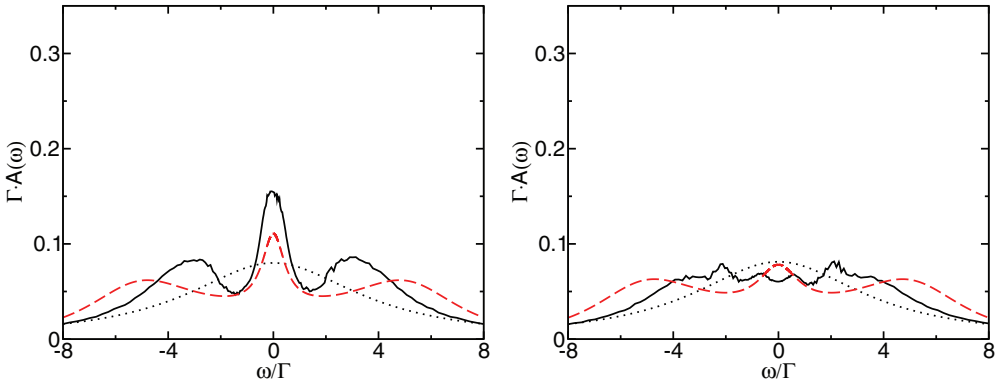

(a) bias voltage $e\Phi = 0.5\Gamma$ (b) bias voltage $e\Phi = 1.0\Gamma$

FIG. 7. (Color online) Nonequilibrium spectral functions for $U = 10\Gamma$ at inverse temperature $\beta = 5\Gamma^{-1}$, as compared to second-order perturbation theory. Line legends are the same as in Fig. 3.

As compared to the real-time QMC calculations, we obtain a good agreement at interaction strength $U = 4\Gamma$. The only significant deviation is at $e\Phi = 0.25$, the value at which we observed the overshooting of the quasiparticle peak in the spectral function earlier on. At higher interaction $U = 6\Gamma$, the current predicted by our method appears to be systematically higher at voltages $e\Phi > 0.2\Gamma$, for both temperatures. This is again consistent with the observation that, with increasing U, the ASR is probably overshooting its actual value for values within the range $0.125\Gamma < e\Phi \leqslant 0.5\Gamma$.

In the following, we discuss the low-voltage region of both cases, $U = 4\Gamma$ and $U = 6\Gamma$. As shown in the previous section, in the case $\beta\Gamma = 5$, the quasiparticle weight is underestimated in the voltage range $e\Phi \leqslant 0.125\Gamma$ for the reason that $i\varphi_m = 0$ data cannot be taken into account for the analytic continuation. This is compatible with the fact that the current is underestimated as compared to the $\beta\Gamma = 10$ data, as well as the real-time QMC data.

Figure 10 shows current-voltage curves for different values of U at $\beta\Gamma = 10$. In any case, an S-shaped current-voltage characteristics is obtained, the first increase of which is due to the ASR, and the second of which is due to the Hubbard bands. The reduced weight of the ASR at increased interaction brings about an earlier departure of the $U = 8\Gamma$ curve as compared to the curves at $U = 4\Gamma$ and $U = 6\Gamma$. The same is true for the $U = 6\Gamma$ curve as compared to the case $U = 4\Gamma$.

E. Comparison to the single-wedge approach from a practical point of view

We briefly illustrate the practical benefit of using the present algorithm as compared to the single-wedge approach proposed in our earlier publication.[4] A comparison of the two analytic continuation methods is shown in Fig. 11, for $\beta = 10.0\Gamma^{-1}$, $U = 6\Gamma$, and $e\Phi = 0.5\Gamma$.

While it is straightforward to implement, the previously proposed *single-wedge method* has a grave disadvantage: Due to the underlying geometrical structure of the single wedge, one has to provide a rather large number of Monte Carlo data, also from large Matsubara frequencies, to the MaxEnt procedure to include nontrivial information about spectral functions at nonzero bias voltage. Unfortunately, doing this usually drives the MaxEnt into a numerically unstable regime. As a consequence, slightly different selections of input data may yield very different spectral functions which, however, can often be identified as unphysical. Therefore, one has to introduce some *ad hoc* criteria[4] to filter such bogus spectral functions. The same holds true for the selection of the opening

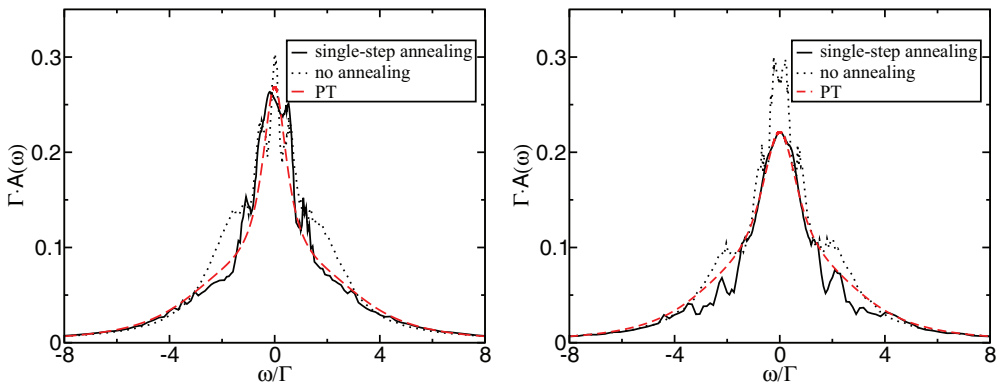

(a) bias voltage $e\Phi = 0.5\Gamma$ (b) bias voltage $e\Phi = 1.0\Gamma$

FIG. 8. (Color online) Lower-temperature spectral functions as inferred for $U = 4\Gamma$, $\beta = 10\Gamma^{-1}$ with or without an annealing step. The default model for the single-step procedure is taken from temperature $\beta = 5\Gamma^{-1}$.

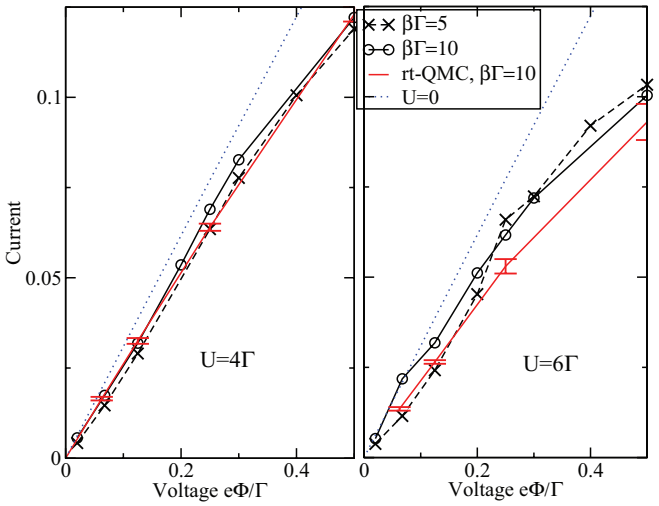

FIG. 9. (Color online) Transport characteristics as compared to real-time QMC data from Ref. 15.

angle of the single wedge; there is no *a priori* way to select an appropriate wedge opening angle for a given system. Consequently, from one simulation one can obtain a collection of different results from the single-wedge analytic continuation method introduced in Ref. 4. The left panel in Fig. 11, for example, shows that by slightly changing ("+1" data point or "+6" data points), the "fine-tuned" selection from the same QMC input data set, the final result is different and often erroneous. Also note that for the fine-tuned choice of the QMC input configuration to the MaxEnt, a numerically equivalent covariance measurement of the QMC data again yields an unphysical spectrum.

In contrast, our *multiwedge approach* is numerically stable over a wide range of input data selections. It also does not require an *a posteriori* tuning of some parameter like the opening angle of a single wedge. As usual, only the principal branch cuts of the Green's function must not be crossed by the selected data set. This profound improvement in stability comes at the price of a computationally much more involved MaxEnt

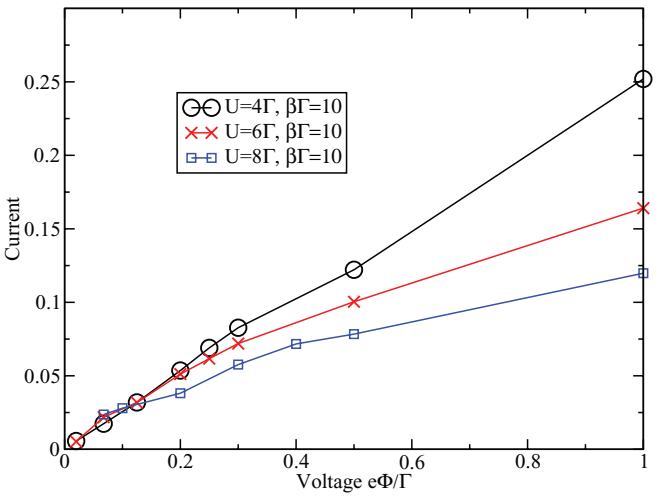

FIG. 10. (Color online) Current as a function of the voltage for different interaction strengths.

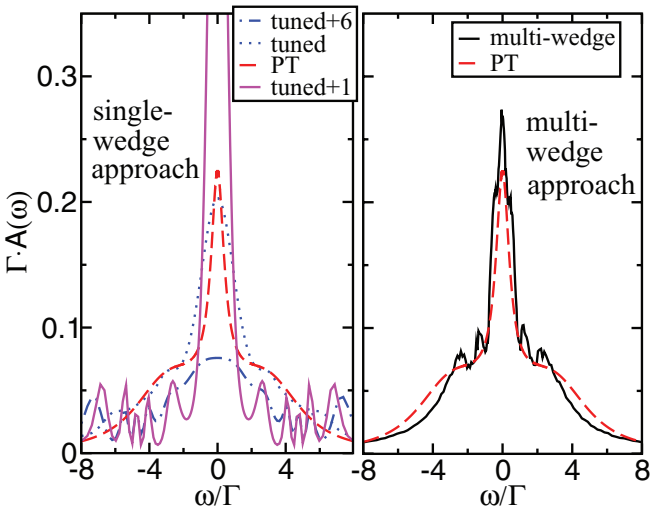

FIG. 11. (Color online) Comparison of the single-wedge approach from Ref. 4 and the multiwedge approach at $U = 6\Gamma$, $\beta\Gamma = 10$, $e\Phi = 0.5\Gamma$.

procedure. Furthermore, to understand and be able to control how it works an explicit knowledge of function theory of several complex variables is mandatory. The two-dimensional (2D) spectral function is very much interlinked with the global structure of the Green's function by partially encoding the branch cut structure. As a consequence, the default model has to be constructed including this prior knowledge and all functions occurring in the MaxEnt procedure have to be handled properly with respect to their function-theoretical meaning. This especially means that the behavior at infinity of the central object in the 2D continuation, the 2D generalized spectral function $\tilde{A}(\varphi,\omega)$, has to be modeled very carefully, a requirement which is unimportant for a conventional 1D continuation, as well as the from the point of view of the single-wedge continuation. The spectrum shown in the right panel in Fig. 11 is the result of this procedure. The previously mentioned selection of the default model was accomplished by adjusting the default model parameters until the posterior probability as determined by the MaxEnt was maximal. Note that the numerical representation of the kernel is not fully optimal yet; but even at this stage, the result is much more reliable than that from the single-wedge method.

Let us add a final remark for practical purposes based on the properties which were just elaborated. When implementing our MaxEnt approaches to the double analytic continuation within the Matsubara-voltage formalism, it is best to start with the single-wedge approach and validate equilibrium spectral functions ($\Phi = 0$) as done in Ref. 4 in order to verify that QMC statistics are incorporated properly. The step to nonzero Φ, i.e., nonequilibrium, is then to implement the multiwedge kernel, which contains single-wedge kernels as building blocks, and plug it into the MaxEnt program. This second step also requires a higher level of knowledge regarding the function-theoretical structures involved. Also note that the present algorithm leaves much room for improvement, since there are many numerical aspects which are still far from being optimal in our implementation: Previously mentioned was the numerical representation of the kernel. A second important problem

is a careful annealing procedure for successively lowering temperatures. A third and major problem as one approaches the Kondo limit is the further incorporation of corrections to the multiwedge approach, as elaborated in Sec. V.

In the next section of the paper, mathematically involved details of the structure of the Green's function are analyzed systematically. It comes along with an introduction of the relevant concepts of the theory of several complex variables. Those are, in particular, needed for the derivation of the MaxEnt inverse problem, Eq. (72), which leads to the results discussed in the present section. The latter mathematical derivation is provided in Sec. IV. It may be convenient to skip Sec. III on first reading and directly go to the MaxEnt derivations and discussions of Sec. IV.

III. SEVERAL COMPLEX VARIABLES AND THE GREEN'S FUNCTION

We want to provide a detailed physicist's introduction to the basic mathematical structures of functions with several complex variables, essential for a full understanding of the Green's function within the Matsubara-voltage formalism. In particular, we attempt to answer the question by deciding which means of intuition from conventional function theory is appropriate or misguiding in the context of dynamic expectation values.

As the next step we describe the analytic structure of dynamic correlation functions $G(z_\varphi, z_\omega)$ appearing as a fundamental object in the Matsubara-voltage formalism (see paper I for details) by means of the function theory for multiple complex variables. Uniqueness of the mathematical procedure involved in the analytical continuations is proven and the connection to MaxEnt approaches for the inference of spectral functions is made.

A. Holomorphy of functions of several complex variables

In order to discuss the notion of holomorphy in the context of functions with several complex variables we partially follow the book by Vladimirov.[16]

A function G of one complex variable is *holomorphic* at a point z_0, if and only if the Cauchy-Riemann differential equation

$$\left.\frac{\partial G}{\partial \bar{z}_\omega}\right|_{z_0} = 0 \tag{3}$$

is satisfied. The notion for holomorphy of functions of several complex variables is a natural extension of this definition: A function $f(\underline{z})$, with $\underline{z} \in \mathbb{C}^d$, is holomorphic with respect to $\underline{z}$ at the point $\underline{z}^{(0)}$ if and only if it is holomorphic with respect to each individual variable,

$$\left.\frac{\partial f}{\partial \bar{z}_i}\right|_{\underline{z}^{(0)}} = 0, \quad i = 1, \ldots, d. \tag{4}$$

Note that in the following we always denote vectors in $\mathbb{C}^d (d > 1)$ by an underlined symbol such as $\underline{z}$. *Hartogs' fundamental theorem* asserts that definition (4) is also equivalent to the Weierstraß definition of holomorphy for several variables. The latter calls a function holomorphic at $\underline{z}_0$ if and only if there exists an open neighborhood M of $\underline{z}^{(0)}$, such that for all $\underline{z} \in M$ the function f may be written as an absolutely convergent power series $f(\underline{z}) = \sum_{|\alpha|=0}^{\infty} a_\alpha (\underline{z} - \underline{z}^{(0)})^\alpha$. α denotes the multi-index for the monomial $\underline{z}^\alpha := \prod_{n=0}^{d} z_n^{\alpha_n}$, and $|\alpha| := \sum_{n=0}^{d} \alpha_n$. An analytic complex function of several variables is holomorphic.

The notion of holomorphy implied by Eqs. (4) is thus as natural and intuitive as in the 1D case.

B. Domains of holomorphy and biholomorphic transformations

The major qualitative difference between single- and multivariable complex analysis is contained in the notion of a domain and the geometric equivalence among holomorphic functions arising from classes of domains. This has far-reaching consequences to the theory itself, such as the construction of integral representations. In the context of our formalism we aim at integral representations. We thus first comment on the basic structures on which integral representations operate. Furthermore, we point out the most prominent differences to conventional function theory. The notion of a domain in single-variable complex analysis is replaced with the notion of a *domain of holomorphy* in multivariable complex analysis; the notion of a conformal map is replaced by the notion of a *biholomorphic map*. We will address the most prominent differences by first reminding the reader of basic structural properties of 1D complex analysis and then introducing the corresponding terminologies of the more-dimensional theory.

1. One-dimensional function theory

In 1D complex analysis, *domains* are defined as open connected subsets of $\mathbb{C}$. For the time being, we restrict the discussion to simply connected open sets, i.e., open connected sets with no holes.

Conformal maps between domains U, V, namely functions

$$m : U \to V, \quad z \mapsto m(z), \tag{5}$$

which are holomorphic and invertible (one to one), provide links between certain classes of domains. The *Riemann mapping theorem* states that conformal maps between any simply connected $U \neq \mathbb{C}, \emptyset$ and the unit disk exists. That is, all simply connected domains $\neq \mathbb{C}, \emptyset$ are conformally equivalent: Their structures of holomorphic functions map one to one to each other and are conformally diffeomorphic. Generalizing the concept of holomorphy to Riemannian surfaces, conformal maps exist only for surfaces of the same topological genus. The *uniformization theorem* finds that for simply connected Riemann surfaces (topological genus 0) up to conformal equivalence three classes exist:

(i) the unit disk $D_1 = \{z \in \mathbb{C} : |z| < 1\}$,
(ii) the complex plane $\mathbb{C}$,
(iii) the Riemann sphere $\mathbb{C} \cup \{\infty\}$.

These three surfaces form the so-called moduli space of genus 0, defined as the space of conformally inequivalent Riemann surfaces of genus 0. In general, the size of the moduli space of a Riemann surface of genus g grows as a function of g. Each modulus represents an equivalence class of holomorphic functions. Conformal equivalence plays an important role in physical applications such as 2D potential flows around airfoils or conformal quantum field theory.

One natural consequence of the conformal equivalence of all nonempty simply connected domains $U \subsetneq \mathbb{C}^1$ is that there always exists a function which is not analytically continuable beyond the domain: The function

$$f_0(z) = \sum_{\alpha=0}^{\infty} z^{\alpha!} \tag{6}$$

is holomorphic on the unit disk but may not be analytically continued to larger domains.[16] Using a conformal map m from the unit disk to U, which exists due to the Riemann mapping theorem, one finds the function $f_0 \circ m^{-1}$ which cannot be analytically continued beyond U. One also calls the unit disk the *domain of holomorphy of* f_0, i.e., the largest domain for which f_0 is holomorphic. U is the domain of holomorphy of $f_0 \circ m^{-1}$. For a given domain G, *if* there exists any function f for which G is the largest possible domain in which f is holomorphic, the domain is called a *domain of holomorphy*.

In general, any domain is also a domain of holomorphy in conventional complex analysis. Due to the simple structures arising from these far-reaching equivalences, the conventional function theory of one complex variable is widely considered to be a finalized field of mathematical research.

2. Multidimensional function theory

The two final statements of the last section are completely incorrect for several complex variables $\mathbb{C}^d$, $d \geqslant 2$.

In several complex variables,

(i) a domain is *not necessarily* a domain of holomorphy;

(ii) domains of holomorphy are *usually not* biholomorphically equivalent.

An example of a domain which is no domain of holomorphy is the hollow sphere (see paragraph b below), because *all* analytic functions in the hollow sphere can be analytically continued to the sphere. As compared to 1D function theory, the emerging structures are thus very rich. Depending on the domain geometry, very different *sheaves of holomorphic functions*[17] will arise.

(a) Biholomorphic maps. The tool of a biholomorphic map, as mentioned in the second point, is the generalization of a conformal map to several complex variables. If a holomorphic mapping $m : U \to U'$, with $U, U' \subset \mathbb{C}^d$ is invertible, it is called a *biholomorphic map*. Two domains U, U' are *biholomorphically equivalent*, if and only if such a map exists. They will have an equivalent sheaf of holomorphic functions. Biholomorphic maps do not necessarily preserve angles. Therefore, they are usually not conformal. Nevertheless, with respect to the holomorphic structure, they are the natural generalization of conformal maps on $\mathbb{C}$, because they are complex diffeomorphisms: The inverse of a biholomorphic map is also holomorphic.[16]

(b) Domains of holomorphy and holomorphic envelopes. A striking example of a domain $\subset \mathbb{C}^2$ which is not a domain of holomorphy is given by the hollow sphere $M := \{\underline{z} = (z_1, z_2)^T \in \mathbb{C}^2 : \frac{1}{2} < \sqrt{|z_1|^2 + |z_2|^2} < 1\}$. In sharp contrast to the single-variable case, one can show that *any* holomorphic function $f : M \to \mathbb{C}$ may be analytically continued to the unit sphere. The unit sphere is, in fact, a domain of holomorphy and is thus named the *holomorphic envelope* of M (Ref. 16). This extends to the famous result by Friedrich Hartogs that isolated singularities are always removable for analytic functions $\mathbb{C}^d \to \mathbb{C}$, $d \geqslant 2$ (*Hartogs' lemma*). While isolated singularities play an essential role in the residue calculus in the $d = 1$ case, the $d \geqslant 2$ case is, due to Hartogs' result, of an entirely different nature. As we see in Sec. III C the theory of integral representations of complex functions for $d \geqslant 2$ has consequently a very different character as compared to the $d = 1$ case.

Since ordinary domains such as the hollow sphere are rather friendly as far as analytic continuation is concerned, mathematicians restrict to the systematic study of corresponding envelopes of holomorphy, i.e., the *domains of holomorphy*. One can show that a domain is a domain of holomorphy if and only if it is a so-called *pseudoconvex* domain. Pseudoconvexity is a certain generalization of convexity from $\mathbb{R}^d$ to $\mathbb{C}^d$ (Ref. 16). For this reason, the fundamental domains of holomorphy in our application, the wedges, are indeed convex (cf. Sec. III D).

(c) Biholomorphic equivalence. In order to provide a classification of domains of holomorphy in $\mathbb{C}^d$, $d \geqslant 2$, the fruitful strategy from $d = 1$, namely using biholomorphic equivalences, is adopted. Nonempty simply connected domains of holomorphy $\subsetneq \mathbb{C}^d$ are usually not biholomorphically equivalent. There are many different types of holomorphic structures, depending on the domain geometry.

A prominent example of biholomorphically inequivalent domains of holomorphy is given by the unit ball $|\underline{z}| < 1$ and the bicylinder $D_1 \times D_1$ in $\mathbb{C}^2$. The unit ball in higher dimensions is with regard to the holomorphic structure in no way related to the unit disks and carries, in fact, a rather singular holomorphic structure.

C. Integral representations

As one might have already guessed from Hartogs' lemma and the domain dependence of the mathematical structures, finding an analogy to Cauchy-like integral representations, yielding, for example, the spectral representation of our two-variable Green's function, turned out to be a cumbersome task.

At present, one knows several, more or less general, possibilities to construct such representations, even with different dimensions of the integration manifolds. The Bochner-Martinelli representation[16] is, for example, probably the most general integral representation, but the integration manifold is $2d - 1$-dimensional.

For our practical purposes, a minimal integration space dimension is, of course, most desirable to reduce the number of fitting variables when reconstructing the function by a MaxEnt-like Bayesian inference technique.

1. The Shilov boundary

In $d = 1$ complex analysis, Cauchy's integral representation reconstructs all values of a simply connected open domain of finite radius using the limit values on the topological boundary, *as long as the boundary values are continuous*. That is, the structure on the topological boundary determines the structure of the interior.

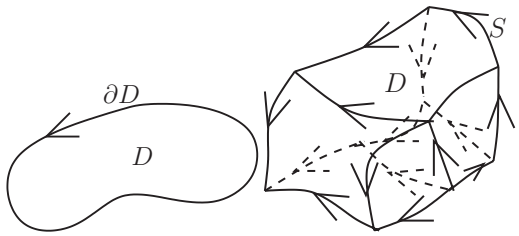

(a) Cauchy ($d = 1$) (b) Bergman-Weil ($d = 2$)

FIG. 12. Comparison of Cauchy and Bergman-Weil integral representation theories. Integrations run over (a) the full topological boundary ∂D and (b) the Bergman-Shilov boundary $S \subset \partial D$ of an analytic polyhedron, respectively.

For $d > 1$, the topological boundary can, in this sense, be reduced to an often much smaller set, the so-called *distinguished* or *Bergman-Shilov boundary*.[18] In the 1930s, Stefan Bergman discovered the distinguished boundary in the context of $\mathbb{C}^2$ for bounded domains with piecewise smooth boundaries. He found that under certain regularity conditions, an integral representation with respect to an only 2D manifold S of all intersections of the smooth boundaries was possible, using the so-called Bergman kernel function. A precise geometric and analytic description of these results is provided in great detail in Chap. XI of Ref. 22. A pictorial comparison of the resulting *Bergman-Weil representation* to the Cauchy formula is provided in Fig. 12. These concepts where independently discovered by Shilov in the 1940s in the rather different context of commutative Banach algebras.[18]

(a) Generalization. In the modern terminology, the Shilov boundary, as a generalization of the Bergman-Shilov boundary, may be defined for any compact space *with respect to* an algebra of continuous complex-valued functions on the space.[18] If we, for example, find physical constraints imposing certain conditions to the set of holomorphic functions, the Shilov boundary with respect to these functions may be reduced to a smaller set. If a sufficiently elaborate kind of integral representation is used, this may enable us to again reduce the number of linear fit parameters significantly in the Bayesian inference problem.

(b) Examples. For the domains with piecewise smooth boundaries which Bergman investigated, S is given by the unification of all possible intersections between the smooth boundary hypersurfaces as long as certain regularity conditions hold. We return to our two examples from Sec. III B 2 c, the *bicylinder* and the *unit sphere*, and comment on their Bergman-Shilov boundaries.

The bicylinder, $D_1 \times D_1$, is one of the most easily accessible domains of holomorphy, because it simply factorizes into two D_1 disks in $\mathbb{C}$. A minimal integral representation of a holomorphic function which is continuous on the closure $\overline{D_1 \times D_1}$, is simply given by the product of two conventional Cauchy representations (see Theorem 2.2.1 in Ref. 19),

$$f(\underline{z}) = \frac{1}{(2\pi i)^2} \iint_{S_1 \times S_1} d^2\zeta \, \frac{f(\underline{\zeta})}{\prod_k (z_k - \zeta_k)}. \tag{7}$$

Therefore, the Bergman-Shilov boundary of $D_1 \times D_1$ is given by the only 2D toroidal subset $S_1 \times S_1 = \partial D_1 \times \partial D_1$ of the 3D topological boundary $\partial(D_1 \times D_1) = \partial D_1 \times D_1 \cup D_1 \times \partial D_1$. Similarly, integral representations of domains which are direct products of $\mathbb{C}^1$ domains can be constructed from the conventional Cauchy integral formula.

It was already mentioned in Sec. III B 2 c that the *unit sphere* in $\mathbb{C}^2$ is not biholomorphically equivalent to the bicylinder. In contrast to the two connected smooth boundary hypersurfaces of the bicylinder, the boundary hypersurface of the unit sphere is not even a smooth hypersurface in Bergman's notion. One can show that here the Bergman-Shilov boundary is, in fact, identical to the topological boundary. Thus, any integral representation for holomorphic functions in domains such as the unit sphere must invoke at least *three* real integrals. It is an example of the strong distinguishments which have to be made between certain classes of domains of holomorphy.

D. Holomorphic structure of the Green's functions

As a next step, we systematically analyze the mathematical structure of the Green's function arising in the Matsubara-voltage approach. The bare Green's function with respect to the two variables $i\varphi_m, i\omega_n$ reads[1]

$$G_0(i\varphi_m, i\omega_n) = \sum_{\alpha=\pm 1} \frac{\Gamma_\alpha / \Gamma}{i\omega_n - \alpha(i\varphi_m - \Phi)/2 - \varepsilon_d + i\Gamma \mathrm{sgn}_{nm}}. \tag{8}$$

Here, $\mathrm{sgn}_{nm} := \mathrm{sgn}(\omega_n - \alpha\varphi_m/2)$. Performing the analytic continuations $i\omega_n \to z_\omega$, $i\varphi_m \to z_\varphi$, the sign function in the denominator results in an ambiguity, as far as the definition of domains, for which G_0 is holomorphic, is concerned.

Choosing a branch cut structure which corresponds to the continuation

$$\mathrm{sgn}(\omega_n \pm \varphi_m/2) \to \mathrm{sgn}(\mathrm{Im}\, z_\omega \pm \mathrm{Im}\, z_\varphi/2) \tag{9}$$

appears to be most sensible from both a mathematic and a physical point of view.

From the former perspective, in contrast to other choices the resulting domains are also *domains of holomorphy* and are thus "maximal" with respect to the holomorphic structure. The four domains of holomorphy are given by $\mathbb{C}^2$ separated into wedges by the two branch cut hyperplanes $\mathrm{Im}\, z_\omega \pm \mathrm{Im}\, z_\varphi/2 = 0$ [see Fig. 13(a)]. From the latter, it is just the imaginary part of the linear combinations of z_ω and z_φ, appearing in the denominators of perturbative expressions in U, which yields the crucial sign-switching δ functions generating the nonanalytic terms separating the domains for which G is holomorphic. See, e.g., Appendix B of paper I.

Consequently, for a finite interaction $U \neq 0$, the appearance of a branch cut must be expected for any new kind of linear combination of z_ω and z_φ in the denominators of the integrands in the perturbation expansion. For example, second-order perturbation theory from Ref. 1 indicated that particle-hole bubbles create higher-order branch cuts $\mathrm{Im}\, z_\omega - \frac{\gamma}{2}\mathrm{Im}\, z_\varphi = 0$, with $\gamma \in \mathbb{Z}$ odd, due to the structure of convolutions which are involved. In a later publication[11] it was pointed out that vertex corrections seem to introduce yet another branch cut for $\mathrm{Im}\, z_\varphi = 0$. The physical retarded Green's function is then

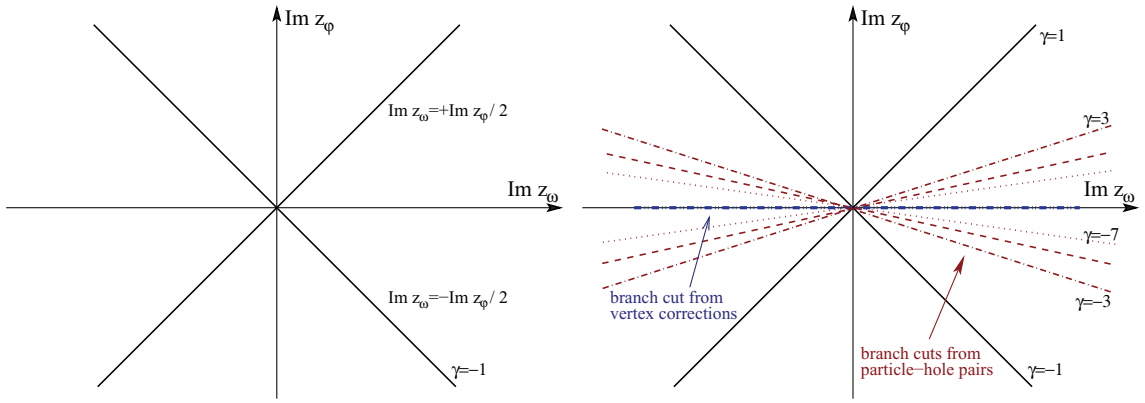

(a) branch cut structure of $G_0(z_\varphi, z_\omega)$ (b) branch cut structure of $G(z_\varphi, z_\omega)$

FIG. 13. (Color online) Branch cut structure of the Green's function. The fully interacting structure is obtained from the perturbative expansion in U/Γ.

given by

$$G_{\text{ret}}(\omega) = \lim_{z_\omega \to \omega + i0^+} \frac{\lim_{\delta_\varphi \to 0^+} + \lim_{\delta_\varphi \to 0^-}}{2} G(\Phi + i\delta_\varphi, z_\omega); \tag{10}$$

i.e., one has to average over the two possible limits with respect to δ_φ.

Note that the latter subtlety was not taken into account in the direct continuation using the cone C_ε in Ref. 4 and also not in the initial approach in Ref. 1.

1. Resulting mathematical assumptions

The following assumptions are being made for the mathematical structure of the Green's function.

(1) By means of holomorphy, we obtain conelike constraints for the combinations of imaginary parts, as depicted in Fig. 13(b). More precisely, we require G to be a solution of the Cauchy-Riemann equations (4) for any $\underline{z}^{(0)}$ *except for those* $\underline{z}^{(0)}$ *for which*

$$\operatorname{Im} z_\omega^{(0)} = \frac{\gamma}{2} \operatorname{Im} z_\varphi^{(0)} \quad \text{or} \quad \operatorname{Im} z_\varphi^{(0)} = 0, \tag{11}$$

with some $\gamma \in 2\mathbb{Z} + 1$. Those $\underline{z}^{(0)}$ define the branch cut hyperplanes and delimit the wedges for which G is holomorphic.

(2) We require the interacting Green's function $G(\underline{z})$ to be bounded, i.e.,

$$\sup_{\underline{z} \in \mathbb{C}^2} |G(\underline{z})| < \infty. \tag{12}$$

(3) We assume that the Green's function $G(\underline{z})$ is *uniquely* defined by the discrete function values $G(i\varphi_m, i\omega_n)$, which are obtained from the effective-equilibrium computations. That is, we require that the continuation to a multisheeted holomorphic function,

$$G(i\varphi_m, i\omega_n) \to G(z_\varphi, z_\omega), \tag{13}$$

is unique.

The second assumption is justified by the structure of the convolution equations in perturbation theory and the boundary conditions that terms $e^{i\varphi_m \beta/2}$ and $e^{i\omega_n \beta}$, evaluate to 1 and -1 before the analytic continuations are carried out.

A proof of the third statement, which is, of course, crucial for the physical theory itself, will be provided in Appendix A. It is based on assumptions 1 and 2 and assumption 3′, which sharpens the requirements on the $\underline{z} \to \infty$-asymptotics:

(3′) Given arbitrary $\underline{x}^{(0)} \in \mathbb{R}^2 \setminus \{0\}$ and $\zeta \in \mathbb{C}$, we have

$$\lim_{\zeta \to \infty} |\zeta G(\zeta \underline{x}^{(0)})| < \infty \Leftrightarrow x_\omega^{(0)} \neq \pm x_\varphi^{(0)}/2. \tag{14}$$

In other words, $G(\underline{z})$ is required to decay like a usual Green's function as a function of ζ, where $\underline{z} = \zeta \underline{x}^{(0)}$, if and only if $\underline{x}^{(0)}$ satisfies the *regularity condition* $x_\omega^{(0)} \neq \pm x_\varphi^{(0)}/2$.

2. Justification of assumption 3′

Assumption 3′ may be justified as follows.

Consider the absolute value of the free Green's function (8),

$$|G_0(z_\varphi, z_\omega)| \leqslant \sum_{\alpha = \pm 1} \frac{\Gamma_\alpha}{\Gamma} \frac{1}{|(z_\omega - \alpha(z_\varphi - \Phi)/2 - \epsilon_d + i\Gamma \operatorname{sgn} \operatorname{Im}(z_\omega - \alpha z_\varphi/2)|}.$$

It is obvious that it decays $\propto \frac{1}{\zeta}$ when $z_\varphi = \zeta x_\varphi^{(0)}$ and $z_\omega = \zeta x_\omega^{(0)}$ for the nonsingular combinations of $x_\varphi^{(0)}$ and $x_\omega^{(0)}$. It does not decay at all in the singular cases $x_\omega^{(0)} = \pm x_\varphi^{(0)}/2$.

It is easy to check that interaction $U > 0$ does not change this *high-energy structure*. Let us examine the second-order self-energy expression [Eq. (15) in

Ref. 1]:

$$\Sigma^{(2)}(\underline{z}) = U^2 \sum_{\alpha_i} \left[\prod_{i=1}^{3} \int d\epsilon_i \, \frac{\Gamma_{\alpha_i}}{\Gamma} \right] \times \frac{f_{\alpha_1}(1-f_{\alpha_2})f_{\alpha_3} + (1-f_{\alpha_1})f_{\alpha_2}(1-f_{\alpha_3})}{z_\omega - (\alpha_1 - \alpha_2 + \alpha_3)\frac{z_\varphi - \Phi}{2} - \epsilon_1 + \epsilon_2 - \epsilon_3},$$

with $f_{\alpha_i} = f(\epsilon_i - \alpha_i \Phi/2)$.

Due to the structure of the denominator, we see that on top of the singular directions of the bare Green's function, $x_\omega^{(0)} = \pm x_\varphi^{(0)}/2$, we also have the singular directions $x_\omega^{(0)} = \pm\frac{3}{2}x_\varphi^{(0)}$.

Consequently, assumption 3′ is incorrect for the second-order *self-energy*. Nevertheless, when inserted into Dyson's equation,

$$G^{(2)}(\underline{z}) = \frac{G_0(\underline{z})}{1 - G_0(\underline{z})\Sigma^{(2)}(\underline{z})}, \tag{15}$$

we see that for the directions $x_\omega^{(0)} = \pm\frac{3}{2}x_\varphi^{(0)}$ the limiting behavior of G_0 is adopted, i.e., the behavior (14).

Note that the uniqueness proof of the appendix also holds when directly applied to the self-energy, because the singular directions of the second-order perturbation theory, $x_\omega^{(0)} = \pm\frac{3}{2}x_\varphi^{(0)}$, are not required to be regular in the proof. This is because the direction $x_\omega^{(0)} = \pm\frac{3}{2}x_\varphi^{(0)}$ also defines a branch cut (assumption 1).

E. Tubular cone domains ("wedges")

As we have seen, the structure of G_0 combined with the structure of convolutions in the perturbation theory with respect to U indicates that the numerous branch cut hyperplanes divide $\mathbb{C}^2$ into several, in fact infinitely many, wedges of the form $T^C = \mathbb{R}^2 + iC$. C is by definition a convex cone with its vertex at zero. See also the pictorial discussion in Ref. 4. Due to the convexity of C, T^C is pseudoconvex and thus a domain of holomorphy.[16] In the mathematical classification scheme, domains like these are called tubular cone domains.

1. Geometry of the cones

We briefly introduce certain notions of the description of the analytic geometry of cones in $\mathbb{R}^d$. This is necessary to thoroughly follow the mathematical formulas which are involved in the description of the analytic structure of T^C. The cone C with vertex at zero is formally defined by the scaling property $\underline{x} \in C \Rightarrow \forall\, \lambda > 0 : \lambda\underline{x} \in C$.

Its *dual cone* C^* is defined via the standard scalar product

$$(\underline{\xi},\underline{x}) := \sum_{k=1}^{d} \xi_k x_k; \quad \underline{\xi},\underline{x} \in \mathbb{R}^d, \tag{16}$$

by

$$C^* := \{\underline{\xi} \in \mathbb{R}^d \mid \forall\, \underline{x} \in C : (\underline{\xi},\underline{x}) \geqslant 0\}. \tag{17}$$

C^* represents the space of positive semidefinite linear functionals on C when the functional form (16) is considered. The dual cone is important because the construction of kernel functions often involves Fourier transforms.

A *convex cone* is a cone for which the straight line between any pair of points within the cone is also contained by the cone.

We also use the analytic continuation of the scalar product (16) with respect to $\underline{x}$. We continue $\underline{x} \to \underline{z}$ holomorphically in (16):

$$(\underline{\xi},\underline{z}) := \sum_{k=1}^{d} \xi_k z_k; \quad \underline{\xi} \in \mathbb{R}^d, \underline{z} \in \mathbb{C}^d. \tag{18}$$

2. Analytic structure and biholomorphic equivalence classes

Tubular cones and domains are well-known objects in the theory of several complex variables, because they naturally arise in certain fields of mathematics. As a consequence, many efforts were put in for a detailed understanding of their structure. In the prominent physical example, axiomatic quantum field theory, the cones represent forward and backward light cones, in 4D spacetime, $d = 4$. A celebrated result was Bogolyubov's edge-of-the-wedge theorem.[20] Mathematical examples include Fourier analysis, functional analysis, the theory of hyperfunctions, and the theory of partial differential equations.

A key component of the wedge is given by its edge, namely the real subspace associated with the vertex of the cone. Because in our case the vertex is located at zero, the edge of the wedge T^C can be formally identified with an oriented copy of the real subspace,

$$\mathrm{Edge}_{T^C} := \mathbb{R}^d + i0^C, \tag{19}$$

where 0^C is an infinitesimal vector within the cone C. Although there exist, depending on the direction approaching the origin within C, several infinitesimals 0^C, the Edge is well-defined through (19), because all infinitesimals in C are obviously equivalent with respect to holomorphic continuation in T^C. T^C may be regarded as a generalization of the upper half plane.

Let C, C' be arbitrary convex cones in $\mathbb{R}^d$, $C \neq C'$. T^C and $T^{C'}$ are in general *not* biholomorphically equivalent. This means that the sets of holomorphic functions living on them are structured differently. Wedges within the space $\mathbb{C}^2$ are fortunately an exception to this rule: *T^C and $T^{C'}$ are biholomorphically equivalent for any combination C, C'.* See also the introductory notes in the corresponding part of the second volume of Ref. 21. In $\mathbb{C}^2$, biholomorphisms between T^C and $T^{C'}$ may be constructed easily using complexified rotations and dilations of $\mathbb{R}^2$: Consider that the real (nonsingular) matrix $M : \mathbb{R}^2 \to \mathbb{R}^2, \underline{x} \mapsto \left(\begin{smallmatrix} a & b \\ c & d \end{smallmatrix}\right)\underline{x}$ maps C to C', i.e., $C' = MC$. The corresponding biholomorphism between T^C and $T^{C'}$ is obtained from the complexified map $\tilde{M} : \mathbb{C}^2 \to \mathbb{C}^2, \underline{z} \mapsto \left(\begin{smallmatrix} a & b \\ c & d \end{smallmatrix}\right)\underline{z}$. It is easy to see that $T^{C'} = MT^C$ and that M is holomorphic and invertible.

If the complexified linear map is a rotation, we also call it a *biholomorphic rotation* when we want to emphasize the biholomorphic character of the mapping.

Note that the helpful notion of the Bergman-Shilov boundary is *not* directly applicable to T^C, because T^C is *unbounded*. However, as discussed next, sequences of bounded domains approaching T^C from its interior may be used to understand the holomorphic structure on T^C.

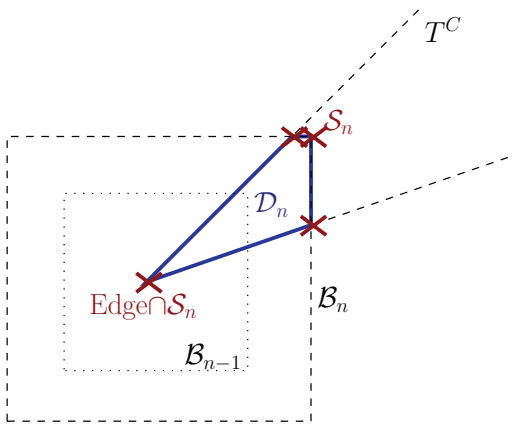

FIG. 14. (Color online) An artist's impression of asymptotically filling the wedge T^C with the sequence $\mathcal{D}_n$. $\mathcal{D}_n$ is a domain with piecewise smooth boundaries created by intersecting with a growing bicylinder $\mathcal{B}_n$, creating the analytic polyhedra $\mathcal{D}_n$. The corresponding sequence of Bergman-Shilov boundaries improperly converges to the set Edge $\cup\{\infty\}$. Therefore, the sheaf of holomorphic functions on T^C is solely characterized by its edge values and its asymptotic behavior $\underline{z}\to\infty$.

3. Bergman-Weil representations

A sequence of bounded domains $\mathcal{D}_n \subset T^C$, $\lim_{n\to\infty}\mathcal{D}_n = T^C$, with piecewise smooth boundaries like in [Fig. 12(b)] may be easily constructed, such that the edge of the wedge contains a part of the Bergman-Shilov boundary $\mathcal{S}_n$ of $\mathcal{D}_n$ and such that the other subsets of $\mathcal{S}_n$ disappear to ∞ as $n\to\infty$. In our case, $d=2$, an explicit construction of such a sequence may be obtained by intersecting T^C with a growing bicylinder $\mathcal{B}_n := R_n(D_1\times D_1)$, $\mathcal{D}_n := \mathcal{B}_n\cap T^C$, with radius $R_n\propto n$. The procedure is sketched in Fig. 14. One finds that the sequence of Bergman-Shilov boundaries improperly converges to

$$\mathcal{S}_\infty := \mathrm{Edge}_{T^C}\cup\{\infty\}, \tag{20}$$

where "∞" informally denotes the point or merely a list of points which emerge when T^C is, depending on the holomorphic structure, compactified suitably. At first glance, each direction for approaching ∞ might yield a different point in $\{\infty\}$. The points "∞" carry the additional information which is necessary to turn the structure on Edge_{T_C} into a unique description of the holomorphic structure on T^C.

The Bergman representation for an analytic polyhedron in $\mathbb{C}^2$ may be obtained by the following, rather technical, procedure, whose details are not particularly relevant but enable us to investigate rather explicitly the structure of a suitably large class of holomorphic functions on a wedge. An excellent pedestrian's introduction to it is provided by Bergman's original monograph, Ref. 22. The book also provides a comprehensive introduction to the Bergman-Shilov boundary and biholomorphic maps, using the example of analytic polyhedra. Equations of the form

$$\zeta^{(k)} = \mathfrak{f}^{(k)}(\underline{z},\lambda_k), \tag{21}$$

with $\lambda_k\in\Lambda_k\subset\mathbb{R}, k=1,\ldots,K$, where $\mathfrak{f}^{(k)}(\underline{z},\lambda_k)$ are λ-parametrized families of analytic functions of $\underline{z}$, shall define the analytic polyhedron. Each equation yields a surface in $\underline{z}$ space for a given λ and a hypersurface h_k in $\underline{z}$ space as λ is varied continuously. The mutual intersections $S_{kl} = h_k\cap h_l$ yield the Bergman-Shilov boundary surface $S=\bigcup_{k,l}S_{kl}$. S_{kl} is then parametrized by a function $\underline{z}=\mathfrak{g}^{(kl)}(\lambda_k,\lambda_l)$. A holomorphic function f on the analytic polyhedron may then be written with respect to the Bergman-Shilov boundary of the latter using the *Bergman kernel function*

$$B_{kl} = \left|\frac{\partial\left(\mathfrak{g}_1^{(kl)},\mathfrak{g}_2^{(kl)}\right)}{\partial(\lambda_k,\lambda_l)}\right|\left(\frac{\mathfrak{f}_l(z_1,z_2,\lambda_l)\mathfrak{f}_k\left(z_1,\mathfrak{g}_2^{(kl)},\lambda_k\right)}{\left(\mathfrak{g}_1^{(kl)}-z_1\right)\left(\mathfrak{g}_2^{(kl)}-z_2\right)}\right.$$
$$\left.-\frac{\mathfrak{f}_k(z_1,z_2,\lambda_k)\mathfrak{f}_l\left(z_1,\mathfrak{g}_2^{(kl)},\lambda_l\right)}{\left(\mathfrak{g}_1^{(kl)}-z_1\right)\left(\mathfrak{g}_2^{(kl)}-z_2\right)}\right). \tag{22}$$

The integral representation with respect to $f|_S$ then reads

$$f(\underline{z}) = -\frac{1}{8\pi^2}\sum_{k\neq l}\int_{\lambda_k,\lambda_l}\frac{f\left(\mathfrak{g}_1^{(kl)},\mathfrak{g}_2^{(kl)}\right)B_{kl}}{\mathfrak{f}^{(k)}(\underline{z},\lambda_k)\mathfrak{f}^{(l)}(\underline{z},\lambda_l)} \tag{23}$$

and can be applied directly to our $\mathcal{D}_n$ domains.

An explicit test on whether a Bergman integral representation for G_0 on the $\mathcal{D}_n=\mathcal{B}_n\cap T^C$ domains is feasible yields that the subsets of $\mathcal{S}_n$ which go to ∞ may *not* be neglected for $G(\underline{z})$ functions. This is because $G_0(\underline{z})$ has a nonzero limit as $\underline{z}\to\infty$ if one goes along the cross-shaped submanifold $\mathrm{Re}\,z_\omega = \pm\mathrm{Re}\,z_\varphi/2$ and keeps $\mathrm{Im}\,\underline{z}$ constant. Due to the independence of $\mathrm{Im}\,\underline{z}$ this problem occurs for each of the wedges. Hence, the Bergman kernel function (22) is only of limited use for us. We thus do not go into further details of this rather clumsy computation here.

The formal use of the sequence $\mathcal{D}_n$ enables us to see very explicitly that the Edge of T^C is with respect to the representation (22) the only carrier of structural information which involves finite values of $\underline{z}$. The rest of the information, then uniquely defining the holomorphic structure on T^C, is encoded in the several possible classes of limiting behavior as $\underline{z}$ approaches infinity.

4. Cauchy-Bochner integral representation

As a straightforward consequence of this, assuming a certain limiting behavior of the considered set of functions on T^C, integral representations with respect to the Edge $\mathbb{R}^d+i0^C$ may be derived. Even more generally, a constraint on the function class which also limits the Edge behavior, can be imposed in such a way that the Edge function yields a unique description. The several possible $\underline{z}\to\infty$ behaviors are then, using the information from the constraint, encoded in the Edge. This appears to be linked deeply to the extension of the notion of the Bergman-Shilov boundary to the notion of the Shilov boundary mentioned in the course of Sec. III C1: Considering a subset of the sheaf of holomorphic functions on a certain (compactified) domain may cause the Shilov boundary to "shrink."

We now discuss one of the earliest developments going beyond simply restricting the considered function set such that a naive extrapolation of Bergman representations, like in Fig. 14, holds. It was another extension of the Cauchy integral formula with respect to tubular cones by Salomon Bochner. He considers a function f which is holomorphic on T^C and

satisfies the constraint

$$\|f(\underline{x}+i\underline{y})\| \leqslant M_{\epsilon,f}(C')e^{\epsilon|\underline{y}|}, \tag{24}$$

which has to hold for any compact cone $C' \subset C$ and for any $\epsilon > 0$, where $M_{\epsilon,f}(C')$ is a suitably chosen real number. $\|\cdot\|$ is a norm which integrates out the $\underline{x}$ variable, $\|f(\underline{x}+i\underline{y})\|^2 := \int d^dx\, |f(\underline{x}+i\underline{y})|^2$ (Ref. 16).

Inequality (24) constrains the limiting behavior $\underline{z} \to \infty$ in a sufficiently strong way such that an integral representation with respect to the Edge may be constructed.

Namely, the Cauchy-Bochner representation then allows a function f satisfying (24) to be written as

$$f(\underline{z}) = \frac{1}{(2\pi)^d}\int d^dx'\, \mathcal{K}_C(\underline{z}-\underline{x}')f(\underline{x}'+i0^C), \tag{25}$$

with the Edge values $f(\underline{x}'+i0^C)$. Here, the so-called *Cauchy kernel*[16] of the cone C, defined as

$$\mathcal{K}_C(\underline{z}) := \int_{C^*} d^d\xi\, e^{i(\underline{\xi},\underline{z})}, \tag{26}$$

was introduced. It is straightforward to compute the Cauchy kernel for our wedges with this formula: see the Appendix of Ref. 4. For our purposes, we provide a general but easily applicable expression for further numerical and analytical computations in Sec. III G.

Unfortunately, as in the Bergman approach, a numerical test of Eq. (25) for $f = G_0$ using an arbitrary wedge for which G_0 is holomorphic shows that the Cauchy-Bochner representation (25) is also incorrect for G_0. As a consequence, we find that the Green's function does not satisfy (24). This is compatible with the fact that the left-hand side of (24) diverges in the case $f = G_0$, no matter which C' is considered.

Nevertheless, as we will see, the Cauchy-Bochner kernel (26) will serve as a building block for the construction of an exact integral representation for a different class of holomorphic functions which, in fact, contains the holomorphic branches of our Green's function $G(\underline{z})$ on the respective wedges. As such, it is essential as a connection of real-time and imaginary-time structure of the Green's function.

5. *The tubular octant* $\mathbb{H}\times\mathbb{H}$ *and biholomorphic equivalence to the bicylinder*

Due to the biholomorphic equivalence of all T^C in $\mathbb{C}^2$ any of our wedges which arise for the Green's function may be mapped biholomorphically to the tubular octant $\mathbb{H}\times\mathbb{H} = \mathbb{R}^2 + i\,(\mathbb{R}^+\times\mathbb{R}^+)$, where $\mathbb{H}$ is the upper half plane of $\mathbb{C}$. This domain may itself be mapped biholomorphically to the bicylinder $D_1 \times D_1$ via a piecewise Möbius transformation of the coordinates. *Hence, all wedges of the Green's function are biholomorphically equivalent to the bicylinder.* Let us denote a corresponding biholomorphism by $\mathfrak{m}_C : T^C \to D_1 \times D_1$. We would like to comment on this due to the striking simplicity of the bicylinder and of domains which are direct products of $\mathbb{C}^1$ domains with respect to the construction of integral representations. From the point of view of this construction, the tubular octant may be regarded as the simplest representant of the biholomorphic equivalence class of all wedges in $\mathbb{C}^2$.

Due to the premises of the Cauchy integral formula, a usage of the representation (7) for the biholomorphically transformed sheaf of holomorphic functions is feasible in case the transformed Green's function $G|_{T^C}\circ\mathfrak{m}_C^{-1}$ is continuous on its topological boundary $\partial(D_1\times D_1)$. Note that under the biholomorphic transformations, $S_1\times S_1$ is mapped to the edges of the T^C wedges. The "∞" in T^C maps to "∞" in $\mathbb{H}\times\mathbb{H}$ under biholomorphic transformation, and that again maps biholomorphically, using the componentwise Möbius transformation $\frac{z_k-i}{z_k+i}$ to the points $\mathfrak{p}_\infty := \{1\}\times S_1 \cup S_1\times\{1\}$. Note that the points $\mathfrak{p}_\infty \subset \partial(D_1\times D_1)$ are also part of the distinguished boundary torus $S_1\times S_1$.

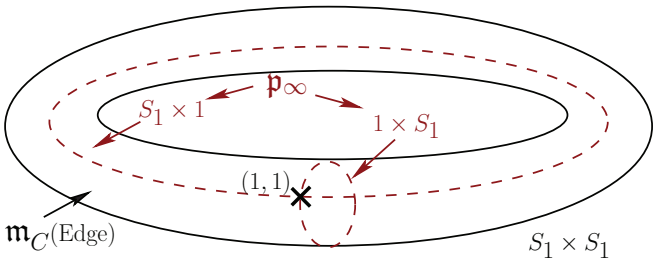

FIG. 15. (Color online) On the distinguished boundary surface of the bicylinder, the picture of Edge_{T^C} under the componentwise Möbius transformation $\mathfrak{m}_C$ is delimited by the dash-dotted lines $\mathfrak{p}_\infty$. A discontinuity of $G|_{T^C}\circ\mathfrak{m}_C^{-1}$ occurs at the intersection point (1,1) of the two circles and prevents a Cauchy representation from being applicable. The violation of the Cauchy-Bochner condition (24) appears to be related to the occurrence of the discontinuity.

The boundary behavior of the transformed Green's function $G|_{T^C}\circ\mathfrak{m}_C^{-1}$ is not continuous at the intersection point (1,1) of the two circles $\mathfrak{p}_\infty$, due to the properties of $G_0|_{T^C}$ at ∞ leading to singular directions, as summarized in assumption 3′ of Sec. III D. An illustration may be found in Fig. 15.

Therefore, using the biholomorphic equivalence to the bicylinder is not immediately helpful for the construction of an integral representation of the Green's function G. Nevertheless, it is essential in the application of Vladimirov's approach, which is the subject of the next section.

F. Vladimirov's integral formula

Vladimirov provided a generalization of the so-called Herglotz-Nevanlinna representation for the upper half plane to tubular cone domains. His investigations were motivated by applications in the field of linear passive systems in mathematical physics.[4,21,23] Due to its generality, the approach is applicable to the analytic wedges of the interacting Green's function G.

1. *Herglotz-Nevanlinna representation* ($d = 1$)

We discuss the conventional Herglotz formulas. Herglotz' representation theorem considers holomorphic functions in the open unit disk D_1 which have a positive real part, the so-called Carathéodory functions.[24–26] By separating a phase factor out of the function one can also consider functions with positive or negative imaginary part, and so on. Since the open unit disk can be conformally mapped to the upper half plane $\mathbb{H}$, using the Möbius transformation $\frac{z-i}{z+i}$, as mentioned above, the representation can under certain circumstances be also used for $\mathbb{H}$.

By considering Carathéodory functions, Herglotz' theorem only imposes assumptions on the positivity of the real (imaginary) part of the function. In contrast to Cauchy's integral formula, no assumptions about the behavior of the Carathéodory functions on the boundary of the disk are made, such as the continuity.

The theorem states that every Carathéodory function f can be represented by

$$f(z) = i\,\mathrm{Im}\, f(0) + \int_0^{2\pi} \frac{e^{it}+z}{e^{it}-z}\, d\sigma(t)\,, \tag{27}$$

where $d\sigma$ is a non-negative finite measure.[24]

Regarding a different set of functions, a formally very similar representation is the so-called *Poisson formula*, which is the analog of the Cauchy formula to the real analysis of harmonic functions (solutions of Laplace's equation), and can, in fact, be derived from it. It provides an integral kernel for the solution to the Dirichlet problem for the Laplace equation on the unit disk in $\mathbb{R}^2$. For a *continuous* function $\mathfrak{f} : \partial D_1 \to \mathbb{R}$ it makes it possible to construct a harmonic function $u : D_1 \to \mathbb{R}$ as follows (see pp. 169ff. in Ref. 27):

$$u(z) = \frac{1}{2\pi}\mathrm{Re} \int_0^{2\pi} \frac{e^{it}+z}{e^{it}-z}\mathfrak{f}(e^{it})\, dt\,. \tag{28}$$

A comparison of Eqs. (27) and (28) shows that the measure $d\sigma$ of the Herglotz formula is, in fact, defined by the (possibly singular) boundary limit of the holomorphic function.

As a natural extension of the Poisson formula, the *Schwarz integral formula* reconstructs a holomorphic function f on the *closed* unit disk from the real part of its boundary values, up to a constant imaginary offset. It reads (p. 171 in Ref. 27)

$$f(z) = i\,\mathrm{Im}\, f(0) + \frac{1}{2\pi} \int_0^{2\pi} \frac{e^{it}+z}{e^{it}-z} f(e^{it})\, dt\,. \tag{29}$$

Apparently, the only formal difference between Eqs. (28) and (29) is the different measure.

Due to the conformal equivalence, for a holomorphic function f on the *closed* upper half plane $\mathrm{Im}\, z \geqslant 0$, under the assumption that there is an $\alpha > 0$ for which $|z^\alpha f(z)|$ is bounded, one has the Schwarz representation in the following form:

$$f(z) = \frac{1}{\pi i} \int_{-\infty}^{\infty} \frac{\mathrm{Re}\, f(x+i0^+)}{x-z}\, dx\,. \tag{30}$$

Note the formal equivalence to the spectral representation of a conventional Matsubara Green's function, $G(z) = \int dx\, \frac{1}{-\pi} \frac{\mathrm{Im}\, G(x+i0^+)}{z-x}$.

Similarly, the Poisson kernel for the closed upper half plane is

$$P_y(x) = \frac{y}{x^2+y^2}, \tag{31}$$

yielding the representation

$$u(x+iy) = \frac{1}{\pi} \int_{-\infty}^{\infty} P_y(x-t)\mathfrak{f}(t)\, dt\,, \tag{32}$$

with $\mathfrak{f} \in L^p(\mathbb{R})$.

The full Herglotz-Nevanlinna representation of arbitrary analytic functions with positive real part for the *open* upper half-plane reads[23]

$$f(z) = \frac{z+i}{\pi i} \int \frac{d\mu\,(x')}{(x'-i)(x'-z)} - \frac{1}{\pi} \int \frac{d\mu\,(x')}{1+x'^2} - iaz + b. \tag{33}$$

Here, μ is given by the boundary-value distribution of $\mathrm{Re}\, f$:

$$\mu = \mathrm{Re}\,\mathrm{bv}\, f, \tag{34}$$

where the operation bv denotes the boundary value distribution of the function and $\mu(x)$ "=" $\mathrm{Re}\, f(x+i0^+)$. The linear coefficient

$$a = \mathrm{Re}\, f(i) - \frac{1}{\pi} \int \frac{d\mu\,(x')}{1+x'^2}\,, \tag{35}$$

and the constant term $b = \mathrm{Im}\, f(i)$.

For example, in the case of the function $f(z) = i/\pi z$, μ is the Dirac measure $\mu(x) = \mathrm{Re}\,\mathrm{bv}\, f = \delta(x)$ and the coefficients $a = b = 0$. The case $\mu(x) = -a\delta(x)$ is not permitted by construction.

At first glance, Eqs. (30) and (32) and the connection to the Herglotz-Nevanlinna representation (33) seem to be rather straightforward applications of the Cauchy integral formula. However, attempting the multidimensional generalization, we found that in our case, $d > 1$, the Cauchy-Bochner way of invoking $\mathcal{K}_C$ for a representation, Eq. (26), is not valid for the noninteracting Green's function $G_0|_{T^C}$; see Sec. III E 4. Remarkably, as found in Sec. III E5, taking assumption 2 from Sec. III D in to account, we find that when transformed to the bicylinder, the Green's function $G|_{T^C} \circ \mathfrak{m}_C^{-1}$ is closely related to a Carathéodory function, but the Cauchy-Bochner representation is invalid.

These subtleties are apparently reflected by the central assumption (24) of Cauchy-Bochner representations.

2. *Functions with positive real or imaginary part in T^C*

Note that the representation (33) can be also used for bounded functions on the upper half plane. This can be seen by formally introducing a shift in f which makes the real part of the function of consideration positive definite.

While the signs of its real and imaginary parts will vary, the Green's function $G|_{T^C}$ is, in fact, a bounded function, assumption (12). This is why Vladimirov's integral representation for functions with positive imaginary part turned out to be applicable.[4] Let us denote the set of holomorphic functions with positive imaginary parts on T^C by $H_+(T^C)$. Due to the biholomorphic equivalence of the Green's function's wedges to the bicylinder, one may think of $H_+(T^C)$ as a generalization of the Carathéodory functions. Note that in the literature, sometimes functions with positive real and sometimes functions with positive imaginary parts are considered, resulting in marginal differences in the equations.

3. *Vladimirov's kernel functions for T^C*

We now study the generalization of the Herglotz-Nevanlinna representation to d-dimensional wedges.[21,23] Vladimirov's approach may be found for positive *real* parts in Ref. 23 and for positive *imaginary* parts in Ref. 21. Because our original work[4] referred to Ref. 21 we would like to switch to considering the class of functions with positive *imaginary* part,

$H_+(T^C)$, in the following. Let us first introduce Vladimirov's generalizations of the Poisson and Schwarz kernels, using the Cauchy kernel $\mathcal{K}_C$ from Eq. (26) as a starting point.

The (generalized) *Poisson kernel* for the wedge T^C is defined by[21]

$$\mathcal{P}_C(\underline{z}) := \frac{|\mathcal{K}_C(\underline{z})|^2}{(2\pi)^d \mathcal{K}_C(2i\,\underline{y})}; \quad \underline{z} = \underline{x} + i\,\underline{y}. \tag{36}$$

In case of the tubular octant, it is the product of usual Poisson kernels; however, it is no longer simply proportional to the imaginary part of the Cauchy kernel. The (generalized) *Schwarz kernel with respect to a point* $\underline{z}^{(0)} = \underline{x}^{(0)} + i\,\underline{y}^{(0)} \in T^C$ is given by

$$\mathcal{S}_C(\underline{z},\underline{z}^{(0)}) := \frac{2\mathcal{K}_C(\underline{z})\overline{\mathcal{K}_C(\underline{z}^{(0)})}}{(2\pi)^d \mathcal{K}_C(\underline{z} - \overline{\underline{z}^{(0)}})} - \mathcal{P}_C(\underline{x}^{(0)},\underline{y}^{(0)}). \tag{37}$$

For a measure $\mu(\underline{x})$ we call

$$P_C[\,d\mu\,](\underline{z}) := \int d\mu(\underline{x})\, \mathcal{P}_C(\underline{z} - \underline{x}) \tag{38}$$

the *Poisson integral with respect to* μ.

4. Vladimirov's theorem

We already pointed out that in the case $d \geqslant 3$ two arbitrary different wedges, T^C and $T^{C'}$, are usually *not* biholomorphically equivalent. In particular, the wedge T^C is not necessarily biholomorphically equivalent to $\mathbb{H}^d$ when $d \geqslant 3$. Hence, one may expect the structural similarity to the Carathéodory functions to break down more easily in higher dimensions. This is the reason why Vladimirov's d-dimensional generalization[21] of Herglotz' theorem is stated in a comparably cryptic way which will simplify considerably in our case $d = 2$, for the reasons above.

Theorem: (Vladimirov, 1978/79). The following conditions for a function $f \in H_+(T^C)$ are equivalent for a cone $C \subset \mathbb{R}^d$ and $\mu(\underline{x}) := \mathrm{Im}\, f(\underline{x} + i0^C)$:

(1) The Poisson integral $P_C[\,d\mu\,]$ is pluriharmonic in T^C;

(2) the function $\mathrm{Im}\, f(\underline{z})$, $\underline{z} = \underline{x} + i\,\underline{y} \in T^C$, is represented by the Poisson formula

$$\mathrm{Im}\, f(\underline{z}) = P_C[\,d\mu\,](\underline{z}) + (\underline{a},\underline{y}), \tag{39}$$

for some $\underline{a} \in C^*$, where C^* is the dual cone of C;

(3) for all $\underline{z}^0 \in T^C$, under the assumption that C is regular, the Schwarz representation

$$f(\underline{z}) = i \int_{\mathbb{R}^d} \mathcal{S}_C(\underline{z} - \underline{t},\underline{z}^0 - \underline{t})\, d\mu(t) + (\underline{a},\underline{z}) + \underline{b} \tag{40}$$

holds, with $b = b(\underline{z}^0) = \mathrm{Re}\, f(\underline{z}^0) - (\underline{a},\underline{x}^0)$. ■

Note that pluriharmonic functions are the natural multidimensional generalization of harmonic functions. A regular cone C in our context is a cone for which $1/\mathcal{K}_C$ is nonsingular in T^C. In the cases $d = 1,2,3$ all pointed cones are regular.[23]

Using the equivalence of all T^C in the case $d = 2$, in Ref. 4 we verified that the first statement of the theorem is true for $G|_{T^C}$. This is so because it is known from the literature (see Ref. 23, p. 134) that the Poisson integral is pluriharmonic for any function $H_+(\mathbb{H}^d)$. Due to the biholomorphic equivalence of all T^C to $\mathbb{H}^2$ in $\mathbb{C}^2$, the two integral representations provide exact relations for all holomorphic sheets of the interacting Green's function. A parametrization of the Green's function with respect to their Edge values is gained by this. In our case, the validity of the representation is due to the biholomorphic equivalences first shown by Korányi and Pukánsky's work on the polycylinder.[28]

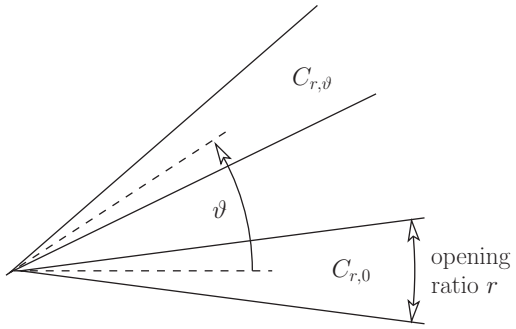

FIG. 16. An arbitrary cone C with 0 as vertex can be parametrized by an opening ratio r and an orientation angle ϑ. The rotation R_ϑ which maps $C_{r,0}$ to $C_{r,\vartheta}$ induces a biholomorphism between $T^{C_{r,0}}$ and $T^{C_{r,\vartheta}}$.

Note that the linear growth term $\underline{a}$ is zero for the Green's function, because it is bounded, as required by assumption (12).

G. Application to the Green's function

It turns out to be reasonable to specify a given cone domain arising from the branch cut structure by an angle ϑ and an opening ratio r (see Fig. 16). It is sufficient to consider the case $\vartheta = 0$ first, because relations for finite ϑ may be reconstructed from biholomorphic rotations, as explained in Sec. III E 2.

1. Kernels for $\vartheta = 0$

For the case $\vartheta = 0$, a computation of the kernels $\mathcal{K}_{C_{r,\vartheta}}$ and $\mathcal{P}_{C_{r,\vartheta}}$ has been provided in the appendix of Ref. 4 already, where the opening ratio r was named ε for technical reasons.[29]

We used the definition

$$C_{r,\vartheta} := \bigcup_{\lambda\in(-r,r)} \{(x_1,x_2) \in \mathbb{R}^2 \,|\, x_2 > 0 \wedge x_1 = \lambda x_2\} \tag{41}$$

and computed the Cauchy and Poisson kernels via Eqs. (26) and (36). The resulting Cauchy kernel is

$$\mathcal{K}_{C_{r,0}}(\underline{z}) = -2r \prod_{\mu=\pm1} \frac{1}{rz_2 - \mu z_1}, \tag{42}$$

and the resulting Poisson kernel is

$$\mathcal{P}_{C_{r,0}}(\underline{z}) = \frac{r}{\pi^2} \prod_{\mu=\pm1} \frac{ry_2 - \mu y_1}{(rx_2 - \mu x_1)^2 + (ry_2 - \mu y_1)^2}. \tag{43}$$

We have not used an explicit formula for the Schwarz kernel (37) yet, because the occurrence of the reference point $\underline{z}^{(0)}$ appears to introduce additional technical complications. The shape of Eq. (43) is so simple because it can be computed from the tubular octant, whose Poisson kernel is the product of usual Poisson kernels. A simple real-valued 2×2 matrix acts as the biholomorphism which converts the two representations.

2. Operator notation

In order to put a stronger emphasis on the functional-analytic nature of the integral representations which interrelate edge and wedge values of the Green's function, let us introduce an operator notation for the Poisson integral and also for the biholomorphic rotations.

Let us denote the set of all *a priori* admitted Green's functions on T^C by $\mathcal{G}_C$. By "*a priori* admitted" we mean those analytic functions $G|_{T^C} : T^C \to \mathbb{C}$ for which axiom 2 from Sec. III D holds (T^C has to comply with axiom 1). Furthermore, let us denote the corresponding space of boundary value distributions (edge functions) $G|_{T^C}(\underline{x} + i0^C)$ by $\mathcal{E}_C$.

In order to focus on the Poisson kernel, we introduce the corresponding spaces of imaginary parts, $\mathcal{G}_C^{(I)}$ and $\mathcal{E}_C^{(I)}$. We denote by the operator $\mathcal{P}_C$ the linear map

$$\begin{aligned} &\mathcal{P}_C : \mathcal{E}_C^{(I)} \to \mathcal{G}_C^{(I)}, \\ &\operatorname{Im} G(\underline{x} + i0^C) \mapsto \int dx^2\, \mathcal{P}_C(\underline{z} - \underline{x}) \operatorname{Im} G(\underline{x} + i0^C). \end{aligned} \tag{44}$$

Note that the Schwarz kernel (37) does not directly yield a comparable map from $\mathcal{E}_C$ to $\mathcal{G}_C$, due to the occurrence of the $\underline{z}^{(0)}$ reference point.

Furthermore, the rotation R_ϑ, which maps the cone $C_{r,0}$ to the cone $C_{r,\vartheta}$, induces a biholomorphic map $\tilde{R}_\vartheta : T^{C_{r,0}} \to T^{C_{r,\vartheta}}$ (see Sec. III E 2). At this point we would again like to emphasize that the biholomorphism does not connect the different branches of the Green's function on the wedges. It merely yields a counterpart of a given holomorphic branch on a biholomorphically equivalent wedge which can be formally operated with. It is in that sense that is analogous to the concept of a conformal map. This biholomorphism maps functions $f \in \mathcal{G}_{C_{r,0}}$ to functions $f \in \mathcal{G}_{C_{r,\vartheta}}$. This can be similarly represented by the linear operator

$$\mathcal{R}_\vartheta : \mathcal{G}_{C_{r,0}} \to \mathcal{G}_{C_{r,\vartheta}}, \tag{45}$$

$$f(\underline{z}) \mapsto f\big(\tilde{R}_\vartheta^{-1}(\underline{z})\big). \tag{46}$$

The operator $\mathcal{R}_\vartheta$ also naturally extends to a linear map from $\mathcal{E}_{C_{r,0}}$ to $\mathcal{E}_{C_{r,\vartheta}}$, which we denote by the same symbol $\mathcal{R}_\vartheta$.

3. Kernel functions at finite ϑ

Consequently, for finite ϑ, the Poisson kernel operator of $T^{C_{r,\vartheta}}$ is

$$\mathcal{P}_{C_{r,\vartheta}} = \mathcal{R}_\vartheta \mathcal{P}_{C_{r,0}} \mathcal{R}_\vartheta^{-1}. \tag{47}$$

Equivalently, the Poisson kernel function of $T^{C_{r,\vartheta}}$ is given by

$$\mathcal{P}_{C_{r,\vartheta}}(\underline{z}) = \mathcal{P}_{C_{r,0}}\big(R_\vartheta^{-1}\underline{z}\big). \tag{48}$$

In practical computations, the function can be evaluated combining Eq. (43) and the rotation matrix

$$R_\vartheta^{-1} = \begin{pmatrix} \cos\vartheta & -\sin\vartheta \\ \sin\vartheta & \cos\vartheta \end{pmatrix}. \tag{49}$$

4. Edge properties of G_0

Since we essentially reduced the structure of the Green's function to the edge values of their holomorphic branches, it seems worthwhile to investigate the edge structure of G_0, and later also the perturbative structure of the theory in U, more carefully. See Sec. III I for the deeper analysis.

The edge limit of the bare Green's function (8), as a function of the edge orientation ϑ, is given by

$$G_0^{(\text{edge})}(\vartheta;\underline{x}) = \sum_{\alpha=\pm1} G_0^{(\text{edge}),\alpha}(\vartheta;\underline{x}), \tag{50}$$

where

$$G_0^{(\text{edge}),\alpha}(\vartheta;\underline{x}) = \frac{\Gamma_\alpha/\Gamma}{x_\omega - \alpha(x_\varphi - \Phi)/2 - \varepsilon_d + i\Gamma \operatorname{sgn}_\vartheta} \tag{51}$$

and

$$\operatorname{sgn}_\vartheta := \operatorname{sgn}\left(\cos\vartheta - \frac{\alpha}{2}\sin\vartheta\right). \tag{52}$$

Apparently, the edge function only changes as a function of ϑ whenever $\cos\vartheta \pm \sin\vartheta/2$ crosses zero. This reflects the equivalence of all directions

$$\underline{x} + i0^\vartheta := \underline{x} + i\begin{pmatrix} \sin\vartheta \\ \cos\vartheta \end{pmatrix}0^+ \tag{53}$$

when approaching the edge within a holomorphic branch T^C, as discussed in Sec. III E 2. The edge function changes whenever ϑ crosses a branch cut, namely for the following singular orientations in the interval $[0,2\pi)$:

$$\begin{aligned} &\vartheta_1^{(\text{sing})} = \arctan 2; \quad \vartheta_2^{(\text{sing})} = \pi - \arctan 2; \\ &\vartheta_3^{(\text{sing})} = \pi + \arctan 2; \quad \vartheta_4^{(\text{sing})} = 2\pi - \arctan 2. \end{aligned} \tag{54}$$

These are the angles corresponding to the four half lines emerging from the origin in Fig. 13(a). The orientations $\vartheta_i^{(\text{sing})}$ are also identical to the singular directions of assumption 3′ in Sec. III D.

There is another subtle feature of the edge behavior of the bare Green's function. The real part,

$$\operatorname{Re} G_0^{(\text{edge})}(\vartheta;\underline{x}) = \sum_{\alpha=\pm1} \frac{\frac{\Gamma_\alpha}{\Gamma}[x_\omega - \alpha(x_\varphi - \Phi)/2 - \varepsilon_d]}{[x_\omega - \alpha(x_\varphi - \Phi)/2 - \varepsilon_d]^2 + \Gamma^2}, \tag{55}$$

is completely ϑ independent. As a consequence, for any branch of G_0, the edge limit $\operatorname{Re} G_0(\underline{x} + i0^C)$ is identical.

Another property is that, following the instructions (10) to obtain the physical limit as far as the orientation of the limiting procedure is concerned, the function

$$\tilde{A}_0(\underline{x}) := -\frac{1}{\pi}\operatorname{Im} G_0(\underline{x} + i0^{\vartheta=0}) \tag{56}$$

is positive definite:

$$\tilde{A}_0(\underline{x}) = \sum_{\alpha=\pm1} \frac{\Gamma_\alpha/\pi}{[x_\omega - \alpha(x_\varphi - \Phi)/2 - \varepsilon_d]^2 + \Gamma^2}. \tag{57}$$

In particular, the noninteracting spectral function

$$A_0(\omega) = \tilde{A}_0(\Phi,\omega). \tag{58}$$

Again one can see in Eq. (57) that $\tilde{A}_0$ does not decay to zero as a function of $\underline{x} \to \infty$ along the singular directions $\vartheta_i^{(\text{sing})}$ ($\underline{x}^{(0)}$ in axiom 3′, Sec. III E 2. This is because the singular directions are an essential feature of the edges and lead to a

discontinuity at ∞ when one compactifies the edge as shown in Fig. 15.

H. Bayesian inference of spectral functions

In Ref. 4 we used Vladimirov's integral representation in order to reconstruct a function $\tilde{A}$, which was defined by Eq. (56) for the interacting system. We chose a cone domain with orientation zero, $T^{C_{\varepsilon,0}}$, and assumed the constrained Green's function $G|_{T^{C_{\varepsilon,0}}}$ to be analytic for sufficiently small cone opening ratios ε. This was justified, because the higher-order branch cuts of particle-hole character [see Fig. 13(b)] occur only in high-order terms in U. The vertex-correction type of branch cut pointed out in Ref. 11 was ignored.

Then the standard MaxEnt procedure[5] for inferring spectral functions from quantum Monte Carlo data could be adopted to the inference of $\tilde{A}$ and therefore the spectral function.

The procedure was found to work well in the equilibrium limit, $\Phi = 0$. However, entering the nonequilibrium regime, the ill-posedness of the inverse problem increased. Similar to the intertwined geometric dependencies between the function structures on edge and wedge coming to the surface in the appendix's uniqueness proof, a geometric dependency of the quality of Bayesian inference was found.

Decreasing the parameter ε provided a limit to a holomorphic function (leaving aside the vertex-correction branch cut) on the one hand, but on the other hand increased the ill-posedness of the inverse problem for a finite-Φ spectral function. A discussion of how this is reflected by the structure of the Poisson kernel function may be found in Ref. 4.

Apparently, the problem is very much related to restricting to the sheet $T^{C_{\varepsilon,0}}$ only taking $G(i\varphi_m, i\omega_n)$ data from the sheet into account and *discarding the others*.

The only possible way to alleviate the increasing ill-posedness is to provide a link between the holomorphic branches of the Green's function, being able to take into account data from not one but several wedges in order to perform the analytic continuation (10).

I. Bogolyubov's edge-of-the-wedge theorem

A candidate of such a link was provided by Bogolyubov's famous edge-of-the-wedge theorem in the context of axiomatic quantum field theory. It considered the analytic continuation of Wightman functions[16] in order to establish certain dispersion relations. From a mathematical point of view, it also introduced a generalization of the very notion of analytic continuation.[16]

There are several versions of the theorem. A simple version which captures the essential idea may be found in the book by Hörmander on partial differential operators.[30] It roughly considers two functions $f^{\pm}$ which are holomorphic on the tube cones $T^{\pm C}$, where C is a convex open cone with vertex at zero. Consequently, the edges of T^{C} and T^{-C} are "infinitesimal neighbors." If the functions have the same boundary value distributions, $f^{+}(\underline{x} + i0^{C}) = f^{-}(\underline{x} - i0^{C}) =: f_0$, then f_0 is an analytic function. f_0 provides an analytic continuation of both f^{+} and f^{-}.

In its more general formulations, the theorem actually demands the functions $f^{\pm}$ to be holomorphic only locally at the edge and establishes certain facts about the domain in which f_0 is analytic (global edge-of-the-wedge theorem).

An extension to several cones whose edges meet in a single point is Martineau's theorem. As in Bogolyubov's theorem, locally, holomorphic functions may be found which constitute analytic continuations of pairs of functions living on wedges. Again, the edge values of the considered set of functions have to be interrelated in a more or less direct way.

IV. SYSTEMATIC EXTENSION OF THE CONTINUATION PROCEDURE BY USE OF EDGE RELATIONS

In the previous section, we systematically analyzed the function-theoretical structure of the Green's function with regard to the two complex variables z_ω and z_φ. The former comes along with the analytic continuation of the fermionic Matsubara frequency $i\omega_n$ associated with the dynamical properties of the effective-equilibrium systems. The latter comes along with the analytic continuation with respect to the Matsubara voltage. A fundamental property of the Green's function with regard to the two variables is the branch cut structure shown in Fig. 13(b). It separates the holomorphic sheets of the Green's function which live on wedges. Their edges meet in a branch point. For a holomorphic sheet, we were able to derive an integral representation of the Green's function with regard to two real variables, using kernel functions such as the one in Eq. (43). By this, the function's values on the wedge are represented linearly by boundary values on its edge and vice versa. The physical limit (10) of the theory corresponds to approaching the branch point in Fig. 13(b) along a certain direction. In order to use data from several wedges for physical results, it is thus necessary to find more or less explicit relations between function values on edges of different wedges. The so-called edge-of-the-wedge theorem (Sec. III I) provides some insight along this line. In order to construct an explicit functional-analytic approach to the analytic continuation which would enable us to extend the numerical implementation of the MaxEnt approach, it is only of indirect use, however.

It is clear that any simple relation between edges of the different branches of the Green's function provides a rather direct link between integral representations of the respective wedges. Based on a continuity approximation to function values at the branch point around which the edges are aligned, the present section derives the MaxEnt procedure which was used to infer the numerical results of Sec. II.

A. Continuous real part at branch point

The relation is an exact identity of the bare Green's function. Namely, $\mathrm{Re}\, G_0(\underline{x} + i0^{\vartheta})$ is identical for any edge orientation ϑ of the bare Green's function; see Eq. (55). It is easy to verify that same is true for the second-order self-energy (15) and also for the functions which are parametrized by Han and Heary's original fitting approach in Ref. 1.

We have

$$\mathrm{Re}\, G_0(\underline{x} + i0^{\vartheta}) = \mathrm{Re}\, G_0(\underline{x} + i0^{\vartheta'}), \tag{59}$$

$$\mathrm{Re}\, \Sigma^{(2)}(\underline{x} + i0^{\vartheta}) = \mathrm{Re}\, \Sigma^{(2)}(\underline{x} + i0^{\vartheta'}), \tag{60}$$

for all $\vartheta,\vartheta' \in [0,2\pi)$. This structure is similar to the conventional Green's function causality relation

$$G(z^*) = G(z)^*. \tag{61}$$

There, we consequently have

$$\mathrm{Re}\, G(\omega + i0^+) = \mathrm{Re}\, G(\omega - i0^+). \tag{62}$$

However, in our case we only know for sure the symmetry

$$G(z_\varphi^*, z_\omega^*) = G(z_\varphi, z_\omega)^*. \tag{63}$$

From Eq. (63) only the edge relation

$$\mathrm{Re}\, G(\underline{x} + i0^{\vartheta+\pi}) = \mathrm{Re}\, G(\underline{x} + i0^{\vartheta}),\ \vartheta \in [0,\pi) \tag{64}$$

can be derived. That is, conjugate wedges T^C, T^{-C} carry the same real parts of $G(\underline{z})$ on their edges.

B. Range of the continuity assumption

We now investigate to what extent the relations (59) and (60) also hold for higher-order contributions to the fully interacting Green's function $G(\underline{z})$, i.e., to what extent we *a priori* expect the approximation

$$\mathrm{Re}\, G(\underline{x} + i0^{\vartheta}) \approx \mathrm{Re}\, G(\underline{x} + i0^{\vartheta=0}) \tag{65}$$

to hold. It is insightful to study the algebraic properties of a conventional Green's function $G(z)$ first. Subsequently, the two-variable function $G(\underline{z})$ is discussed with respect to its formal structure and regarding empirical findings from the continuous-time QMC simulation data.

1. Conventional Green's function

As a simple example, let us consider the summation of the Dyson series[10]

$$G = G_0 - G_0\Sigma G = G_0 - G_0\Sigma G_0 + G_0\Sigma G_0\Sigma G_0 \cdots . \tag{66}$$

The entities $G(z)$, $G_0(z)$, and $\Sigma(z)$ satisfy the causality relation (61). For the equation to hold, the product (and the sum) of two Eq. (61)-satisfying quantities $A(z)$, $B(z)$ shall also satisfy Eq. (61). This is obviously the case, because

$$\begin{aligned}\mathrm{Re}\,(AB)(\omega + i0^+) &= \mathrm{Re}\, A(\omega + i0^+)\mathrm{Re}\, B(\omega + i0^+)\\ &\quad -\mathrm{Im}\, A(\omega + i0^+)\mathrm{Im}\, B(\omega + i0^+)\\ &= \mathrm{Re}\, A(\omega - i0^+)\mathrm{Re}\, B(\omega - i0^+)\\ &\quad -[-\mathrm{Im}\, A(\omega - i0^+)][-\mathrm{Im}\, B(\omega - i0^+)]\\ &= \mathrm{Re}\,(AB)(\omega - i0^+).\end{aligned}$$

The same can be shown for the imaginary part. It is crucial to recall that the mutual conjugation of *imaginary parts*of upper and lower functions has been used explicitly for closedness of Eq. (61) under multiplication. In other words, the set of functions with *only* the property (62) is not closed under multiplication.

2. Two-variable Green's function

The closedness under multiplication is, in general, violated for functions with solely a continuous real part on the branch point. This is due to the fact that no statement about the imaginary part is made, and in the case of the causality relation (61), conjugateness of the imaginary parts is needed for closedness of the real part's continuity under multiplication. For instance, one can easily verify that $G_0(\underline{z})G_0(\underline{z})$ yields different real parts on the edges. The same can be shown for $G_0(\underline{z})^{-1}$.

C. Structure of the residual term

Nevertheless, as discussed in this paragraph, we are able to show that the continuity assumption (65) is recovered for a certain energy range. Additionally, empirical findings for the structure of CT-QMC data, as discussed in Appendix B, partially support the assumption by observing continuity relations between edge functions. Last but not least, the assumption is justified *a posteriori* for a rather large collection of wedges via the obtained numerical results (see Sec. IV E for further discussion). It is found in Sec. IV E that including upper (and lower) wedges, $|\omega_n| > |\varphi_m/2|$ (and $|\omega_n| < -|\varphi_m/2|$) into the considered collection of wedges causes the numerical procedure to fail. Otherwise, it converges. This observation is compatible with a strong violation of the continuity assumption at the principal branch cuts $\mathrm{Im}\, z_\omega = \pm \mathrm{Im}\, z_\varphi/2$.

It is insightful to study how the resulting difference of two given edge functions is structured, namely to study the local residue

$$R^{(\vartheta,\vartheta')}(\underline{x}) := \mathrm{Re}\, G(\underline{x} + i0^{\vartheta}) - \mathrm{Re}\, G(\underline{x} + i0^{\vartheta'}) \tag{67}$$

for arbitrary values $\vartheta,\vartheta' \in [0,2\pi)$ as a function of $\underline{x} \in \mathbb{R}^2$.

1. Angular structure

Obviously, due to Eq. (64) we have

$$R^{(\vartheta,\vartheta)} \equiv R^{(\vartheta,\vartheta+\pi)} \equiv 0 \tag{68}$$

for all ϑ. $R^{(\vartheta,\vartheta)} \equiv 0$ if ϑ and $\vartheta'(+\pi)$ belong to the same wedge.

2. Structure due to continuity of imaginary-time data

Using the empirical fact that the CT-QMC data $\Sigma(i\varphi_m, i\omega_n)$ are continuous as a function of φ_m and ω_n, we can derive certain continuity relations for $R^{(\vartheta,\vartheta')}$. They are provided in Appendix B.

3. High-energy structure

Let us also consider the high-energy limit

$$|\underline{x}| \gg \max\{\Gamma, |U|, |\Phi|, |\epsilon_d|\}. \tag{69}$$

For this, $|G(\underline{x} + i0^{\vartheta})|$ is significantly larger than zero only if $x_\omega \approx \pm x_\varphi/2$, according to point 3′ in Sec. III E2. The "+" and "−" cases imply a separation of energy scales. *For both of these two energy scales, the closedness under multiplication is recovered.*

One can easily see the recovery of the multiplicative structure in the high-energy limit by investigating the bare Green's function (50). The "+" and "−" energy scales are given by the $\alpha = -$ and $\alpha = +$ addends (51) in Eq. (50), respectively. Each of the addends satisfies the multiplication rule, because the absolute value of their imaginary part remains the same for all ϑ at fixed $\underline{x}$. The same is true for the sum of

the corresponding $\sum_i \alpha_i = \mp 1$ addends in the second-order self-energy (15).

Therefore, we conclude that

$$\lim_{\underline{x}\to\infty} R^{(\vartheta,\vartheta')} = 0 \text{ for all } \vartheta,\vartheta', \tag{70}$$

in contrast to the limiting behavior of G itself.

4. Consequences for the analytic structure

Hence, although the assumption (65) is apparently only approximate, the error $R^{(\vartheta,\vartheta')}(\underline{x})$ is introduced by assuming the relation is correct around 0 in the $\underline{x}$ space. It is remarkable that the intermediate-coupling numerical data presented in Sec. II appear to be rather precise in the low-energy region, although the violation terms are *a priori* expected to be strong at low energies.

From the *a priori* perspective, the assumption (65) gives a correct picture of how the wedges are related in the high-energy range. When assuming the relation, additional low-energy degrees of freedom have to be introduced in order to reobtain an exact continuation theory (cf. Sec. V). Empirical data discussed in Appendix B indicate that these degrees of freedom are comparably well behaved.

D. Functional-analytic consequences of the shared-real-part assumption

We will see that the continuity assumption (65) leads to a complete description of the function $G(\underline{z})$ on *all* wedges *only* as a function of the single edge $\mathrm{Im}\, G(\underline{x}+i0^{\vartheta=0})$. This is extraordinarily attractive from a numerical point of view, because by this, the number of degrees of freedom when doing the MaxEnt inference is not increased, but *all* imaginary-time theory data $G(i\varphi_m, i\omega_n)$ may be taken into account, without any *a priori* constraint. As in the single-wedge approach of Ref. 4, the spectral function can still be directly extracted from the MaxEnt result. We will see that for functions which comply with the assumption, it in fact alleviates the ill-posedness of the inverse problem, as desired.

1. Construction of the kernel

Starting from Eq. (65) we can derive a representation of the Green's function with respect to $\mathrm{Im}\, G(\underline{x}+i0^{\vartheta=0})$ in the following way. First, we introduce the Hilbert transform operator $\mathcal{H}$ as

$$(\mathcal{H}f)(\underline{x}) := \frac{1}{\pi}\fint dx_2' \, \frac{f(x_1,x_2')}{x_2 - x_2'}. \tag{71}$$

Then we can use condition 3′ (Sec. III D) in order to apply the Hilbert transform for computing real and imaginary parts from each other on the boundary of certain $\mathbb{H}$-isomorphic complex lines.

One can show that

$$\mathrm{Im}\, G|_{T^{C_{r,\vartheta}}} = -\frac{1}{\pi}\mathcal{Q}_{r,\vartheta}\,\mathrm{Im}\, G(\underline{x}+i0^{\vartheta=0}), \tag{72}$$

where we introduced the operator

$$\mathcal{Q}_{r,\vartheta} := \mathcal{P}_{r,\vartheta}\mathcal{R}_\vartheta \mathcal{H}\mathcal{R}_\vartheta^{-1}\mathcal{H}. \tag{73}$$

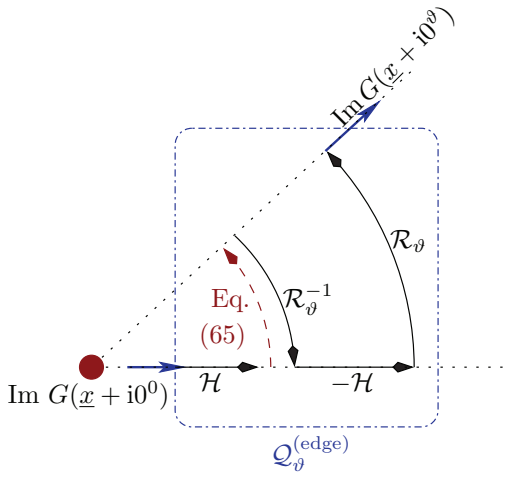

FIG. 17. (Color online) Action of the operator $-\mathcal{Q}_\vartheta^{(\mathrm{edge})}$. It translates between functions living on edges of wedges with two different angular orientations. The orientation ϑ is the one of the considered data wedge, and 0 is the orientation of the physical limiting procedure (10). Initially acting on the physical edge function, the consecutive formal operations which comprise $-\mathcal{Q}_\vartheta^{(\mathrm{edge})}$ either change the angular rotation or leave it invariant, as indicated by the respective arrows.

Let us also introduce a symbol for the right part of the operator sequence,

$$\mathcal{Q}_\vartheta^{(\mathrm{edge})} := \mathcal{R}_\vartheta \mathcal{H}\mathcal{R}_\vartheta^{-1}\mathcal{H}. \tag{74}$$

The action of $-\mathcal{Q}_\vartheta^{(\mathrm{edge})}$ on $\mathrm{Im}\, G(\underline{x}+i0^{\vartheta=0})$ is depicted in Fig. 17: First, the Hilbert transform $\mathcal{H}$ with respect to the x_ω variable yields $\mathrm{Re}\, G(\underline{x}+i0^{\vartheta=0})$. Then, via Eq. (65) it is identified with $\mathrm{Re}\, G(\underline{x}+i0^{\vartheta})$. In order to obtain $\mathrm{Im}\, G(\underline{x}+i0^{\vartheta})$ one formally has to transform to the biholomorphic equivalent of $G|_{T^{C_{r,\vartheta}}}$ in the domain $T^{C_{r,0}}$ via the operator $\mathcal{R}_\vartheta^{-1} = \mathcal{R}_{-\vartheta}$. The inverse Hilbert transform $-\mathcal{H}$ yields the imaginary part of the edge value of the function $T^{C_{r,0}} \to \mathbb{C}$, $\underline{z} \mapsto (\mathcal{R}_\vartheta^{-1}(G|_{T^{C_{r,\vartheta}}}))(\underline{z})$. Transforming the function back to the edge of $T^{C_{r,\vartheta}}$ using $\mathcal{R}_\vartheta$ yields the result $\mathrm{Im}\, G(\underline{x}+i0^{\vartheta})$.

Using the Poisson kernel $\mathcal{P}_{r,\vartheta}$ [Eq. (48)], the Green's function is obtained in the desired wedge $T^{C_{r,\vartheta}}$. The entire procedure is contained in $\mathcal{Q}_{r,\vartheta}$.

2. Feature of $\mathcal{Q}_\vartheta^{(\mathrm{edge})}$: Decoding branch cut geometry from single edge function

The operator $\mathcal{Q}_\vartheta^{(\mathrm{edge})}$ is a map of pure "edge" character. Therefore, it is worthwhile to study it separately. $\mathcal{Q}_\vartheta^{(\mathrm{edge})}$ is well-defined for any square-integrable function $f(\underline{x})$, no matter which orientation ϑ is considered.

Considering an edge function which is compatible with the Green's function properties 1,2,3′ (Sec. III D), $\mathcal{Q}_\vartheta^{(\mathrm{edge})}$ is not defined for the singular orientations (54). For example, a straightforward calculation shows that applying $\mathcal{Q}_\vartheta^{(\mathrm{edge})}$ step by step to $G_0(\underline{x}+i0^{\vartheta=0})$ yields exactly the formula (50), with the switching behavior (52) whose value is undefined for the orientations (54). The missing square-integrability of the edge functions along these directions is the corresponding

mathematical reason. In particular, whenever $\mathcal{Q}_\vartheta^{(\mathrm{edge})}$ crosses a singular orientation of $\mathrm{Im}\, G_0(\underline{x}+i0^{\vartheta=0})$, it exactly generates the jump in $\mathrm{Im}\, G_0(\underline{x}+i0^{\vartheta})$ as a function of ϑ.

Consequently, assuming Eq. (65) is correct, both the holomorphic structure and the complete information about the entire *branch cut structure*, namely the exact geometry of the branch cuts, are encoded in the single edge function $\mathrm{Im}\, G(\underline{x}+i0^0)$. The same is true for the $(\vartheta=0)$-edge limit of the second-order self-energy, $\mathrm{Im}\,\Sigma^{(2)}(\underline{x}+i0^0)$, due to Eq. (60). It is always square-integrable, except for the directions $x_\omega = -3/2x_\varphi$, $x_\omega = -x_\varphi/2$, $x_\omega = x_\varphi/2$, and $x_\omega = 3/2x_\varphi$, namely for the geometry of the second-order branch cuts.

For practical computations, we find that an exploitation of symmetries of $\mathcal{Q}_\vartheta^{(\mathrm{edge})}$ is mandatory. Those are *translational invariance* and *scale invariance*, but *no rotational invariance*: For the translation operator

$$(\mathcal{T}_{\underline{x}'} f)(\underline{x}) := f(\underline{x}-\underline{x}') \tag{75}$$

and for the homogenous scaling operator

$$(\Lambda_\lambda f)(\underline{x}) := \lambda^2 f(\lambda \underline{x}),\ \lambda > 0, \tag{76}$$

we have

$$\left[\mathcal{Q}_\vartheta^{(\mathrm{edge})}, \mathcal{T}_{\underline{x}}\right] = 0, \tag{77}$$

$$\left[\mathcal{Q}_\vartheta^{(\mathrm{edge})}, \Lambda_\lambda\right] = 0, \tag{78}$$

$$\left[\mathcal{Q}_\vartheta^{(\mathrm{edge})}, \mathcal{R}_{\vartheta'}\right] \neq 0. \tag{79}$$

The proof of these commutator relations is provided in Appendix C. Note that because *directional* scaling implies a shear and therefore nonconserved angles in the shapes of $\mathrm{Im}\, G(\underline{x}+i0^0)$, it is no symmetry of the operator, in contrast to uniform scaling.

E. Numerical implementation of $\mathcal{Q}_{r,\vartheta}$

The numerical implementation of the kernel $\mathcal{Q}_{r,\vartheta}$ is nontrivial. Assuming that $G(\underline{x}+i0^0)$ is sufficiently smooth, we can represent it by superimposing localized test functions which span the space of edge functions.

1. Integral structure of the mapping

$\mathcal{Q}_{r,\vartheta}$ introduces a quadruple integral. The first two integrals are the two principal value integrals which come with the Hilbert transforms. The second ones are included by the Poisson kernel $\mathcal{P}_{r,\vartheta}$. The integrations are formally very similar to a sequence of convolutions $A*(B*(C*e))$, where e is an edge function. A crucial point is that, due to the distributional nature of both the principal values and the edge functions, the associativity rule cannot be expected to hold for these convolutions (see Sec 4.2 in Ref. 30): The principal value and our type of edge functions [functions with singular directions, Eqs. (54)] are no distributions with compact support. Therefore, it is impossible to simply contract some "inner integrals" within $\mathcal{Q}_{r,\vartheta}$ analytically in order to obtain a simple kernel function for $\mathcal{Q}_{r,\vartheta}$. The use of a set of test functions which spans the space of edge functions is mandatory.

2. Construction of the test functions

The test functions would preferably be structured in a way which allows the quadruple integral in the operator $\mathcal{Q}_{r,\vartheta}$ to be solved essentially analytically. Using the translation operators $\mathcal{T}_{\underline{X}}$, Eq. (75), and scaling operators $\Lambda_{1/\varepsilon}$, Eq. (76), we define the functions

$$f_{\underline{X},\varepsilon} := \mathcal{T}_{\underline{X}} \Lambda_{1/\varepsilon} f, \tag{80}$$

with

$$f(\underline{x}) := \frac{1}{\pi^2} \prod_{\alpha=\pm 1} \frac{1}{(x_\omega - \alpha x_\varphi/2)^2 + 1}. \tag{81}$$

They turn out to be a good choice as test functions: First, we have the Dirac δ distribution

$$\lim_{\varepsilon\to 0} f_{\underline{X},\varepsilon} = \delta(\underline{x}-\underline{X}) \tag{82}$$

as a limit. Second, due to the symmetries (77) and (78), the use of scaling and translation operators yields—regarding the action of the integrals in $\mathcal{Q}_\vartheta^{(\mathrm{edge})}$—the much more simple expression

$$(\mathcal{Q}_{r,\vartheta} f_{\underline{X},\varepsilon})(\underline{x}) = \left(\mathcal{P}_{r,\vartheta} \mathcal{T}_{\underline{X}} \Lambda_{1/\varepsilon} \left(\mathcal{Q}_\vartheta^{(\mathrm{edge})} f\right)\right)(\underline{x}) \tag{83}$$

rather than $(\mathcal{P}_{r,\vartheta}(\mathcal{Q}_\vartheta^{(\mathrm{edge})} \mathcal{T}_{\underline{X}} \Lambda_{1/\varepsilon} f))(\underline{x})$ as a matrix element of $\mathcal{Q}_{r,\vartheta}$. Third, the simple pole structure of Eq. (81) allows us to compute most of the integrals analytically. Note that the simpler looking symmetric Lorentzian function $\frac{1}{x_\omega^2+x_\varphi^2+1}$ is, in fact, no good alternative to f, because the poles with respect to z_ω or z_φ contain square roots of z_φ or z_ω, respectively. Similar problems arise for localized Gaussians.

The directional arbitrariness $x_\omega \pm x_\varphi/2$ arising in Eq. (81) from choosing a product of 1D Lorentzians in Eq. (81) is still to be discussed. For example, one could also have chosen it to be $x_\omega \pm x_\varphi$, adjusting the normalization factor from $\frac{1}{\pi^2}$ to $\frac{2}{\pi^2}$ in order to assert Eq. (82). A conceptional advantage of our choice of f is, however, that for any domain $T^{C_{r,\vartheta}}$, for which G is holomorphic, we have $r \leqslant 2$. Consequently, due to the pole structure of Eq. (81), f is holomorphic in the domain $T^{C_{r,0}} \subset T^{C_{2,0}}$, whose edge is the starting point of the $\mathcal{Q}_{r,\vartheta}$ transform. Nevertheless, a certain ambiguity remains which could be technically useful.

3. Computation of the matrix elements

We found it feasible to calculate at least the first three integrals of the right-hand side of expression (83) analytically, using a computer algebra system. In order to compute the fourth integral, an adaptive numerical quadrature can be used.

The result of the analytical integration of the first two integrals, namely $(-\mathcal{Q}_\vartheta^{(\mathrm{edge})} f)(\underline{x})$, is shown in Fig. 18 for selected edge orientations. We find that $(-\mathcal{Q}_\vartheta^{(\mathrm{edge})} f)(\underline{x})$ is a rational function which changes continuously as a function of ϑ, in contrast to the transformation behavior of $\mathrm{Im}\, G_0(\underline{x}+i0^0)$. Note that since $\mathcal{Q}_\vartheta^{(\mathrm{edge})}$ is scale-invariant Eq. (78), the transformation behavior of the Dirac δ distribution is analogous to that in Fig. 18. Consequently, the transformed δ distribution on the edge $\mathbb{R}+i0^\vartheta$ is not a function but rather a distribution with a relatively complicated structure. Therefore, the limit $\delta \to 0$ in Eq. (83) cannot be taken before the last two integrals from the Poisson kernel $\mathcal{P}_{r,\vartheta}$ are computed.

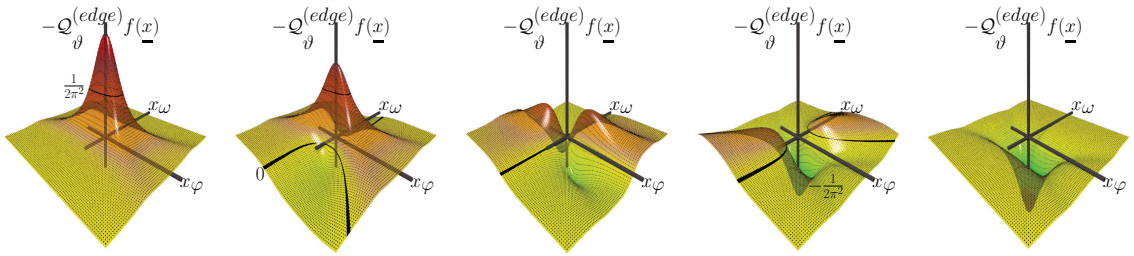

(a) $\vartheta = 0$ (b) $\vartheta = \pi/4$ (c) $\vartheta = \pi/2$ (d) $\vartheta = 3\pi/4$ (e) $\vartheta = \pi$

FIG. 18. (Color online) Transformation behavior of the test function $f(\underline{x})$ as a function of the edge-to-edge map $-\mathcal{Q}_\vartheta^{(\mathrm{edge})}$ for different values of ϑ. Function values are shown within the range $[-5,5] \times [-5,5]$. Due to translational and scale invariance, it represents the edge-to-edge transformation behavior of a Dirac δ function under the continuity assumption (65).

In the special case $\vartheta = \pi/2$, Fig. 18(c), the asymptotic behavior of the result decays $\propto \frac{1}{|\underline{x}|}$ when $\underline{x} \to \infty$, in contrast to the original test function behavior $f(\underline{x}) \propto \frac{1}{|\underline{x}|^2}$. This is because the Hilbert transforms are taken with respect to mutually orthogonal directions in $\mathbb{R}^2$, here.

The angles between 0 and $\pi/2$ interpolate smoothly between the extremal cases of the unperturbed well-localized $f(\underline{x})$ at $\vartheta = 0$ and the long-range function at $\vartheta = \pi/2$. The solution at $\vartheta = \pi$ is again strongly localized and equals $-f(\underline{x})$. The behavior in the interval $[\pi, 2\pi)$ is analogous due to symmetry reasons.

4. Implementation

As mentioned above, the third integral of the operator sequence (83) can still be computed analytically. However, each integration of the sequence adds additional poles to the resulting function, and more and more complex distinguishments have to be done in order to decide whether a pole is on the upper or the lower half plane and whether it contributes or not to certain residue sums.

Because translational and scale invariance do not seem to be as useful concepts as applied to $\mathcal{P}_{r,\vartheta}$, not only the extra variable r appears in the computation of the remaining expressions, but also the shift $\underline{X}$ and the scale λ of the test function (80). For the third integral, one can still determine the poles and residues before doing the latter substitution with the computer algebra system, however.

At present, very lengthy expressions result for the last integrand. As a consequence, the last integral was evaluated numerically for each matrix element. The limit $\delta \to 0$ can only be taken numerically. An algebraic determination of the poles of this expression is cumbersome, because high-order polynomials appear in the denominator of the resulting expressions. Nevertheless, numerical computations indicate that the limit $\delta \to 0$ yields well-defined functions after the fourth integration. Once an algebraic expression is found, the expression for the limit $\delta \to 0$ would be more simple than the intermediate terms. As already stated in the beginning of this section, we compute the fourth integral with an adaptive numerical integration routine in practice. In the numerical MaxEnt implementation, one can adjust δ as a function of $\underline{x}$, denoted by $\delta_{\underline{x}}$, depending on how well a specific region of the edge should be resolved.

When defined according to the interacting branch cut geometry, $\mathcal{Q}_{r,\vartheta}$ is simply called $\mathcal{Q}$ in the following. Details on the numerical representation of $\mathcal{Q}$ are provided in Appendix D. A detailed description of implementation and setup of the MaxEnt method using $\mathcal{Q}$ is given in Appendix E.

5. Details of the MaxEnt procedure

The quality of the results of the MaxEnt method using the $\mathcal{Q}$ mapping critically relies on a careful *a posteriori* identification of the high-energy structure of the physical edge function $\tilde{A}(x_\varphi, x_\omega)$ along its singular directions. The information is incorporated into the default model as described in Appendix E. In brief, we first determine the most probable lateral width of the default model (E3). In the same fashion, a second step optimizes the low-energy structure of the default model, by *a posteriori* determining the most probable low-energy bandwidth, i.e., the quantity $\tilde{\sigma}_{\mathrm{def}}$ in Eq. (E4) with the highest posterior probability. In Eq. (E4) we set the low-energy scale to $R = 5\Gamma$. In tested examples, no strong dependence of the inferred results on R was observed. In future applications, however, in order to increase accuracy, it may be advantageous to also perform an optimization with respect to the posterior probability of R.

Let us provide an example of how the method works for the weak-coupling case, i.e., for parameters $U = 2\Gamma$, $\beta = 5\Gamma^{-1}, e\Phi = \Gamma$. The final results for the spectral function were already presented in Fig. 3. It turns out that the applicability of the $\mathcal{Q}$ approach is limited *a posteriori* by bad behavior of the inferred spectral functions to input data with $\omega_n > |\varphi_m/2|$ for $n \geqslant 0$. This condition corresponds to not crossing the principal branch cut $\gamma = \pm 1$ in Fig. 13(b), when coming from the retarded Green's function (edge orientation $\vartheta = 0$). Apart from this restriction, there appears to be no further problem with the approach. Consequently, at least for weak coupling, the central continuity assumption of the $\mathcal{Q}$ approach is practically solely violated with respect to the branch cuts $\gamma = \pm 1$. The violation already occurs at very small values of the many-body interaction, $U \leqslant 2\Gamma$. However, it vanishes at $U = 0$, since the continuity assumption is exact for G_0. This observation is compatible with the observed strong violation of the assumption within the Dyson series which was reported in Sec. IV B.

We therefore can use all Matsubara data of our Monte Carlo simulation subject to $\omega_n > |\varphi_m/2|$. For the inverse temperature

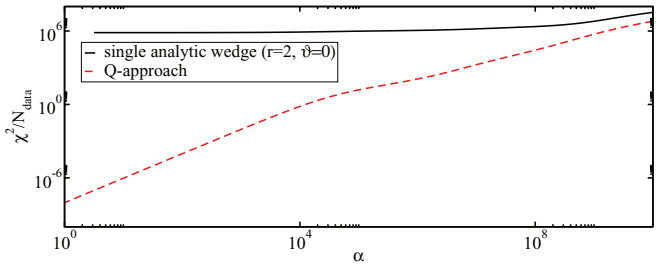

FIG. 19. (Color online) Comparison of χ^2 as a function of the MaxEnt regularization parameter for single-wedge kernel $\mathcal{P}_{r,\vartheta}$ and multiwedge kernel $\mathcal{Q}$ at weak interaction $U = 2\Gamma, \beta = 5\Gamma^{-1}$, and $e\Phi = \Gamma$ as a function of the regularization parameter α. For the same input set, the single-wedge approach clearly fails to converge due to the presence of higher-order branch cuts.

$\beta = 5\Gamma^{-1}$, these extend from $n = 1$ to $n = 8$ for ω_n with $m = \pm 1, \ldots, \pm 5$ for φ_m. As a first test, we show in Fig. 19 the performance of the MaxEnt method for both the single-wedge[4] and the multiple-wedge approaches for the given data set. Because data from the comparably widely opened wedge $\omega_n > |\varphi_m/2|$ are used in the single-wedge approach, it implicitly assumes the interacting Green's function to be analytic for $\mathrm{Im}\, z_\omega > |\mathrm{Im}\, z_\varphi/2|$. Apparently, this wrong assumption makes it impossible to obtain a reasonable fit with a positive definite $\tilde{A}(\underline{x})$. Consequently, the χ^2 value of the procedure does not drop below $10^6 N_{\mathrm{data}}$, and the MaxEnt fails to converge. In sharp contrast, values of $\chi^2/N_{\mathrm{data}} \approx 1$ may be reached with the MaxEnt with respect to $\mathcal{Q}$. Also, controls such as the MaxEnt error rescaling merit do not indicate the presence of any abnormalities.

Thus, for the $\mathcal{Q}$ mapping, a well-behaved MaxEnt solution is obtained. As further discussed in Appendix E, the quality of the solution very much relies on appropriately including the prior knowledge on singular directions of the Green's functions in $\mathbb{C}^2$ into the default model of the edge function. For this purpose, within a set of smooth default models with the correct singular directions as $\underline{x} \to \infty$, a most probable one is identified within the Bayesian framework of the MaxEnt method. The thus identified default model for the edge function is displayed in Fig. 20(a). Using this default model, the well-behaved edge function $\tilde{A}(x_\varphi, x_\omega)$ shown in Fig. 20(b) is obtained. An overall moderate sharpening of the edge function along the crosslike structure is observed as a result of this final step of the Bayesian inference procedure.

With such appropriately optimized default models, the results presented in Sec. II were obtained from weak to intermediate coupling strengths. Throughout, the only major data range constraint, $\omega_n > |\varphi_m/2|$ was found, which prohibits crossing the principal branch cut due to violations of the continuity assumption. On occasion, for stronger correlation strengths, values with small ω_n had to be discarded in order to obtain a converging MaxEnt solution, i.e., a solution which meets the continuity assumption constraints. At the comparably small inverse temperature $\beta = 5\Gamma^{-1}$ used, calculations require only moderate computer resources, mainly due to the comparably small QMC data space of approximately 50 imaginary-time-theory data points. In general, the amount of data will grow quadratically as a function of inverse temperature, due to the simultaneous presence of Matsubara voltage and Matsubara frequency. Additionally, at low temperatures, sharp features in the spectral function and hence the edge function $\tilde{A}$ will have to be resolved, requiring an enhanced grid refinement. Altogether, matrix sizes in the MaxEnt will increase substantially when the temperature is decreased. In particular, the computational effort for the generation of an appropriate kernel matrix (cf. Appendix D) grows dramatically and the memory consumption of the MaxEnt itself poses a limitation at lower temperatures at the present stage of code development. Additionally, it is well known that the resolution of low-temperature features with the MaxEnt method requires a careful Bayesian analysis based on higher-temperature data, i.e., an "annealing procedure," involving a sequence of QMC plus MaxEnt runs for a reasonably fine temperature grid.[5,13]

V. PERSPECTIVE: UNBIASED MULTIWEDGE APPROACH

From a mathematical point of view, the underlying continuity assumption of the multiwedge approach, i.e., the mapping $\mathcal{Q}$, is only approximate, because in higher orders of perturbation theory, terms which do not characterize the full collection of wedges, but rather just isolated wedges or subcollections of wedges, are generated. These terms are manifested in discontinuities of the real part of the Green's function at the branch point $\mathrm{Im}\, \underline{z} = 0$.

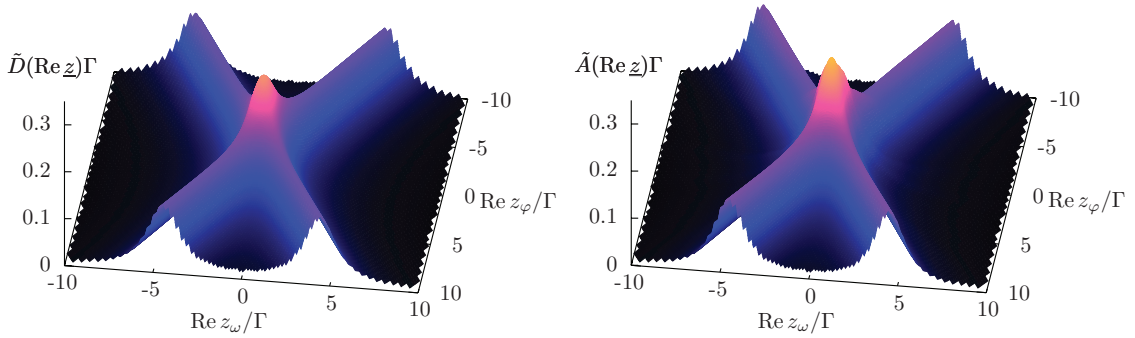

(a) a-posteriori identified best default model (b) inferred $\tilde{A}(\underline{x})$

FIG. 20. (Color online) Application of the MaxEnt procedure for the $\mathcal{Q}$ mapping to the nonequilibrium weak-coupling case $U = 2\Gamma$, $\beta = 5\Gamma^{-1}, e\Phi = \Gamma$, with CT-QMC data as input. The default model has been identified via its maximal posterior probability.

In order to extend the $\mathcal{Q}$ approach to the full nonequilibrium Kondo regime $U \geqslant 2\pi\Gamma$, $e\Phi \sim T_K$, $\beta^{-1} \sim T_K$, one has to take these contributions into account. This requires the consideration of the full analytic structure of the theory, i.e., the full set of edge functions.

As a consequence, extra terms have to be added to the representation of $G(z_\varphi, z_\omega)$ within the MaxEnt procedure. Obvious candidates for such degrees of freedom are the residual imaginary parts of edge functions

$$\tilde{R}_n(\underline{x}) := \operatorname{Im} G(\underline{x} + i0^{\vartheta_n}) - \pi \left(\mathcal{Q}^{(\text{edge})}_{\vartheta_n} \tilde{A}\right)(\underline{x}), \tag{84}$$

for the edge of the nth wedge with orientation ϑ_n. Because the $\mathcal{Q}$ mapping is exact at high energies $\|\underline{x}\|$, the terms $\tilde{R}_n(\underline{x})$ are essentially localized within a finite radius around 0. This range is expected to be of the order of magnitude of the energy scales Γ, U, ϵ_d, and $e\Phi$.

Regarding the inverse problem, for data in the nth wedge, one has the *exact* representation

$$\operatorname{Im} G(i\varphi_m, i\omega_n) = (\mathcal{P}_{r_n,\vartheta_n} \tilde{R}_n)(i\varphi_m, i\omega_n) + \pi(\mathcal{Q}\tilde{A})(i\varphi_m, i\omega_n), \tag{85}$$

where r_n is the opening ratio of the respective data wedge.[31] The MaxEnt procedure must determine $\tilde{R}_n$ and $\tilde{A}$ simultaneously. Practically, the terms $\tilde{R}_n$ would act as "valves" for the conceptual imperfection of the $\mathcal{Q}$ mapping within the Bayesian information flow.

It is an interesting question if the formally infinitely many 2D variable vectors in practice lead to a dramatic increase in the fit space or not. Due to locality of the terms $\tilde{R}_n(\underline{x})$, the effort is probably less than for the $\tilde{A}$ function, which itself encodes many aspects of the analytic structure. Furthermore, the rather large Poisson kernel matrix elements at low energies will possibly lead to a comparably good MaxEnt performance in the determination of $\tilde{R}_n(\underline{x})$, as long the opening ratio ϑ_n of the nth wedge is comparably large.

Because the functions $\tilde{R}_n(\underline{x})$ cannot be expected to be positive, it is necessary to introduce a shift to a positive function, such as for the spectral functions of the static observables in paper I. The terms $\tilde{R}_n(\underline{x})$ are presumably most dominant for wedges next to the noninteracting Green's function's branch cuts. A very careful Bayesian analysis, including an appropriate set of choosable default models constructed from *a priori* information, is probably required for a successful application of the exact approach (85). It is also possible that the perturbative structure of the theory reorganizes terms $\tilde{R}_n$ in subcollections of wedges which result in a more moderate MaxEnt problem than Eq. (85). In particular, the branch cut at $\operatorname{Im} z_\varphi = 0$ probably leads to a nonzero limit $\lim_{n\to\infty} \tilde{R}_n$, where the limit $n \to \infty$ shall consider a sequence of wedges with $\vartheta_{n\to\infty} = 0$ or $\vartheta_{n\to\infty} = \pi$.

VI. SUMMARY

We systematically studied the mathematical structure of the dot-level Green's function and the Bayesian inference of nonequilibrium spectral functions and transport properties from effective-equilibrium quantum Monte Carlo data within the Matsubara-voltage theory. Furthermore, a continuity assumption on the analytic structure was introduced which strongly improved the numerics of the MaxEnt approach of an earlier publication.[4]

Formal parts of the paper introduced the essential concepts of the function theory of several complex variables and connected to the respective mathematical literature. Using insights from perturbation theory, the Green's function was characterized axiomatically with regard to its function-theoretical structure. As the fundamental domains of holomorphy, so-called wedges (tubular cones) emerged. The Green's function is composed of sheets which are holomorphic on the wedges enclosed by branch cuts. Within each wedge, the Matsubara data of the Green's function uniquely map to a real-time limit on the so-called edge of the wedge. For this purpose, an explicit integral representation was constructed. However, depending on the considered wedge, the edge structure does not necessarily have a direct physical interpretation.

In an earlier publication,[4] we had been unable to compute reliable *nonequilibrium* spectral functions from a MaxEnt procedure based on integral representations within wedges, due to rather strong assumptions on the analytic structure and weak assumptions on the physical structure. The assumptions had limited us to a single wedge with a rather small opening ratio, on which the Green's function is not strictly analytic but which directly includes the physical limit procedure on its edge. While as compared to the present work the numerical effort of the MaxEnt procedure was rather low, due to the wedge structure and simple kernel structure, we had not been able to consider most available quantum Monte Carlo data within the MaxEnt procedure. The hereby implied loss of information from available simulation data had not affected the equilibrium spectra but the nonequilibrium spectra, due to the kernel structure.

In order to overcome these previous limitations, we introduced a continuity assumption to the real-time structure of the Green's function, i.e., its structure at the branch point around which the edges of the wedges associated to the branches of the Green's function are aligned. The assumption includes structures generated by the earlier fit approach introduced in Ref. 1, which was motivated by perturbation theory. Mathematically, the assumption led to a uniform description of data from all branches of the Green's function and gave rise to a linear operator $\mathcal{Q}$ which, while hard to implement, enhanced the MaxEnt procedure to a larger set of quantum Monte Carlo data.

We found that the continuity assumption appears to be valid for a very broad range of data, up to intermediate coupling strengths, eventually yielding reasonable nonequilibrium MaxEnt results for spectral function and transport properties, which are dramatically improved as compared to the results of Ref. 4. However, as the nonequilibrium Kondo regime is approached, we expect the continuity assumption to break down eventually. For this parameter regime, the method could be extended along the line discussed in Sec. V.

ACKNOWLEDGMENTS

The authors acknowledge useful discussions with J. Freericks, F. B. Anders, S. Schmitt, K. Schönhammer, and A. Schiller. A.D. acknowlegdes financial support by the DAAD through the PPP exchange program. J.H. acknowledges

the National Science Foundation with the Grant No. DMR-0907150. M.J. acknowledges NSF LA-SiGMA Cooperative Agreement EPS-100389. A.D. and T.P. would also like to acknowledge computer support by the HLRN, the GWDG, and the GOEGRID initiative of the University of Göttingen. Parts of the implementation are based on the ALPS 1.3 library.[32]

APPENDIX A: UNIQUENESS OF THE ANALYTIC CONTINUATION OF DYNAMICAL QUANTITIES

In the following, we would like to show that the continuation of Matsubara data $G(i\varphi_m, i\omega_n)$ to the multisheeted holomorphic function $G(\underline{z})$ is unique; i.e., we prove assumption 3 in Sec. III D, relation (13). We derive the uniqueness using the axiomatic statements 1, 2, and 3′ of Sec. III D. Since the proof involves some elementary geometry, it is accompanied by several sketches.

We may focus our attention to a single-wedge T^C which is defined by subsequent branch cuts from Eqs. (11). The data $G(i\varphi_m, i\omega_n)$ which are located in the wedge are our starting point, $(\varphi_m, \omega_n)^T \in C$. Without loss of generality we can assume that we have entire lines of data, $G(i\varphi_m, i\omega_I)$, $\omega_I \in \mathbb{R}$, because arbitrary continuous imaginary ω_I may be computed by Fourier transform in the φ_mth effective equilibrium theory, having again $(\varphi_m, \omega_I)^T \in C$. Let us denote the effective equilibrium data range by

$$E_0 := \{i(\varphi_m, \omega_I)^T | m \in \mathbb{Z}, \omega_I \in \mathbb{R}\} \cap T^C. \tag{A1}$$

These lines of known data of the unknown function $G(\underline{z})$ in the wedge T^C are depicted in Fig. 21. They constitute 1D lines in the 4D wedge T^C for which the function $G|_{T^C}$ shall be reconstructed.

We prove, step by step, the uniqueness of the continuation of the imaginary-time data by applying biholomorphic maps and the identity theorem of complex analysis. The central idea is to extend larger and larger subsets for which a unique continuation is obtained.

1. Reconstruction of edge values using complex lines which are isomorphic to $\mathbb{H}$

Due to assumptions 1 and 2, we found that the Green's function $G|_{T^C}$ may be reconstructed from their edge values, using Eqs. (39) and (40). Therefore, it suffices to show that we can reconstruct all edge values of the function G from the data $G|_{E_0}$.

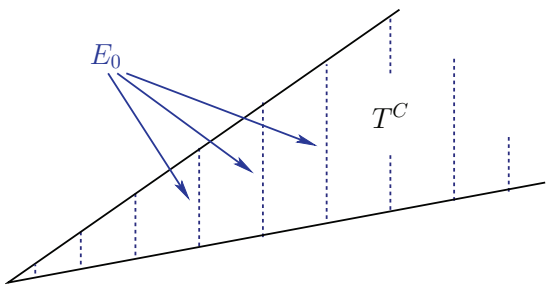

FIG. 21. (Color online) The wedge to be considered. The dash-dotted lines denote the data yielded by imaginary-time theory.

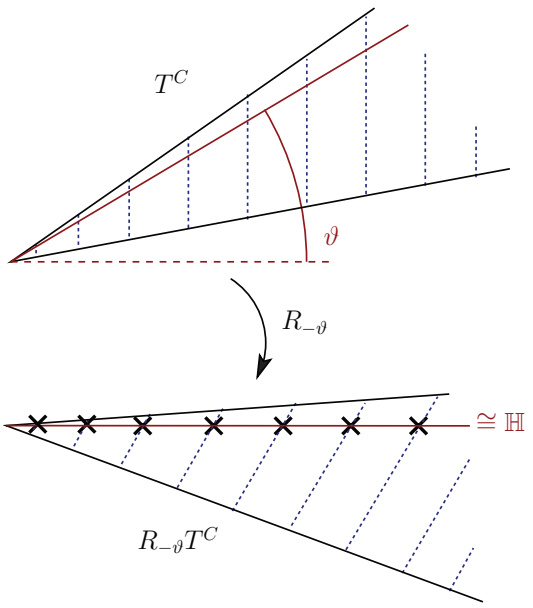

FIG. 22. (Color online) A single line contained by the cone C may after biholomorphic rotation $R_{-\vartheta}$ and subsequent complexification be interpreted as the upper half plane $\mathbb{H}$ of $\mathbb{C}$.

We first show that one may reconstruct a certain set of *single lines through zero* on the edge. Each of these lines is defined by an angle ϑ. All function values on the line may be reconstructed if the angle ϑ is contained by the cone C.

The proof of the latter statement is the following. Consider a single line in the cone C, given by the angle ϑ. A biholomorphic rotation in the sense of Sec. III E2 can then be applied in such a way that the line is horizontal and may, after complexification, be interpreted as the upper half plane $\mathbb{H}$ of $\mathbb{C}$; see Fig. 22. The real line is then associated to a horizontal line on the edge of $R_{-\vartheta}T^C$.

The biholomorphic equivalent to the yet-unknown function is now $\tilde{G}(\underline{z}) = G(R_{-\vartheta}^{-1}\underline{z})$. Note that the line $(0, i\lambda)^T$ in $R_{-\vartheta}T^C$, $\lambda > 0$, contains infinitely many known values of $\tilde{G}(\underline{z})$. These are denoted by the crosses in Fig. 22. Extending to the upper half plane $(0, \mathbb{H})$, one may apply the identity theorem of complex analysis for reconstructing $\tilde{G}(\underline{z})$ on the whole plane $(0, \mathbb{H})$. In particular, the boundary values $\tilde{G}(0, \mathbb{R} + i0^+)$ are recovered. This proves the statement of this section.

(a) Identity theorem

Let us comment on the satisfaction of the assumptions of the identity theorem. Since $(0, \infty)$ is the accumulation point of the known data points on $(0, \mathbb{H})$, i.e., of the "series of crosses in Fig. 22," given by $(0, \mathbb{H}) \cap R_{-\vartheta}E_0$, we have to show that $\tilde{G}(0, 1/z)$ may be extended to an analytic function at $z = 0$. Once this is possible, the function is uniquely determined by the set of function values.

Combining assumptions 1 and 3′, we know that $G(\zeta \underline{x}^{(0)})$ (in the sense of assumption 3′) behaves like a conventional Green's function, because the singular case coincides with a branch cut which is by construction not contained by the wedge. Due to this rapid decay one may extend $\tilde{G}$ to the lower half plane such that $\tilde{G}(0, z^*) = \tilde{G}(0, z)^*$ and is holomorphic at $z = \infty$. This can be done explicitly using a spectral representation with respect

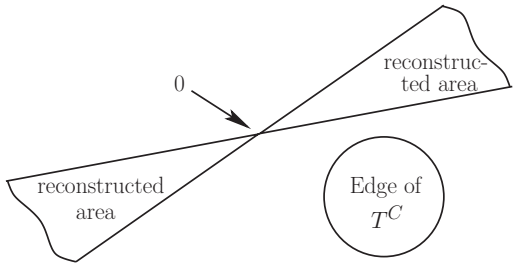

FIG. 23. Uniquely reconstructed range $\mathrm{Edge}^{(\mathrm{recon},0)}_{T^C}$ of $G(\underline{z})|_{T^C}$ on the edge of T^C following from the partial argument of Appendix A1. The wiggly lines in the boundary mean that the area extends to infinity.

to the boundary values of $\mathrm{Im}\,\tilde{G}(0,z)$ on the real axis. The spectral representation exists due to the $1/z$ asymptotics which lets the line integral contribution vanish on the infinitely large semicircle attached to the real axis. Note that this construction is also compatible with the symmetry relation $G(-i\varphi_m, -i\omega_n) = G(i\varphi_m, i\omega_n)^*$.

As a consequence, the identity theorem is applicable for $\tilde{G}(0,z)$ at $z = \infty$ such as it is for regular Matsubara Green's functions.

One may also think of $G(\zeta \underline{x}^{(0)})$, $\zeta \in \mathbb{H}$ as a meromorphic function of $\zeta \in \mathbb{C}$, because it may, due to boundedness and $1/\zeta$ asymptotics, be approximated arbitrarily well by a meromorphic function, such as in an infinite Padé expansion. Since meromorphic functions on $\mathbb{C}$ are holomorphic on the Riemann sphere, the identity theorem holds at the accumulation point ∞.

(b) Resulting reconstruction of edge values

Sweeping through all possible angles ϑ which are contained by the cone C, the uniquely reconstructed edge behavior of $G|_{T^C}$ is given by the area depicted in Fig. 23.

It is obviously given by

$$\mathrm{Edge}^{(\mathrm{recon},0)}_{T^C} := C \cup (-C). \tag{A2}$$

2. Extending the unique range to the entire edge

In order to show that the function values of $G|_{T^C}$ are also uniquely defined by $G|_{E_0}$ for the complement of $\mathrm{Edge}^{(\mathrm{recon},0)}_{T^C}$, the argument has to be extended in a similar way. The trick is to consider yet another set of $\mathbb{H}$-isomorphic subspaces and then apply the argument of the last section to a larger set of data.

(a) Extending the known data range within the wedge

The first step is depicted in Fig. 24. In contrast to before, we consider a constant angle ϑ_0 and various lines which start at different points on the boundary of the cone with the orientation ϑ_0.

After biholomorphic rotation to the wedge $R_{-\vartheta_0} T^C$ we can again complexify the lines

$$\tilde{l}_{\underline{\tilde{y}}^{(0)}} := \{i\underline{\tilde{y}}^{(0)} + i(0,\lambda)^T, \lambda > 0\};\ \underline{\tilde{y}}^{(0)} \in \partial C \tag{A3}$$

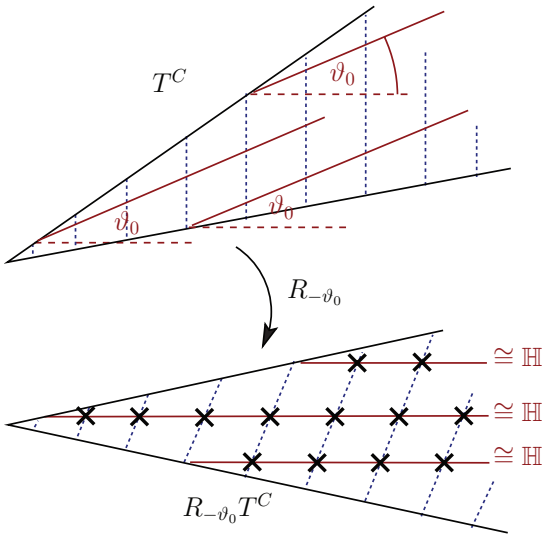

FIG. 24. (Color online) Enhancing the formal holomorphic reconstruction within the wedge.

to

$$\tilde{L}_{\underline{\tilde{y}}^{(0)}} := i\underline{\tilde{y}}^{(0)} + \begin{pmatrix} 0 \\ \mathbb{H} \end{pmatrix}. \tag{A4}$$

The isomorphy of $\tilde{L}_{\underline{\tilde{y}}^{(0)}}$ to $\mathbb{H}$ and assumption 3′ again enable us to apply the identity theorem to the crossed data in Fig. 24, namely to the infinite sequence $(G \circ R_\vartheta)|_{(R_{-\vartheta} E_0) \cap \tilde{L}_{\underline{\tilde{y}}^{(0)}}}$.

By this, the transformed Green's function $\tilde{G} = G \circ R_{\vartheta_0}$ is reconstructed for all points of the set,

$$D := \bigcup_{\underline{\tilde{y}}^{(0)} \in \partial C} \tilde{L}_{\underline{\tilde{y}}^{(0)}} = (R_{-\vartheta_0} T^C) \cap \begin{pmatrix} i\mathbb{R} \\ \mathbb{C} \end{pmatrix}. \tag{A5}$$

For simplicity, we may now just look at a subset of D, namely,

$$\tilde{E}_1 := R_{-\vartheta_0} E_0 + \begin{pmatrix} 0 \\ \mathbb{R} \end{pmatrix}. \tag{A6}$$

It enables us to see that the values of G are now known on the set

$$E_1 := E_0 + R_{\vartheta_0} \begin{pmatrix} 0 \\ \mathbb{R} \end{pmatrix}. \tag{A7}$$

(b) Full reconstruction of the edge

With the information from E_1 one may reinterpret the procedure associated with Fig. 22 and described in Appendix A 1. The dashed lines of known data now contain an *additional real dimension* along the direction $R_{\vartheta_0}(0,1)^T$.

We can use each point $\lambda R_{\vartheta_0}(0,1)^T$ ($\lambda \in \mathbb{R}$) of this new degree of freedom as an offset of the lines used in Appendix A 1 and reapply the entire procedure. Using the resulting affine subspaces, the Green's function may be reconstructed on further regions of the edge which are affine to the one in Fig. 23, namely,

$$\mathrm{Edge}^{(\mathrm{recon},\lambda)}_{T^C} := \mathrm{Edge}^{(\mathrm{recon},0)}_{T^C} + \lambda R_{\vartheta_0}(0,1)^T. \tag{A8}$$

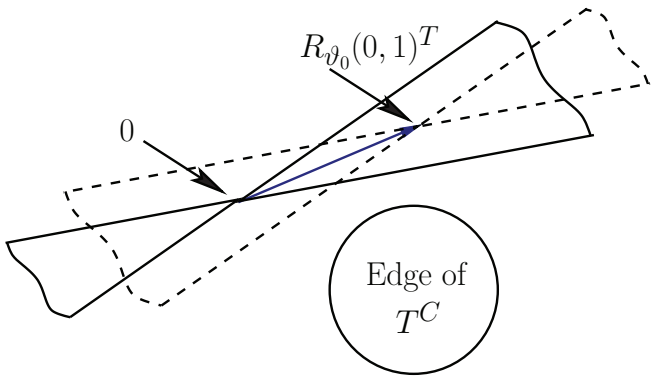

FIG. 25. (Color online) Reconstructing the Green's function on the complete edge. The reconstructed area $\mathrm{Edge}_{T^C}^{(\mathrm{recon},0)}$ [see Fig. 23 and Eq. (A2)] may be extended by affine transformations along the $R_{\vartheta_0}(0,1)^T$ direction using the information from the set E_1.

Applying the argument to all $\lambda \in \mathbb{R}$ reconstructs the entire edge and hence the entire Green's function $G|_{T^C}$, because $\bigcup_{\lambda\in\mathbb{R}} \mathrm{Edge}_{T^C}^{(\mathrm{recon},\lambda)} = \mathrm{Edge}_{T^C}$.

This "affine procedure" is sketched in Fig. 25.

APPENDIX B: EMPIRICAL PROPERTIES OF THE RESIDUAL TERM

The empirical observation that the quantum Monte Carlo data are continuous as a function of $i\omega_n$, as one crosses higher-order branch cuts, yields the following structure. Let ϑ_0 be the orientation of the corresponding branch cut. Then, due to the observed continuity, we have

$$\begin{aligned} &G(i\rho\sin(\vartheta_0-\delta), i\rho\cos(\vartheta_0-\delta)) \\ &\quad = G(i\rho\sin(\vartheta_0+\delta), i\rho\cos(\vartheta_0+\delta)), \end{aligned} \tag{B1}$$

for any $\rho > 0$.

Using the identity theorem along the directions $\vartheta_0 \pm \delta$, one find that the relation

$$R^{(\vartheta_0-\delta,\vartheta_0+\delta)}(\rho\sin(\vartheta_0), \rho\cos(\vartheta_0)) = 0 \tag{B2}$$

holds for any $\rho > 0$. Consequently, the continuity in Matsubara space induces a continuity relation in the edge space. Similarly, one could construct relations for the derivatives of G which help constrain $R^{(\vartheta,\vartheta')}(\underline{x})$.

APPENDIX C: COMMUTATOR RELATIONS OF $\mathcal{Q}_\vartheta^{(\mathrm{edge})}$

We derive the commutator relations (77), (78), and (79).

1. Translational invariance

Let us consider the action of $\mathcal{Q}_\vartheta^{(\mathrm{edge})} = \mathcal{R}_\vartheta \mathcal{H} \mathcal{R}_\vartheta^{-1} \mathcal{H}$ on a function $\tilde{A}(x,y)$ which is translated by the operator $\mathcal{T}_{\underline{X}}$, where we set $\underline{X} = (X,Y)^T$. We also write $\underline{x} := (x,y)^T$.

As a first step, we apply the Hilbert transform,

$$\begin{aligned} (\mathcal{H}\mathcal{T}_{\underline{X}}\tilde{A})(\underline{x}) &= \frac{1}{\pi}\fint d\tilde{y}\, \frac{\tilde{A}(x-X,\tilde{y}-Y)}{y-\tilde{y}} \\ &= \frac{1}{\pi}\fint d\tilde{y}\, \frac{\tilde{A}(x-X,\tilde{y})}{(y-Y)-\tilde{y}}. \end{aligned} \tag{C1}$$

Using the short-hand notation $c := \cos\vartheta$, $s := \sin\vartheta$, we then have

$$(\mathcal{R}_\vartheta^{-1}\mathcal{H}\mathcal{T}_{\underline{X}}\tilde{A})(\underline{x}) = \frac{1}{\pi}\fint d\tilde{y}\, \frac{\tilde{A}(cx+sy-X,\tilde{y})}{(-sx+cy-Y)-\tilde{y}}. \tag{C2}$$

In the next two steps one obtains

$$\begin{aligned} (\mathcal{Q}_\vartheta^{(\mathrm{edge})}\mathcal{T}_{\underline{X}}\tilde{A})(\underline{x}) = \frac{1}{\pi^2}\fint d\tilde{y}\, \underbrace{\frac{1}{sx+cy-\tilde{\tilde{y}}}}_{\to(C5)}\fint d\tilde{y} \\ \times \frac{\tilde{A}(\overbrace{(cx-sy)c+s\tilde{\tilde{y}}-X}^{\to(C6)}, \tilde{y})}{\underbrace{-(cx-sy)s+c\tilde{\tilde{y}}-Y}_{\to(C7)}-\tilde{y}}. \end{aligned} \tag{C3}$$

By substituting $\underline{X} = 0$ and then applying $\mathcal{T}_{\underline{X}}$ from the left, one finds

$$\begin{aligned} (\mathcal{T}_{\underline{X}}\mathcal{Q}_\vartheta^{(\mathrm{edge})}\tilde{A})(\underline{x}) = \frac{1}{\pi^2}\fint d\tilde{\tilde{y}}\, \frac{1}{s(x-X)+c(y-Y)-\tilde{\tilde{y}}}\fint d\tilde{y} \\ \times \frac{\tilde{A}([c(x-X)-s(y-Y)]c+s\tilde{\tilde{y}}, \tilde{y})}{-(c(x-X)-s(y-Y))s+c\tilde{\tilde{y}}-\tilde{y}}. \end{aligned} \tag{C4}$$

In order to verify that the expressions (C3) and (C4) are, in fact, equal, we consider the following system of linear equations:

$$sx+cy-\tilde{\tilde{y}} = sx_0+cy_0-y^*, \tag{C5}$$

$$(cx-sy)c+s\tilde{\tilde{y}}-X = (cx_0-sy_0)c+sy^*, \tag{C6}$$

$$-(cx-sy)s+c\tilde{\tilde{y}}-Y = -(cx_0-sy_0)s+y^*c, \tag{C7}$$

in matrix form:

$$\begin{aligned} \underbrace{\begin{pmatrix} -1 & s & c \\ s & c^2 & -sc \\ c & -sc & s^2 \end{pmatrix}}_{=:M} \cdot \begin{pmatrix} \tilde{\tilde{y}} \\ x \\ y \end{pmatrix} - \begin{pmatrix} 0 \\ X \\ Y \end{pmatrix} \\ = \underbrace{\begin{pmatrix} -1 & s & c \\ s & c^2 & -sc \\ c & -sc & s^2 \end{pmatrix}}_{=:M} \cdot \begin{pmatrix} y^* \\ x_0 \\ y_0 \end{pmatrix}. \end{aligned} \tag{C8}$$

The equations correspond to the idea of substituting the terms in Eq. (C3) as denoted there in such a way that y^* is the new integration variable, $\int d\tilde{\tilde{y}} \to \kappa \int dy^*$, where κ is some regular prefactor from the integral transformation, and such that the external variables x and y are replaced with x_0 and y_0. We will see that the resulting form will exactly be Eq. (C4).

The system (C5)–(C7) can be solved by inversion of the matrix M: One has

$$M^{-1} = \begin{pmatrix} 0 & s & c \\ s & 1 & 0 \\ c & 0 & 1 \end{pmatrix}, \tag{C9}$$

det $M = -1$, and consequently the well-defined solution

$$y^* = \tilde{\tilde{y}} - (sX + cY), \tag{C10}$$

$$x_0 = x - X, \tag{C11}$$

$$y_0 = y - Y. \tag{C12}$$

The integral transformation constant $\kappa = 1$, and performing the substitutions (C5)–(C7) in Eq. (C3) yields Eq. (C4), when y^* is again renamed $\tilde{\tilde{y}}$.

Therefore, $[\mathcal{Q}_\vartheta^{(\mathrm{edge})}, \mathcal{T}_{\underline{X}}] = 0$.

2. Scale invariance

Similarly, we show the scale invariance (78). We have

$$\begin{aligned}\big(\mathcal{Q}_\vartheta^{(\mathrm{edge})}\Lambda_\lambda \tilde{A}\big)(\underline{x}) &= \frac{\lambda^2}{\pi^2}\fint d\tilde{\tilde{y}}\,\frac{1}{sx + cy - \tilde{\tilde{y}}} \\ &\quad\times \fint d\tilde{y}\,\frac{\tilde{A}(\lambda[(cx - sy)c + s\tilde{\tilde{y}}],\lambda\tilde{y})}{-(cx - sy)s + c\tilde{\tilde{y}} - \tilde{y}} \qquad \text{(C13)}\\ &= \frac{1}{\pi^2}\fint d\tilde{\tilde{y}}\,\frac{1}{sx + cy - \tilde{\tilde{y}}/\lambda} \\ &\quad\times \fint d\tilde{y}\,\frac{\tilde{A}((c\lambda x - s\lambda y)c + s\tilde{\tilde{y}},\tilde{y})}{-(cx - sy)s + c\tilde{\tilde{y}}/\lambda - \tilde{y}/\lambda} \qquad \text{(C14)}\\ &= \frac{\lambda^2}{\pi^2}\fint d\tilde{\tilde{y}}\,\frac{1}{s\lambda x + c\lambda y - \tilde{\tilde{y}}} \\ &\quad\times \fint d\tilde{y}\,\frac{\tilde{A}((c\lambda x - s\lambda y)c + s\tilde{\tilde{y}},\tilde{y})}{-(c\lambda x - s\lambda y)s + c\tilde{\tilde{y}} - \tilde{y}} \qquad \text{(C15)}\\ &= \big(\Lambda_\lambda \mathcal{Q}_\vartheta^{(\mathrm{edge})}\tilde{A}\big)(\underline{x}). \qquad \text{(C16)}\end{aligned}$$

3. Absence of rotational invariance

We provide a simple example for which $[\mathcal{Q}_\vartheta^{(\mathrm{edge})}, \mathcal{R}_{\vartheta'}] \neq 0$.

We consider the bare $\tilde{A}_0$, Eq. (57). Setting $\vartheta = \vartheta' = \pi/2$, we find

$$\big(\mathcal{Q}_{\pi/2}^{(\mathrm{edge})}\tilde{A}_0\big)(\underline{x}) = \sum_{\alpha=\pm1}\frac{\alpha\Gamma_\alpha/\pi}{[x_\omega - \alpha(x_\varphi - \Phi)/2 - \varepsilon_d]^2 + \Gamma^2}, \text{ and} \tag{C17}$$

$$\begin{aligned}&\big(\mathcal{R}_{\pi/2}\mathcal{Q}_{\pi/2}^{(\mathrm{edge})}\tilde{A}_0\big)(\underline{x}) \\ &\quad= \sum_{\alpha=\pm1}\frac{\alpha\Gamma_\alpha/\pi}{[x_\varphi - \alpha(-x_\omega - \Phi)/2 - \varepsilon_d]^2 + \Gamma^2}.\end{aligned} \tag{C18}$$

On the other hand,

$$\big(\mathcal{R}_{\pi/2}\tilde{A}_0\big)(\underline{x}) = \sum_{\alpha=\pm1}\frac{\Gamma_\alpha/\pi}{[x_\varphi - \alpha(-x_\omega - \Phi)/2 - \varepsilon_d]^2 + \Gamma^2}, \text{ and} \tag{C19}$$

$$\begin{aligned}&\big(\mathcal{Q}_{\pi/2}^{(\mathrm{edge})}\mathcal{R}_{\pi/2}\tilde{A}_0\big)(\underline{x}) \\ &\quad= \sum_{\alpha=\pm1}\frac{-\alpha\Gamma_\alpha/\pi}{[x_\varphi - \alpha(-x_\omega - \Phi)/2 - \varepsilon_d]^2 + \Gamma^2}.\end{aligned} \tag{C20}$$

Hence, $\mathcal{Q}_{\pi/2}^{(\mathrm{edge})}\mathcal{R}_{\pi/2}\tilde{A}_0 = -\mathcal{R}_{\pi/2}\mathcal{Q}_{\pi/2}^{(\mathrm{edge})}\tilde{A}_0$, and therefore $[\mathcal{Q}_{\pi/2}^{(\mathrm{edge})}, \mathcal{R}_{\pi/2}] \neq 0$.

APPENDIX D: NUMERICAL REPRESENTATION OF THE MULTIWEDGE MAP $\mathcal{Q}$

In this Appendix, a recipe for the numerical computation of the quadruple integral $\mathcal{Q}$ is given. The application to the test function (80), $f_{\underline{X},\delta}$, for a function value at $(i\varphi_m, i\omega_n)$ is computed. The first three integrals can be computed analytically by use of a computer algebra system. A numerical quadrature method can be used for the approximation of the remaining integral.

1. Analytic computation of first three integrals

Using the translational and scale invariance of the edge-to-edge contribution $\mathcal{Q}_\vartheta^{(\mathrm{edge})}$, only the action of $\mathcal{Q}_\vartheta^{(\mathrm{edge})}$ on our test function

$$f(x,y) = \frac{1}{\pi^2}\frac{1}{(y - x/2)^2 + 1}\frac{1}{(y + x/2)^2 + 1} \tag{D1}$$

has to be computed, yielding the results shown in Fig. 18. For brevity we set $y = x_\omega$ and $x = x_\varphi$. The first principal integral can be eliminated by straightforward application of the residue theorem:

$$(\mathcal{H}f)(x,\tilde{y}) = \fint dy\,\frac{\pi^{-1}}{\tilde{y} - y}f(x,y) = -\frac{8}{\pi^2}\,\frac{(x^2 - 12 - 4\tilde{y}^2)\tilde{y}}{(16\tilde{y}^4 + 32\tilde{y}^2 - 8\tilde{y}^2x^2 + 16 + 8x^2 + x^4)(x^2 + 4)}. \tag{D2}$$

As a next step, introducing the short-hand notation $s = \sin\vartheta$ and $c = \cos\vartheta$ and imposing the rotation operator $\mathcal{R}_\vartheta^{-1}$, one obtains

$$\big(\mathcal{R}_\vartheta^{-1}\mathcal{H}f\big)(k,l) = \mathrm{subs}\big(x \to kc + ls, \tilde{y} \to lc - ks; (\mathcal{H}f)(x,\tilde{y})\big). \tag{D3}$$

Here, "subs" denotes the operation of a variable substitution. In order to apply the second Hilbert transform, it is necessary to determine the poles of the corresponding integrand

$$\begin{aligned}g(k,\tilde{\tilde{y}};l) := \frac{\pi^{-1}}{\tilde{\tilde{y}} - l}\big(\mathcal{R}_\vartheta^{-1}\mathcal{H}f\big)(k,l) &= 8\,\frac{(k^2c^2 + 10\,kcls + l^2s^2 - 12 - 4\,l^2c^2 - 4\,k^2s^2)(lc - ks)}{\pi^3(k^2c^2 + 2\,kcls + l^2s^2 + 4)} \\ &\quad\times(4\,l^2c^2 - 6\,kcls + 4\,k^2s^2 + 4 + 4\,kc^2l - 4\,k^2cs + 4\,l^2sc - 4\,ls^2k + k^2c^2 + l^2s^2)^{-1}(-\tilde{\tilde{y}} + l)^{-1}\end{aligned} \tag{D4}$$

with respect to the integration variable l. One finds that the function has the following seven poles in the complex plane:

$$l_1 := \tilde{\tilde{y}}, \tag{D5}$$

$$l_{2,3} := \frac{-kc + 2ks \pm 2i}{s}, \tag{D6}$$

$$l_{4,5} := \frac{-kc + 2ks \pm 2i}{s + 2c}, \tag{D7}$$

$$l_{6,7} := \frac{kc + 2ks \pm 2i}{-s + 2c}. \tag{D8}$$

The Hilbert transform can now be evaluated through the residue sum

$$\left(\mathcal{H}\mathcal{R}_\vartheta^{-1}\mathcal{H}f\right)(k,\tilde{\tilde{y}}) = \sum_{n=1}^{7} \mathrm{Re}\left[2\pi i \mathrm{Res}_{l=l_n} g(k,\tilde{\tilde{y}};l)\right]\theta(\mathrm{Im}\, l_n). \tag{D9}$$

The Heaviside function $\theta(x)$ ensures that only poles from the upper half plane are taken into account for the evaluation of the contour integral which corresponds to the principal value integral. An explicit evaluation of the residue sum (D9) can be accomplished with a computer algebra system. A dramatic increase in complexity is coming along with the constraints $\mathrm{Im}\, l_n > 0$ which depend on the wedge orientation angle ϑ. In fact, six separate cases emerge as a function of ϑ. They can be parametrized by three overlapping different cases, namely (A) terms which are proportional to $\mathrm{sgn}(s)$, (B) terms which are proportional to $\mathrm{sgn}(2c + s)$, and (C) terms which are proportional to $\mathrm{sgn}(2c - s)$, discriminating between the different signs of $\mathrm{Im}\, l_n$. The term

$$\left(\mathcal{R}_\vartheta \mathcal{H}\mathcal{R}_\vartheta^{-1}\mathcal{H}f\right)(x,y) = \mathrm{subs}\left(k \to xc - ys, \tilde{\tilde{y}} \to yc + xs; \left(\mathcal{H}\mathcal{R}_\vartheta^{-1}\mathcal{H}f\right)(k,\tilde{\tilde{y}})\right) \tag{D10}$$

is then best reorganized into rational functions as coefficients of the sign functions,

$$\begin{aligned}\left(\mathcal{Q}_\vartheta^{(\mathrm{edge})} f\right)(x,y) &= \left(\mathcal{R}_\vartheta \mathcal{H}\mathcal{R}_\vartheta^{-1}\mathcal{H}f\right)(x,y) \\ &= A(x,y)\mathrm{sgn}(s) + B(x,y)\mathrm{sgn}(2c+s) \\ &\quad + C(x,y)\mathrm{sgn}(2c-s).\end{aligned} \tag{D11}$$

This explicit split is necessary for the study of the interplay of the rational functions $A(x,y)$, $B(x,y)$, and $C(x,y)$ in a computer algebra system.

(a) Rational coefficients of the transformed edge test function

The rational functions

$$A(x,y) = \frac{A_{\mathrm{enum}}(x,y)}{A_{\mathrm{denom}}(x,y)}, \tag{D12}$$

$$B(x,y) = \frac{B_{\mathrm{enum}}(x,y)}{B_{\mathrm{denom}}(x,y)}, \tag{D13}$$

$$C(x,y) = \frac{C_{\mathrm{enum}}(x,y)}{C_{\mathrm{denom}}(x,y)} \tag{D14}$$

have the following polynomials as enumerators and denominators:

$$\begin{aligned}A_{\mathrm{enum}}(x,y) = -8\Big[&\Big(-1 + x^2 + 1/4\, y^2 - \frac{41}{16}\, xy\Big)c^4 \\ &- \frac{13}{16}\Big(\frac{12}{13}\, xy + x^2 + \frac{12}{13} - \frac{28}{13}\, y^2\Big)sc^3 \\ &+\Big(1 + \frac{13}{8}\, xy - 1/2\, y^2\Big)c^2 + 1/16\, s(-4 + x^2 \\ &-4\, xy - 12\, y^2)c - 1/16\, y(-4\, y + x)\Big],\end{aligned} \tag{D15}$$

$$A_{\mathrm{denom}}(x,y) = \pi^2(x^2 + 4 - 4\, xy + 4\, y^2)K(x,y), \tag{D16}$$

$$\begin{aligned}B_{\mathrm{enum}}(x,y) = -8\Big[&\Big(-1 + x^2 + 1/4\, y^2 + \frac{41}{16}\, xy\Big)c^4 \\ &+\frac{13}{16}\, s\Big(-\frac{12}{13}\, xy + x^2 + \frac{12}{13} - \frac{28}{13}\, y^2\Big)c^3 \\ &+\Big(1 - \frac{13}{8}\, xy - 1/2\, y^2\Big)c^2 \\ &- 1/16\, s(-4 + x^2 + 4\, xy - 12\, y^2)c \\ &+ 1/16\, y(4\, y + x)\Big],\end{aligned} \tag{D17}$$

$$B_{\mathrm{denom}}(x,y) = (x^2 + 4\, xy + 4\, y^2 + 4)\pi^2 K(x,y), \tag{D18}$$

$$\begin{aligned}C_{\mathrm{enum}}(x,y) = &-3\,(-1/3\, y^2 - 3 + x^2)yxc^4 \\ &- s[(-3\, x^2 + 4)y^2 - 5\, x^2 + 4 + x^4]c^3 \\ &+3\,(-10/3 + x^2 - 2/3\, y^2)yxc^2 \\ &+[(-3\, x^2 + 4)y^2 - x^2 + 4]sc + yx(y^2 + 1),\end{aligned} \tag{D19}$$

and

$$C_{\mathrm{denom}}(x,y) = (x^2 + 4)\pi^2 K(x,y). \tag{D20}$$

For the denominators, we introduced the shared polynomial

$$\begin{aligned}K(x,y) = &[y^4 + (-3 - 6\, x^2)y^2 + 3\, x^2 - 4 + x^4]c^4 \\ &- 4(3/2 + x^2 - y^2)xsyc^3 \\ &+[-2\, y^4 + (2 + 6\, x^2)y^2 + 4 + x^2]c^2 \\ &- 4(1/2 + y^2)xsyc + y^2 + y^4.\end{aligned} \tag{D21}$$

(b) Composition of the rational coefficients

In contrast to the actual edge functions $\mathcal{Q}_\vartheta^{(\mathrm{edge})} f$, the coefficients $A(x,y)$, $B(x,y)$, and $C(x,y)$ are comparably ill behaved. For example, one obtains

$$B(x,y)|_{\vartheta=0} = -8\, \frac{x + y}{\pi^2(x^2 + 4)(x^2 + 4\, xy + 4\, y^2 + 4)}\, \frac{1}{x}. \tag{D22}$$

Apparently, the function diverges for $x \to 0$. The functions $A(x,y)$ and $C(x,y)$ are similarly structured. However, the actual edge functions, as displayed in Fig. 18, have no such singularities, but do rather represent smooth deformations of the test function when the wedge orientation angle ϑ is tuned. As a consequence, the real singularities are canceled as the

rational functions are added up in Eq. (D11). For a consistent further evaluation of the action of $\mathcal{Q}$ on the test function it is thus necessary to study each of the full combinations (D11) separately. There are six possible combinations, namely the sectors

$$\text{(a)} \quad 0 \leqslant \vartheta \leqslant \arctan 2, \tag{D23}$$

$$\text{(b)} \quad \arctan 2 \leqslant \vartheta \leqslant \pi - \arctan 2, \tag{D24}$$

$$\text{(c)} \quad \pi - \arctan 2 \leqslant \vartheta \leqslant \pi, \tag{D25}$$

$$\text{(d)} \quad \pi \leqslant \vartheta \leqslant \pi + \arctan 2, \tag{D26}$$

$$\text{(e)} \quad \pi + \arctan 2 \leqslant \vartheta \leqslant 2\pi - \arctan 2, \tag{D27}$$

$$\text{(f)} \quad 2\pi - \arctan 2 \leqslant \vartheta \leqslant 2\pi. \tag{D28}$$

For example, the expression for the sector (a) reads

$$\left(\mathcal{Q}_\vartheta^{(\text{edge})} f\right)|_{(\text{a})}(x,y) = A(x,y) + B(x,y) + C(x,y). \tag{D29}$$

(c) Contraction with the Poisson kernel

As a next step, one of the integrals introduced by Vladimirov's Poisson kernel (47) is evaluated analytically. For this, the pole structure of both the Poisson kernel (48) and the edge-transformed test function have to be analyzed.

(i) Pole structure of edge-transformed test functions. In fact, we are interested in the pole structure of the scaled and then translated edge-transformed test functions $(\mathcal{T}_{\underline{X}} \Lambda_{1/\delta} \mathcal{Q}_\vartheta^{(\text{edge})} f)(x',y')$ from Eq. (83). The poles and also the residues of these functions are, however, easily calculated from the poles and residues of $(\mathcal{Q}_\vartheta^{(\text{edge})} f)(x,y)$. This is the crucial advantage of translational and scale invariance of $\mathcal{Q}_\vartheta^{(\text{edge})}$.

For example, in sector (a), the following poles of $(\mathcal{Q}_\vartheta^{(\text{edge})} f)(x,y)$ with respect to x are obtained: $x_{1,2} = \pm 2i$, $x_{3,4} = sy \pm 2i$, $x_{5,6} = -2y \pm 2i$, $x_{7,8} = 2y \pm 2i$. The corresponding residues are $r_{1,2} = \frac{1}{2\pi^2 y}$, $r_{3,4} = -\frac{1}{2\pi^2 y}$, $r_{5,6} = \frac{1}{4\pi^2}\frac{-1\mp iy}{(y^2+1)y}$, $r_{7,8} = \frac{1}{4\pi^2}\frac{1\mp iy}{(y^2+1)y}$. The resulting residues of $(\mathcal{T}_{\underline{X}} \Lambda_{1/\delta} \mathcal{Q}_\vartheta^{(\text{edge})} f)(x',y')$ are then given by

$$r_i' = \frac{1}{\delta} \text{subs}\left(y \to \frac{y'-Y}{\delta}; r_i(y)\right), \tag{D30}$$

where the center of mass of the test function is $\underline{X} = (X,Y)$. They are associated to the poles of $(\mathcal{T}_{\underline{X}} \Lambda_{1/\delta} \mathcal{Q}_\vartheta^{(\text{edge})} f)(x',y')$, which are similarly given by

$$x_i' = X + \delta \text{subs}\left(y \to \frac{y'-Y}{\delta}; x_i\right). \tag{D31}$$

In order to obtain the true residues with respect to the x' contraction with the Poisson kernel, one only has to evaluate the Poisson kernel at the poles (48) and multiply r_i' with the value.

(ii) Pole structure of Poisson kernel. The pole structure of Vladimirov's Poisson kernel is rather straightforward to compute; however, rather lengthy expressions result for the poles. Similar to above, the residues have to be multiplied by the function values of the edge-transformed test function $(\mathcal{T}_{\underline{X}} \Lambda_{1/\delta} \mathcal{Q}_\vartheta^{(\text{edge})} f)(x',y')$ at the pole of the Poisson kernel. Poles of the rotated Poisson kernel $\mathcal{P}_{r,\vartheta}(\varphi_m,\omega_n;x',y')$ with respect to x' are

$$x_{1,2}' = \frac{s - c\epsilon}{s\epsilon + c} y' \pm i \frac{\eta_1 + \varepsilon\eta_2}{s\varepsilon + c}, \tag{D32}$$

$$x_{3,4}' = \frac{c\epsilon + s}{c - s\epsilon} y' \pm i \frac{\eta_1 - \epsilon\eta_2}{s\epsilon - c}. \tag{D33}$$

We introduced the short-hand notations $\eta_1 = \varphi_m c - \omega_n s$, $\eta_2 = \varphi_m s + \omega_n c$. The associated residues of $\mathcal{P}_{r,\vartheta}$ are easily determined.

(iii) Residue sum for the x' integral. An algebraic expression for the residue sum corresponding to the x' integral can be generated symbolically by evaluating

$$\begin{aligned} I_3(\varphi_m,\omega_n;y') = \int dx' \underbrace{\mathcal{P}_{r,\vartheta}(\varphi_m,\omega_n;x',y')}_{\text{“Poisson”}} \\ \times \underbrace{\left(\mathcal{T}_{\underline{X}} \Lambda_{1/\delta} \mathcal{Q}_\vartheta^{(\text{edge})} f\right)(x',y')}_{\text{“edge”}} \\ = \sum_{x_i'}^{\text{“edge”}} \text{Re}\,[2\pi i \mathcal{P}_{r,\vartheta}(\varphi_m,\omega_n;x_i',y') r_i'] \theta(\text{Im}\, x_i') \\ + \sum_{x_i'}^{\text{“Poisson”}} \text{Re}\left[2\pi i \left(\mathcal{T}_{\underline{X}} \Lambda_{1/\delta} \mathcal{Q}_\vartheta^{(\text{edge})} f\right)(x_i',y') \right. \\ \left. \times \text{Res}_{x'=x_i'} \mathcal{P}_{r,\vartheta}(\varphi_m,\omega_n;x',y')\right] \theta(\text{Im}\, x_i'). \end{aligned} \tag{D34}$$

However, it yields rather lengthy formulas, because the integrations with respect to x' have to be done separately, for each of the sectors (D23) to (D28). The growth in complexity is also due to the amount of parameters which increased dramatically by introducing the Poisson kernel and inserting the translations $\mathcal{T}_{\underline{X}}$ and scaling $\Lambda_{1/\delta}$ of the edge functions. It is possible to export the expressions resulting from Eq. (D34) from the computer algebra system to a file of Fortran code which is 500 kilobytes in size. Similar to the procedure described in Appendix D 1 b for the second integral, the expression (D34) includes removable discontinuities.

2. Numerical quadrature of the fourth integral

Due to the vast complexity of expression (D34), the last remaining integral,

$$I_4(\varphi_m,\omega_n) = \int dy' \, I_3(\varphi_m,\omega_n;y'), \tag{D35}$$

is evaluated numerically, making use of the exported Fortran code. Adaptive integration routines from the GNU Scientific Library are imposed.[33] Because the resulting matrix elements give rise to an inverse problem, it is compulsory to achieve a high integration accuracy. By definition, the integrand is most distinguishedly structured in the area $y' \approx Y$, on a scale δ. Special attention has to be drawn to the appropriate integration of this range.

The high-frequency tails $(-\infty, -R]$ and $[R,\infty)$ need to be integrated out separately, where R is the integration range of the conventional quadrature. For some parameter values of δ, $\underline{X}$, etc., problems with the convergence of these high-energy integrals may occur, due to floating point precision. Choosing

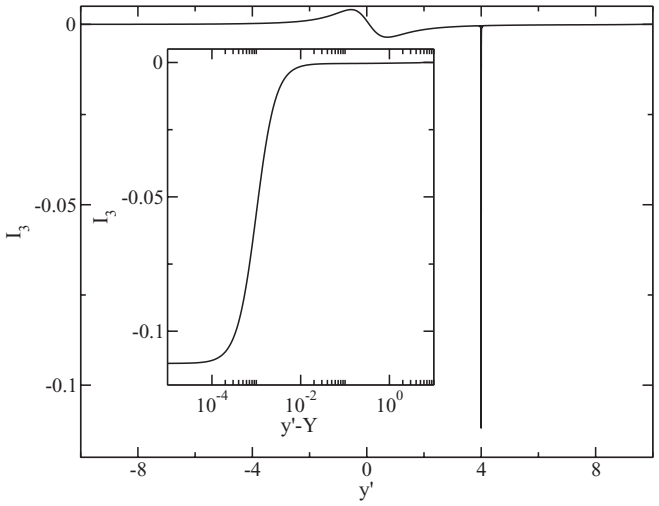

FIG. 26. Example for I_3 as a function of y', using $\varphi_m = 2.0$, $\omega_n = 2.0$, with test function location $X = 0.0$, $Y = 4.0$, and test function width $\delta = 10^{-3}$. The interacting branch cut geometry is used for the determination of r and ϑ.

a finite interval extending to $\pm\max(10^6, |X| \times 10^3, |Y| \times 10^3)$ is then usually sufficient for numerically satisfactory data.

A typical shape of the integrand I_3 is shown in Fig. 26. The structure at $y' \approx Y$ is not necessarily δ-shaped, but depending on the values of φ_m and ω_n it may rather look like the Hilbert transform of such. The integral may be computed at each point (X,Y) of the $\tilde{A}$ discretization lattice for all values of the simulation data $(i\varphi_m, i\omega_n)$ on a computer cluster. In practice, the computation of the matrix elements has to be done only once for each temperature β, regardless of the bias voltage. This is because an adjustment of the $\tilde{A}$ grid is not necessary in the latter case.

In future applications, one should aim at symbolically programming the residue sum of the fourth integral and then take the limit $\delta \to 0$ analytically.

APPENDIX E: MAXENT IMPLEMENTATION FOR DATA FROM MULTIPLE WEDGES

In this Appendix, the implementation of the MaxEnt algorithm for the $\mathcal{Q}$-mapping is described. Details on the computation of the numerical representation of $\mathcal{Q}$ were provided in Appendix D.

The local test function width $\delta_{\underline{x}}$ for the map $\mathcal{Q}_{r,\vartheta}$ can be adjusted to the local grid resolution when the function $\tilde{A}(\underline{x})$ is discretized. The inverse problem for the inference of spectral properties using assumption (65) is, by construction,

$$\operatorname{Im} G(i\varphi_m, i\omega_n) = (\mathcal{Q}_{r,\vartheta}\,\tilde{A})(i\varphi_m, i\omega_n). \tag{E1}$$

The values r,ϑ are those which specify the $T^{C_{r,\vartheta}}$ branch of G in which the vector $(i\varphi_m, i\omega_n)^T$ is located, as defined by axiom 1 of Sec. III D. The spectral function of the dot electrons can then again be gained by evaluating along the physical line,

$$A(\omega) = \tilde{A}(\Phi, \omega), \tag{E2}$$

of the inferred $(\vartheta = 0)$-edge function. See Ref. 4 for details.

(a) Discretization of $\tilde{A}(x_\varphi, x_\omega)$

The single-wedge MaxEnt-based analytic continuation problem proposed in Ref. 4 only required a rather straightforward discretization of the function $\tilde{A}(x_\varphi, x_\omega)$. In contrast, for the multiwedge mapping, the discretization of the edge function has to pay tribute to the strong intertwining of edge structure and branch cut structure which is revealed by $\mathcal{Q}^{(\text{edge})}$ (cf. Sec. IV D2).

Especially, it turns out that the limiting behavior along the singular directions of $\tilde{A}$ has to be captured numerically. In terms of the multiwedge approach, the singular directions dominate the mathematical structure. In our experience, also the *lateral* structure of $\tilde{A}(\underline{x})$ along the singular directions has to be resolved. We constructed a grid as follows. Let $\tilde{x}_1^{(i)}$ and $\tilde{x}_2^{(j)}$ be two variables which are discretized on ith and jth logarithmic grid points around zero, respectively. Then the grid $\underline{x}^{(i,j)} = \frac{\sqrt{5}}{20}\left(\begin{smallmatrix} 8 & 10 \\ -4 & 5 \end{smallmatrix}\right)\underline{\tilde{x}}^{(i,j)}$ yields an appropriate discretization of the edge, because the given matrix maps the double-cone $\mathbb{R}^+ \times \mathbb{R}^+ \cup \mathbb{R}^- \times \mathbb{R}^-$ and its complement to the wedges defined by the singular directions. The numerical test function width $\delta_{\underline{x}}$ can then be adjusted to the local grid resolution.

Also the high-energy structure of the Green's function has to be taken into account explicitly, because along the singular directions it does not decay. In practice, it seems to be important to have a very large logarithmically discretized fit region, for which in practice a x_φ/Γ region of at most $[-800, 800]$ is subject to modifications by the MaxEnt algorithm and a x_ω/Γ region of at most $[-400, 400]$. The singular-direction contributions beyond this range also prove not to be negligible, in a test with the bare Green's function (see also the G_0 benchmark below). In order to take them into account, their contribution up to very large energies ($x_\varphi \approx 10^5\Gamma$) is computed assuming a G_0-like structure along the directions, positioning adequately weighted δ spikes along it and substracting the corresponding contributions from the raw data, as done for the negative-spectral-function contributions of static observables in the first paper.

(b) Kernel structure

The kernel $\mathcal{Q}_{r,\vartheta}$ may exhibit rather sharp structures with respect to the $\tilde{A}$ function space. In particular, this may be the case in regions where the to-be-determined $\tilde{A}$ is expected to be very smooth and physically noninteresting. Consequently, for these regions, the MaxEnt discretization grid would be chosen rather coarse-grained. These potentially disturbing structures can already be seen from the formal structure of $\mathcal{P}_{r,\vartheta}$, which features strong anisotropies. The convolution with the (transformed) test functions $\mathcal{Q}_\vartheta^{(\text{edge})} f_{\underline{X},\delta}$ is, in general, no cure for this problem, because $\mathcal{Q}_\vartheta^{(\text{edge})} f_{\underline{X},\delta}$ is even more sharply structured, on the scale δ, which is of the order of the discretization scale (see Fig. 18).

In order to discuss this in more detail, some matrix elements of $\mathcal{Q}_{r,\vartheta}$ are plotted in Fig. 27. The orientation of the considered data point in Matsubara space defines the orientation of

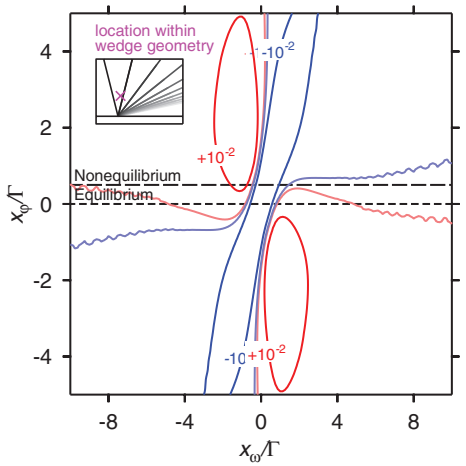

(a) $m = 1$, $n = 0$ ($\beta\Gamma = 5.0$)

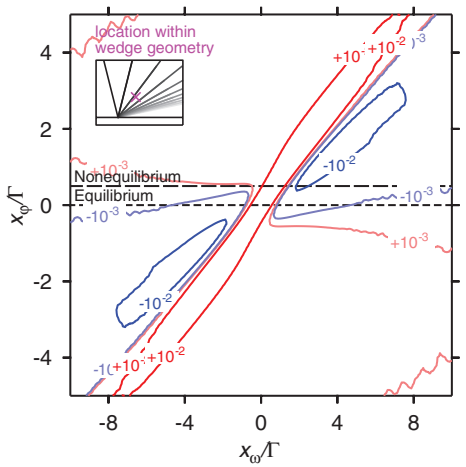

(b) $m = 1$, $n = 3$ ($\beta\Gamma = 5.0$)

FIG. 27. (Color online) Cut through $\mathcal{Q}_{r,\vartheta}$ in $\tilde{A}$ space for different pairs of $i\varphi_m$ and $i\omega_n$, at $\beta\Gamma = 5.0$. The wedge opening ratios r and wedge orientations ϑ (Fig. 16) are chosen according to the interacting branch cut geometry. The "nonequilibrium" line represents the location of the dot-electron spectral function for a system with source-drain voltage $e\Phi = 0.5\Gamma$. Wiggly structures at higher energies result from the increasingly coarse-grained $\tilde{A}$ grid.

the structure which emerges in the kernel with respect to the (x_φ, x_ω) coordinates of $\tilde{A}$ space. A major qualitative difference to the structure of the single-wedge kernels $\mathcal{P}_{r,\vartheta}$ is the emergence of distinguished negative regions. They are generated by the combinations of Hilbert transforms within the edge-to-edge map $\mathcal{Q}_\vartheta^{(\mathrm{edge})}$. As such, they are a direct consequence of the branch cuts. The negative and positive regions spread over a comparably wide range and will compete in the process of Bayesian inference, in which several $(i\varphi_m, i\omega_n)$ pairs and differently overlapping combinations of positive/negative regions are involved. The wide range of the regions appears to result from superimposing the $1/x$ tails of $\mathcal{Q}_\vartheta^{(\mathrm{edge})} f_{\underline{x},\delta}$ which are dominant for $\vartheta \approx \pi/2$ and $\vartheta \approx 3\pi/2$ and absent for $\vartheta \approx 0$, as well as $\vartheta \approx \pi$. Note that since the continuity assumption (65) becomes exact for larger energies, this feature can be expected to be contained in the kernel of an optimal continuation theory of Green's functions within the Matsubara voltage formalism.

The kernel structure moreover indicates that due to the leverage of the single-wedge constraint (as it applied to the MaxEnt calculations in Ref. 4), the nonequilibrium spectral function could now well be resolved. In the following, the interacting branch cut geometry is always used for the operator $\mathcal{Q}_{r,\vartheta}$. For brevity, the accordingly defined operator is shortly written as $\mathcal{Q}$, since r and ϑ are now well determined.

(c) Noninteracting Green's function as benchmark

The fundamental assumption of this chapter, Eq. (65), is exact for G_0 [Eq. (55)]. As a consequence, we use the noninteracting Green's function as a benchmark for our multiple-wedge numerical analytic continuation procedure, already assuming the interacting branch cut geometry for the construction of $\mathcal{Q}_{r,\vartheta}$, which is certainly also valid for G_0. *At present, from a numerical point of view, the method is composed of two technically challenging consecutive steps.* First, the kernel and its high-energy convolution with the Green's function have to be evaluated numerically up to a certain precision. Second, an appropriate default model has to be defined and the MaxEnt must converge to a good estimate in a controlled way.

In order to test the performance of the *first step*, we can take the exact solution as default model and run the MaxEnt with the discretized kernel. By construction, due to the design of Bryan's algorithm,[34] MaxEnt changes of the $\tilde{A}(x_\varphi, x_\omega)$ function will directly correspond to the numerical errors in the computation of the kernel matrix elements: Evidence for changes of the exact solution is taken from the exact data due to numerical imperfections in the kernel. Without integrating out the sharp structures of the kernel properly for these regions, serious artifacts are obtained even for larger test function broadnesses $\delta_{\underline{x}}$. This can be seen in the "historic" MaxEnt data shown Fig. 28. Here, $\delta_{\underline{x}}$ is chosen adaptively with respect to the local kernel resolution, namely $\delta_{\underline{x}} = 0.3 \times$ (localkernelgridresolution). The MaxEnt is able to modify the $\tilde{A}$ function on a large grid varying over the ranges $x_\varphi \in [-800, 800]$, $x_\omega \in [-400, 400]$. As the local kernel resolution is increased, averaging out its structure within the $\tilde{A}$ grid, an increasingly appropriate discretization of the kernel is obtained. In the computations shown in Fig. 28, realistic covariance weights for the imaginary-time data were assumed. If numerical errors $\gtrapprox \sqrt{10^{-13}}$ were included into the realization of the kernel, there would probably be stronger deviations from $\tilde{A}_0(x_\varphi, x_\omega)$ than observed. For some single points the $\delta_{\underline{x}}$ is so small that the adaptive quadrature of the fourth integral in $\mathcal{Q}$ does not converge. This can be seen best in Fig. 28(d), because here the kernel discretization grid is eight times finer than the $\tilde{A}(x_\varphi, x_\omega)$ discretization grid. Similarly, in the nonequilibrium situation, $\Phi \neq 0$, the function $\tilde{A}_0$ is not significantly altered by the 8×8-averaging kernel. This was tested explicitly also for large bias voltages, such as $e\Phi = \Gamma$.

The performance of the *second step* can be tested by using a kernel realization which succeeded in the first step and then performing runs with a modified default model. Because the noninteracting $\tilde{A}_0(x_\varphi, x_\omega)$ function has the correct singular behavior as $\underline{x} \to \infty$ we investigate the dependence of the

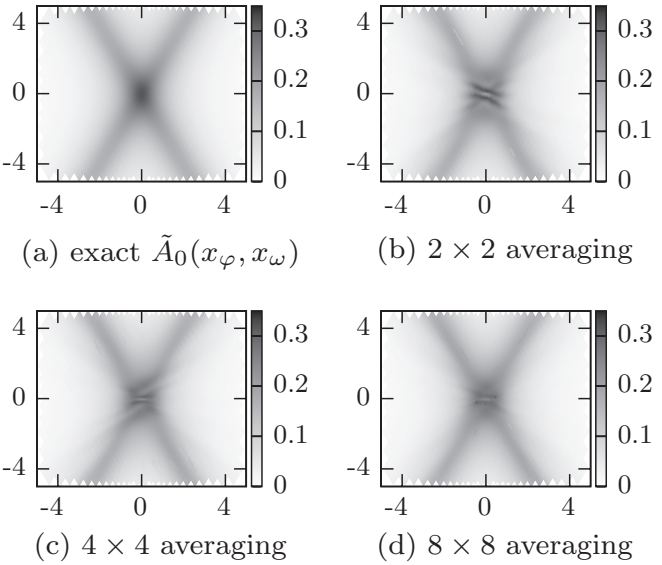

FIG. 28. Successive improvement of kernel quality by averaging out the local kernel structure within the local $\tilde{A}$ grid resolution. Data are shown for $U = 0$, $\Phi = 0$, $\beta\Gamma = 5$, $n = 0, \ldots, 9$, $m = -3, \ldots, 3$ and a realistic mock diagonal covariance matrix $C = \mathrm{diag}(\frac{10^{-13}}{\Gamma^2})$. The abscissa denotes x_φ/Γ, the ordinate denotes x_ω/Γ, grayscale denotes $\tilde{A}(x_\varphi, x_\omega)$ in units of Γ^{-1}.

MaxEnt results on the following default models:

$$\tilde{D}_{\sigma_{\mathrm{def}}}(x_\varphi, x_\omega) = \frac{1}{2\pi} \sum_{\alpha=\pm 1} \frac{\sigma_{\mathrm{def}}}{\left[x_\omega - \frac{\alpha}{2}(x_\varphi - \Phi)\right]^2 + \sigma_{\mathrm{def}}^2}. \quad \text{(E3)}$$

As compared to $\tilde{A}_0(x_\varphi, x_\omega)$, the width of the Lorentzians is varied. Using the best-quality kernel, i.e., 8×8-averaging [see Fig. 28(d)], increasing the default-model width quickly results in spurious features in the low- to intermediate-energy region, even though $\mathcal{Q}$ represents an exact relation between data and $\tilde{A}$ and the numerical representation of $\mathcal{Q}$ is sufficiently accurate. This is shown in Fig. 29. Away from the low-energy region also for $\sigma = 1.5\Gamma$ a good agreement with $\tilde{A}_0$ is obtained, i.e., a sharpened structure along the cross-shaped directions with an approximately correct amplitude [as compared to Fig. 28(a)]. The strong sensitivity of especially the low-energy range on the default model may be interpreted as a result of the subtle interplay of positive and negative regions of high-amplitude kernel matrix elements for different $(i\varphi_m, i\omega_n)$. The structure of the matrix elements was discussed above

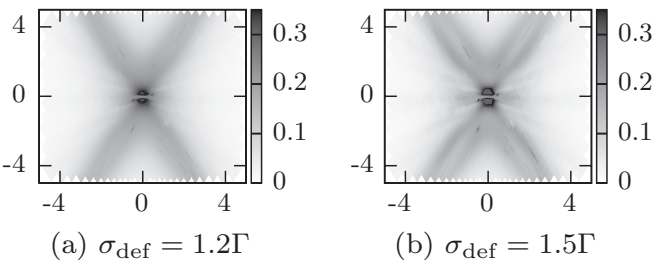

FIG. 29. Sensitivity to the default model, using the same parameters and scales as in Fig. 28(d).

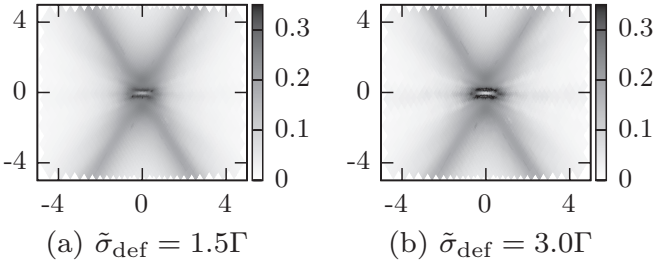

FIG. 30. MaxEnt results for flat low-energy default models (E4), $R = 5$. As compared to Fig. 29(b), the quality of low-energy data is increased significantly, due to the correct high-energy behavior of the default model. Scales are as in Fig. 28(d).

and plotted in Fig. 29. As shown in Fig. 29 a problem often encountered for not well-chosen default models is apparently an increase of spectral weight in the low-energy region $|\underline{x}| \approx 0$, which exceeds the color scale used in the plots by up to a factor of three, even for moderate deviations of σ_{def} from Γ. This is unfortunate, because not only for spectral functions unphysically high values may be deduced, but also the overall weight of the spectral function is too large. However, since the kernel $\mathcal{Q}$ imposes an exact relation on G_0 and is resolved well enough, this unfortunate aspect is identified as a pure MaxEnt ("*second step*") artifact. As such, it is no conceptual problem of the $\mathcal{Q}$ approach and can, in principle, be removed by developing a more sophisticated MaxEnt algorithm which imposes the physical constraints as prior information. In fact, this issue can be significantly reduced by a careful but straightforward analysis of the posterior probabilities within a set of smooth default models.

From our data we can conclude that default models with the shape (E3) are apparently not of much use for functions whose high-energy behavior along the singular directions is a Lorentzian with width Γ. Once the high-energy structure is known to be such, an interesting experiment is to flatten out the low- to intermediate-energy structure of the default model, by imposing an $\underline{x}$-dependent

$$\sigma_{\mathrm{def}}(x_\varphi) = \Gamma + (\tilde{\sigma}_{\mathrm{def}} - \Gamma)\frac{R^2}{x_\varphi^2 + R^2}, \quad \text{(E4)}$$

where R is the flattening radius and $\tilde{\sigma}_{\mathrm{def}} \gg \Gamma$ is a strong flattening of the default model's low-energy region. For G_0 it turns out that the resulting MaxEnt solution is practically identical to the $\sigma_{\mathrm{def}} = \Gamma$ solution. This is shown in Fig. 30 for two cases of low-energy default-model broadening. Consequently, the "*second step*" artifact for G_0 of overshooting low-energy values (Fig. 29) can just be cured by imposing the correct high-energy limit. The low-energy artifact is thus caused by missing *a priori* information about the high-energy structure. This appears to be another manifestation of the fact that the kernel $\mathcal{Q}$ puts a large range of energy scales in relation to each other.

(a) Application to the interacting model

Switching on a finite Coulomb interaction, one has to be aware of the fact that the $\mathcal{Q}$ mapping can no longer be expected

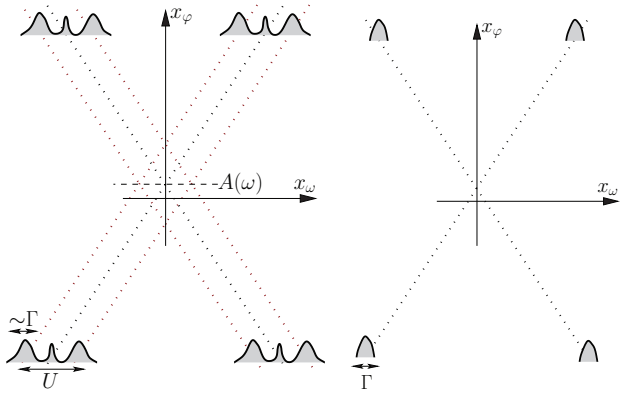

(a) nontrivial physics at $x_\omega \approx \pm x_\varphi/2$ (b) "asymptotic freedom"

FIG. 31. At high energies, one might (a) expect the lateral structure of $\tilde{A}(x_\varphi, x_\omega)$ to be composed of two Hubbard peaks and possibly a quasiparticle resonance which combine to the physical spectrum $A(\omega)$ at the intersection point. In the complementary scenario (b), the function $\tilde{A}$ would not differ from the noninteracting one at high energies.

to be fully exact. However, a special case of the assumption, namely the fitting ansatz in Ref. 1, is found to yield reasonable results which agree with other methods up to a certain extent.[11] Therefore, it seems worthwhile to investigate how far one can go with the controlled MaxEnt approach to the inversion of the $\mathcal{Q}$ mapping.[35]

(b) Lateral structure along singular directions

As shown in the preceding section, the *a posteriori* determination of a most adequate approximate *a priori* picture of the high-energy structure is crucial for the success of the MaxEnt procedure. As sketched in Fig. 31, at finite U, one may, for example, expect the lateral structure be an unphysical copy of a spectral function, i.e., two Hubbard peaks with possibly an additional peak associated to a quasiparticle resonance. Such a structure would extend over a range $\approx U$. However, the two parallel Hubbard peaks can be expected to approximately have a Lorentzian structure of width $\approx\Gamma$ and would generate a type of branch cut in the $\mathcal{Q}$ mapping which is equivalent to the one in G_0. In the strongly correlated regime, Hubbard satellites may be broadened up to a width of 2Γ, due to many-body correlations.[36]

It is *a priori* uncertain to what extent either of the intuitive pictures in Fig. 31 is correct. However, one of the conceptual

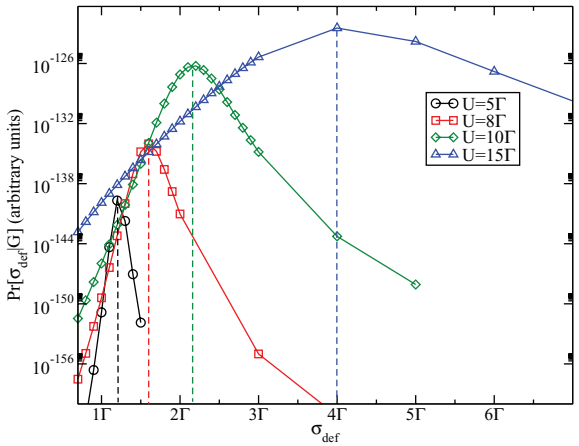

FIG. 32. (Color online) Posterior probability of the default model (E3) at $\beta\Gamma = 5$, $e\Phi = \Gamma$ for several interactions strengths. The result is found to be essentially independent of the bias voltage. The kernel validated in Fig. 28(d) has been used.

strengths of the $\mathcal{Q}$ mapping is the precise rendering of the high-energy structure of the imaginary-voltage theory (cf. Sec. IV C). One can expect that only a characteristic width of the lateral structure along the singular directions is needed in order to model the correct high-energy contribution to the amplitude of the discontinuity of $G(z_\varphi, z_\omega)$ at the low- to intermediate-energy portions of the branch cuts. Based on this, we can investigate the posterior probability $\Pr(\sigma_{\text{def}}|\bar{G})$ for default models (E3) as a function of their width σ_{def}.

The thus-determined most probable σ_{def} then serves as an effective description of the high-energy structure $\tilde{A}(x_\varphi, x_\omega)$ for the actual computations. However, as input data from the QMC simulations, only low- to intermediate-energy data are available. Therefore, the posterior probability probe with respect to default models (E3) has to be interpreted with care.

In Fig. 32, posterior probabilities for different interaction strengths are displayed. Due to the width being significantly larger than 2Γ for $U = 15\Gamma$ it is obvious that the lateral width cannot solely be interpreted as a signature of the Hubbard bands. Merely, the overall Lorentzian broadness of the spectral function seems to be obtained. Based on our data, neither of the scenarios of Fig. 31 can be preferred. However, based on our experience, the most probable high-energy structure also yields reasonable results in the case of comparably strong interactions. Thus, in the practical computations, first the most probable default model is identified. As a next step, the actual spectral functions are estimated.

[1] J. E. Han and R. J. Heary, Phys. Rev. Lett. **99**, 236808 (2007).
[2] J. E. Han, A. Dirks, and T. Pruschke, Phys. Rev. B **86**, 155130 (2012).
[3] E. Gull, A. J. Millis, A. I. Lichtenstein, A. N. Rubtsov, M. Troyer, and P. Werner, Rev. Mod. Phys. **83**, 349 (2011).
[4] A. Dirks, Ph. Werner, M. Jarrell, and Th. Pruschke, Phys. Rev. E **82**, 026701 (2010).
[5] Mark Jarrell and J. E. Gubernatis, Phys. Rep. **269**, 133 (1996).
[6] M. Pustilnik and A. Georges, J. Phys.: Condens. Matter **16**, R513 (2004).
[7] Y. Meir and N. S. Wingreen, Phys. Rev. Lett. **68**, 2512 (1992).
[8] We use $L = +$ and $R = -$ in mathematical expressions.
[9] J. E. Han, Phys. Rev. B **81**, 113106 (2010).

[10]J. W. Negele and H. Orland, *Quantum Many-particle Systems* (Addison-Wesley, Reading, MA, 1988).
[11]J. E. Han, Phys. Rev. B **81**, 245107 (2010).
[12]L. Mühlbacher, D. F. Urban, and A. Komnik, Phys. Rev. B **83**, 075107 (2011).
[13]M. Jarrell, A. Macridin, K. Mikelsons, and D. G. S. P. Doluweera, in *Lectures on the Physics of Strongly Correlated Systems XII*, edited by A. Avella and F. Mancini, AIP Conf. Proc. No. 1014 (AIP, New York, 2008), p. 34.
[14]K. Aryanpour, W. E. Pickett, and R. T. Scalettar, Phys. Rev. B **74**, 085117 (2006).
[15]Ph. Werner, T. Oka, M. Eckstein, and A. J. Millis, Phys. Rev. B **81**, 035108 (2010).
[16]V. S. Vladimirov, *Methods of the Theory of Functions of Several Complex Variables* (M.I.T. Press, Cambridge, MA, 1966).
[17]Sheaves are very general mathematical concepts, but here one may just imagine the set of holomorphic functions $U \to \mathbb{C}$ carried by a given domain $U \subset \mathbb{C}^d$.
[18]U. Rehmann (editor), *Encyclopedia of Mathematics*, http://eom.springer.de/.
[19]L. Hörmander, *An Introduction to Complex Analysis in Several Variables* (D. Van Nostrand Co., Princeton, NJ, 1966).
[20]See Sec. III I.
[21]G. M. Khenkin and A. G. Vitushkin (editors), *Encyclopedia of Mathematical Sciences: Several Complex Variables II* (Springer, Verlag, Berlin, Heidelberg, 1994).
[22]S. Bergman, *The Kernel Function and Conformal Mapping* (American Mathematical Society, Providence, RI, 1950).
[23]V. S. Vladimirov and V. V. Zharinov, Proc. Steklov Inst. Math.: Theor. Math. Phys. **175**, 131 (1988).
[24]D. Alpay, V. Bolotnikov, A. Dijksma, and B. Freydin, Arch. Math. **78**, 465 (2002).
[25]M. S. Brodskii, *Triangular and Jordan representations of linear operators* (American Mathematical Society, Providence, RI, (1971) [translated from the Russian by J. M. Danskin, Transl. Math. Monogr. **32**, Theorem 4.5].
[26]R. Nevanlinna, *Eindeutige analytische Funktionen* (Springer, Berlin, 1936).
[27]H. Behnke and F. Sommer, *Theorie der analytischen Funktionen einer komplexer Veränderlichen* (Springer, Berlin, 1962).
[28]A. Korányi and L. Pukánsky, Trans. Am. Math. Soc.y **108**, 449 (1963).
[29]Because in our application ε will not necessarily be small, we changed to the notation r.
[30]L. Hörmander, Grundlehren Math. Wiss. **256**, 343 (1983).
[31]For the definitions, see Fig. 16.
[32]A. F. Albuquerque *et al.*, J. Magn. Magn. Mater. **310**, 1187 (2007).
[33]M. Galassi *et al.*, *GNU Scientific Library Reference Manual*, 3rd ed. (Network Theory Ltd., Godalming, UK, 2009).
[34]R. K. Bryan, Eur. Biophys. J. **18**, 165 (1990).
[35]To be more precise, for technical reasons (conservation of the spectral function normalization for *any* causal self-energy) the fits in Refs. 1 and 11 were performed with respect to the self-energy, not with respect to the Green's function. Because the $\mathcal{Q}$ mapping is also exact for ansatz functions of the fits presented in Ref. 1, the fits are essentially special cases of the present work. The first-order Padé approximant fits presented in Ref. 11 represent a different kind of generalization.
[36]M. T. Glossop and D. E. Logan, J. Phys.: Condens. Matter **14**, 6737 (2002).